Measurement of the electromagnetic form factors of the proton via elastic scattering in the Q^2 range from 0.5 to 2 $(GeV/c)^2$

Dissertation zur Erlangung des Grades
„Doktor der Naturwissenschaften" (Dr. rer. nat.)
am Fachbereich Physik, Mathematik und Informatik
der Johannes Gutenberg-Universität in Mainz

Julian Müller
geboren in Simmern/Hunsrück

Institut für Kernphysik
Johannes Gutenberg-Universität Mainz
Juni 2023

Tag der mündlichen Prüfung: 15.12.2023

Abstract

The electric and magnetic form factor of the proton are connected to the distribution of electric charge and electric current inside the proton. As a fundamental property of the proton, the knowledge of the form factors therefore allows to gain insight into the structure of the proton. The form factors are accessible in elastic electron-proton scattering experiments, which have been performed since the 1950s. One distinguishes two types of experiments, the scattering with polarized and unpolarized electrons. Around the turn of the millennium, it was found that there is a discrepancy in the electric to magnetic form factor ratio of the proton $G_E(Q^2)/G_M(Q^2)$, when comparing the results of both methods. According to the data from polarization experiments, the ratio follows a linear decreasing trend with increasing momentum transfer Q^2, whereas the ratio measured in unpolarized scattering remains roughly constant. The commonly assumed explanation for this discrepancy is the contribution of the two photon exchange (TPE) to the scattering process, which has a different influence on polarized and unpolarized scattering.
To investigate the discrepancy in the form factor ratio and the influence of the TPE, new unpolarized elastic electron-proton scattering data were measured at the Mainz Microtron MAMI and the 3-spectrometer-facility of the A1 collaboration. The data were taken at seven beam energies between 720 MeV and 1508 MeV to cover the Q^2 region from $0.5\,(\mathrm{GeV/c})^2$ to $2\,(\mathrm{GeV/c})^2$. The new data extends an already existing data set from an earlier measurement in 2010. In total, the MAMI data set now consists of 1676 cross section points in the Q^2 range between $0.004\,(\mathrm{GeV/c})^2$ and $2\,(\mathrm{GeV/c})^2$. The measured cross sections were corrected for radiative processes by utilizing an extensive simulation, which calculates the radiative corrections for each event. Instead of using the classical Rosenbluth technique, the MAMI data set was analyzed via a direct fit of a form factor model to the cross section data to separate the form factors. The fitting procedure was also used to determine the normalization of the data, however, the fit proved to have stability issues for the data at higher beam energies. The inclusion of external data from previous unpolarized experiments provided the stability needed for the fit and an excellent agreement between the two parts of the MAMI data set could be demonstrated. Two different models for the TPE correction were applied to the data before the fit, to investigate by how much the contribution shifts the form factors. The extracted form factor ratio from the fit was compared to the data from polarization experiments.
The results showed that the MAMI data produce a linear decreasing form factor ratio, independently of the applied TPE model. This trend has not been observed in previous unpolarized experiments. An overall lower electric to magnetic form factor ratio in unpolarized electron-proton scattering could play an important role in solving the discrepancy between polarized and unpolarized experiments.

Contents

1. Introduction

In 1911 Rutherford, Geiger and Marsden found the first experimental evidence for an internal structure of atoms [1, 2]. Based on the experimental results from scattering α particles on gold foils, a model of the atom was developed, which laid the foundation of the modern view of atoms as a small and heavy nucleus and a hull of electrons. Rutherford also identified the proton as the hydrogen nucleus in 1919, when he transmuted nitrogen into oxygen [3]. The discovery of the neutron by Chadwick in 1932 [4] and the previous discovery of the electron by Thomson in 1897 [5] completed the picture of the fundamental building blocks of the atom.

According to Dirac's theory of pointlike spin-$\frac{1}{2}$ particles in relativistic quantum mechanics, the proton with charge e and mass M should have the magnetic moment

$$\mu = \frac{g}{2}\frac{e}{2M}\hbar = \frac{g}{2}\mu_N \tag{1.1}$$

where $\hbar$ is Planck's constant h divided by 2π. From Dirac's equation it follows that the gyromagnetic ratio g is exactly 2. (later experiments found a slight deviation from the factor of two [6–8], which can be explained by quantum electrodynamics). The magnetic moment of the proton was expected to be $\mu_p = \frac{g}{2} = 1$, in units of the nuclear magneton μ_N. Experiments by Stern et al. in 1933 [9, 10] however measured a 2.5 times larger magnetic moment. The latest recommended value is $\mu_p = 2.792775599(30)$ [11]. This result is incompatible with the prediction from quantum electrodynamics (QED) and a clear proof that the proton is not a pointlike particle, but has an inner structure. In the current understanding, the proton is a composite particle bound by the strong interaction, consisting of three valence quarks (two up quarks and one down quark) and a see of gluons and quark-antiquark pairs. The internal structure of the proton can be investigated via elastic electron-proton scattering, from which the electric and magnetic form factors G_E and G_M can be extracted. The form factors describe the distribution of electric charge and electric current inside the proton. So far, quantum chromodynamics (QCD), the theory of the strong interaction, can not provide a detailed model of the form factors.

The electric and magnetic form factors of the proton have been investigated in electron-proton scattering since the 1950s. The first measurements were performed by Hofstadter et al. at Stanford [12–14]. They found that the form factors of the proton, as well as the magnetic form factor of the neutron could be described with

a dipole shape, which corresponds to an exponential charge distribution. A later measurement by Simon et al. [15] in Mainz showed that this empirical parameterization is not sufficient to describe the data. However, the dipole parameterization is still used today to describe the rough trend of the form factors and as an approximation at low momentum transfer Q^2. Since then, the nucleon form factors have been of interest with many experiments being conducted until today. Over the last two decades, two unresolved problems which are introduced below have brought the interest in the proton form factors to a new high. The first issue concerns the size of the proton, which is also of great interest in the field of atomic physics since the value is needed to accurately calculate energy levels and atomic transitions. The charge radius of the proton measured in atomic spectroscopy [16] was significantly higher than the radius extracted from the standard dipole parameterization of the electric form factor. The second problem is the focus of this thesis: A discrepancy in the proton's electromagnetic form factor ratio $\mu_p G_E(Q^2)/G_M(Q^2)$ between polarized and unpolarized electron-proton scattering. The discrepancy was first observed in 1999. In a polarization transfer experiment by Jones et al. [17] the obtained form factor ratio was found to be in disagreement with previous unpolarized measurements (Rosenbluth measurements). According to the polarization data, the from factor ratio follows a linearly decreasing trend with increasing Q^2, whereas the ratio measured in unpolarized scattering remains constant around 1.

Proton Charge Radius

To determine the electric and magnetic charge radius of the proton Bernauer et al. performed a new measurement at A1/MAMI [18]. A total of 1422 cross section points were measured in a kinematic range in Q^2 from $0.004\,(\mathrm{GeV/c})^2$ to $1\,(\mathrm{GeV/c})^2$. The results were published in 2010 and 2014 [19, 20]. In elastic scattering, the electric and magnetic root mean square radius of the proton can be determined by extrapolating the slope of the form factors G_E and G_M to $Q^2 = 0$:

$$\langle r^2 \rangle = -\frac{6}{G(0)} \left. \frac{dG(Q^2)}{dQ^2} \right|_{Q^2=0} . \tag{1.2}$$

The measured charge radius at MAMI in 2010 was in agreement with the CODATA recommended value: 0.8768(69) fm [21]. In the same year, the proton radius was also determined by Pohl et al. using spectroscopy to measure the Lamb shift in muonic hydrogen atoms. They found a significantly smaller proton radius of 0.84184(67) fm [22]. The discrepancy between the spectroscopy result and the CODATA value of 5σ sparked the problem of the proton radius, by now infamously known as the proton radius puzzle. Since then, the charge radius of the proton was extracted from various experiments and reanalyses of electron-proton scattering data, some of

which are shown in figure 1.1. The latest results from the PRad electron scattering experiment at JLab [23] and from ordinary atomic hydrogen spectroscopy favor the small proton charge radius from muonic hydrogen spectroscopy. In view of these results, there is already a debate about whether the radius puzzle is resolved. The PRad data, however, is in disagreement on a form factor level with previous scattering measurements, creating a new puzzle [24].

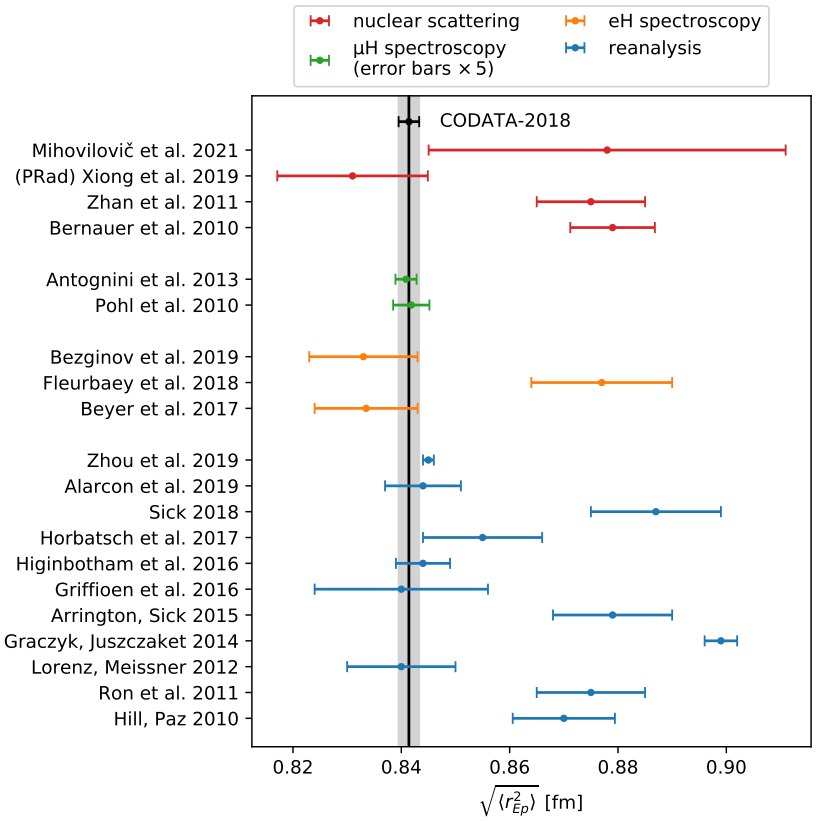

Figure 1.1.: The electric charge radius of the proton as extracted from electron scattering experiments [19, 23, 25, 26], atomic (ordinary) and muonic hydrogen spectroscopy [27–29], [22, 30], and from reanalyses of electron-proton scattering data [31–41]. The black line represents the 2018 CODATA recommended value. The error bars of the muonic hydrogen spectroscopy are scaled by a factor of five for visibility.

Proton Form Factor Ratio

The experiment by Bernauer et al. in 2010 followed a proposal by the A1 collaboration to measure the electromagnetic form factors in the Q^2 region up to $Q^2 = 2\,(\mathrm{GeV/c})^2$ [42]. In the experiment, however, cross section data was only measured up to a momentum transfer of $Q^2 = 1\,(\mathrm{GeV/c})^2$. At the time of the measurement there was no experience with the beam quality of the third accelerator stage called MAMI C and the beam could not yet be extracted at different

energy levels [18]. The data at low Q^2 measured in 2010 is not well suited for the investigation of the proton form factor discrepancy. As can be seen in figure 1.2, the discrepancy in the form factor ratio between polarized and unpolarized measurements becomes more significant at higher Q^2. The experiment presented in this thesis is the continuation of the previous measurement at the higher beam energies of MAMI C, to tackle the second unsolved problem: The puzzle of the form factor ratio.

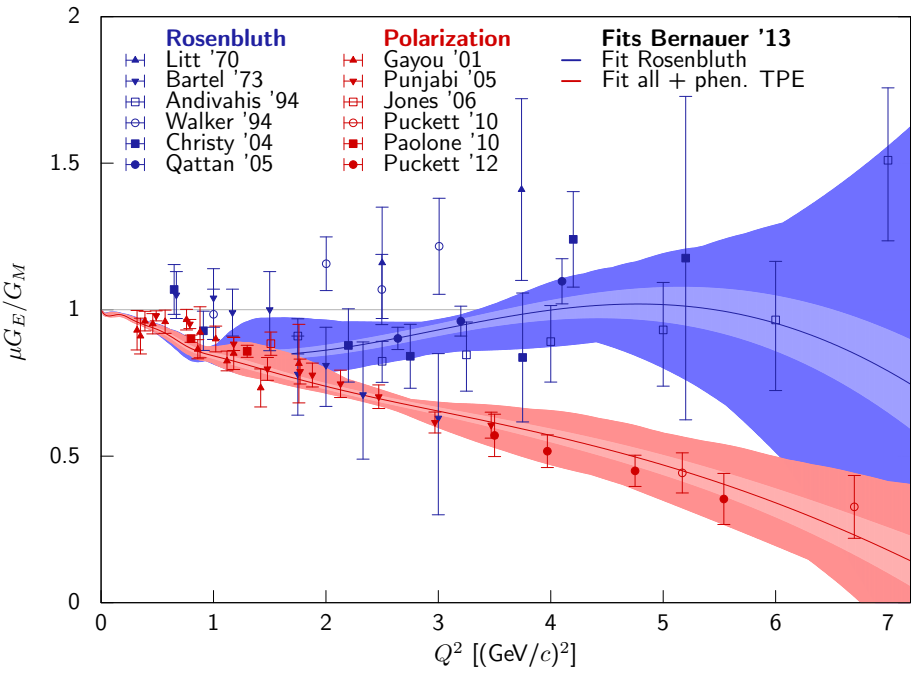

Figure 1.2.: Form factor ratio of the proton as a function of Q^2 measured in polarized and unpolarized (Rosenbluth) scattering. The curves are fits to the world data [20]. The bands show the statistical (light shaded) and the model uncertainty (dark shaded) added linearly. The red fit contains a phenomenological two photon correction, see section 2.3. Figure from [43].

A possible explanation for this difference might be the two photon exchange (TPE) correction. While it is believed that the TPE contribution has a bigger influence in unpolarized scattering [44], the issue is still not fully resolved. The formulae used to calculate the cross sections in polarized and unpolarized experiments are in one-photon approximation, also called the Born approximation. This approximation seems to be insufficient at higher Q^2. Accurately determining the TPE proves to be challenging for both, theory and experiment [45]. On the theory side the TPE contribution depends on the hadronic structure, unlike the standard radiative corrections which are generally model independent. On the experimental side, direct TPE measurements have to be done at backward angles and at high momentum transfer where the TPE effects are largest, but the cross section is suppressed. Direct measurements of the TPE have been done in measurements of the positron-proton

to electron-proton elastic cross section ratio at VEPP-3, CLAS, and OLYMPUS [46–48]. Most of the first order radiative corrections cancel in this ratio, but the TPE correction from the interference of one and two-photon exchange has opposite signs for electrons and protons. The data from the three experiments are in reasonable agreement with each other, but the results are not definitive [45]. It is not clear if the discrepancy in the form factor ratio can be explained by the TPE alone. In this context, another interesting outcome of the 2010 measurement at MAMI was a 4% larger magnetic form factor compared to older Rosenbluth measurements (figure 1.3). A larger magnetic form factor than previously assumed would play a crucial role in solving the discrepancy in the form factor ratio.

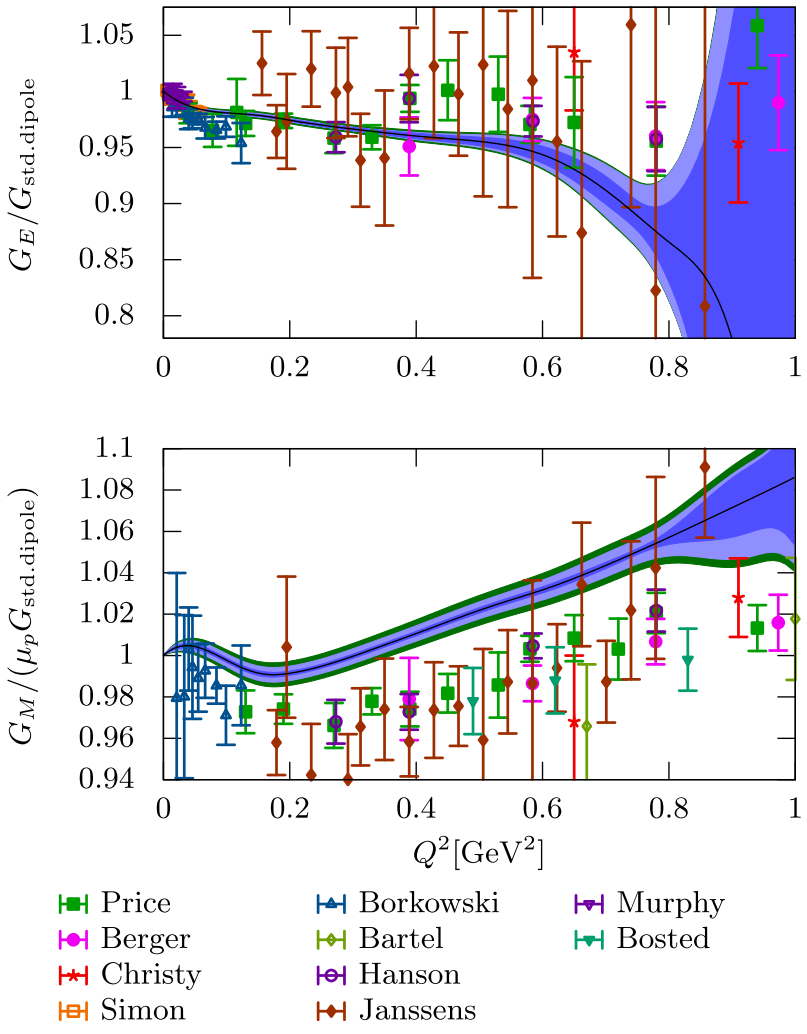

Figure 1.3.: Electric and magnetic form factor of the proton measured at A1/MAMI in 2010 [19]. The magnetic form factor in the lower plot is about 4% larger compared to previous measurements. The dark blue area is the statistical 68% pointwise confidence band and the light blue area corresponds to the experimental systematic error. The green bands indicate a variation of the Coulomb correction by 50%. Original figure in [20].

The goal of this thesis is to examine if the magnetic form factor is larger than seen in previous measurements, and to investigate the influence of the TPE on the form factor ratio. As mentioned before, in the 2010 MAMI experiment, cross section data was only measured up to a momentum transfer of $Q^2 = 1\,(\mathrm{GeV/c})^2$. Now with the higher beam energies of the third accelerator stage MAMI C being available, the accessible kinematic range increases to $Q^2 = 2\,(\mathrm{GeV/c})^2$. Elastic electron-proton scattering was measured at momentum transfers $0.5\,(\mathrm{GeV/c})^2 < Q^2 < 2\,(\mathrm{GeV/c})^2$. This kinematic range was chosen to have an overlap with the previous measurement and to cover the full kinematic range available at MAMI C. The measurement program is designed to provide a seamless continuation of the previous experiment at MAMI.

This thesis is organized as follows: In chapter 2 the theoretical basics of elastic electron-proton scattering are introduced, in particular the Rosenbluth formula and the required radiative corrections. Chapter 3 describes the MAMI accelerator facility and the spectrometer setup of the A1 experiment, focusing on the target and the detector system. An overview of the data measured in this work and in the 2010 MAMI experiment is given in chapter 4. Chapter 5 presents the simulation of the cross section measurement and the generator for the radiative tail is described in detail. The simulation will be used to extract the first order cross section from the cross section measurement. In chapter 6 the calibration of the drift chambers and the Čerenkov detector is discussed. Chapter 7 describes the analysis of the data and the calculation of the cross section from the measured count rates. This chapter also details the matching of experiment and simulation and the determination of the luminosity. The data are analyzed by a direct fit of a form factor model to the cross section data. The fitting procedure is introduced in chapter 8 and the form factor results from the fit to the MAMI data are discussed. In Chapter 9 the MAMI data is combined with external data from previous experiments and the same fitting procedure is performed again. Different TPE models are applied to the data before the fit to investigate the influence of the TPE on the extracted form factors. The results for the form factor ratio $\mu_p G_E(Q^2)/G_M(Q^2)$ are then compared to the data from polarization measurements. Finally, a summary of the obtained results in this work and outlook is given in chapter 10.

2. Elastic Electron-Proton Scattering

2.1. The Rosenbluth Cross Section

This section outlines how the cross section for electron-proton scattering is obtained at lowest order (Born approximation). The derivation of this cross section is described in great detail in [49]. The process of interest is shown in figure 2.1.

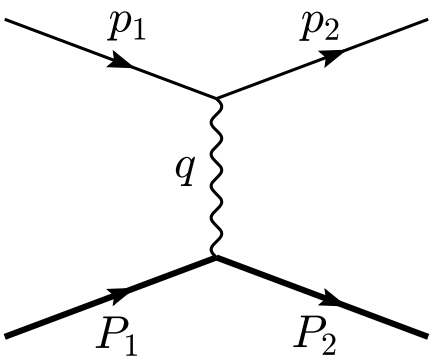

Figure 2.1.: Lowest order process of elastic electron-proton scattering. The bold lines represent the incoming and outgoing proton.

In a fixed target experiment, as the one presented here, it is easiest to view the process in the laboratory frame, where the proton is initially at rest. The four-momenta in this frame of reference are:

$$p_1 = (E, \boldsymbol{p}), \quad p_2 = (E', \boldsymbol{p}'), \quad P_1 = (M_0, \boldsymbol{0}), \quad P_2 = (E'_P, \boldsymbol{P}'), \tag{2.1}$$

where p_1 and p_2 are the four momenta of the incoming and outgoing electron. The incoming proton with mass M_0 is initially at rest and is scattered with four momentum P_2. Here, natural units are chosen: $\hbar = c = 1$. The final cross section (equation (2.11)) is calculated in the ultra relativistic limit $m_0 \ll E$, in which the rest mass of the electron m_0 is assumed to be small compared to the kinetic energy. From this, it also follows that $|\boldsymbol{p}| \approx E$ and the four momentum transfer simplifies to

$$q^2 = (p - p')^2 = 2(m_0^2 - E'E + |\boldsymbol{p}'||\boldsymbol{p}| \cos\theta) = -4EE' \sin^2 \frac{\theta}{2} \tag{2.2}$$

with the energy of the scattered electron

$$E' = \frac{E}{1 + \frac{E}{M_0}(1 - \cos\theta)} \,. \tag{2.3}$$

The squared four momentum of the virtual photon is space-like and therefore, always negative. It is customary to use $Q^2 = -q^2$ for convenience.

The cross section σ is defined as

$$\sigma = \frac{\text{transition rate per particle}}{\text{incoming particle flux}} = \frac{W_{fi}}{\Phi}\,, \tag{2.4}$$

where the transition rate W_{fi} is the probability per unit of time for a particle in initial state i to be scattered into final state f. The unit of σ is barn: $1\,\mathrm{b} = 10^{-28}\,\mathrm{m}^2$. The transition rate can be calculated using Fermi's (second) Golden Rule:

$$W_{fi} = 2\pi|\mathcal{M}|^2\rho_f\,. \tag{2.5}$$

The matrix element $\mathcal{M}$, also known as the invariant amplitude, describes the transition from the initial state to the final state and can be determined by evaluating the relevant Feynman diagrams for the process at hand. ρ_f is the energy density of final states, a factor that accounts for the number of available final states in phase space. Applying Fermi's Golden Rule to a two-body scattering process, one can write down the differential cross section [50]

$$\begin{aligned} d\sigma \;=& \frac{1}{4\sqrt{(p_1\cdot P_1)^2 - (m_0 M_0)^2}}\,|\mathcal{M}|^2 \\ &\times\; (2\pi)^4\delta^{(4)}(p_1 + P_1 - p_2 - P_2)\,\frac{d^3\boldsymbol{p}'}{(2\pi)^3 2E'}\,\frac{d^3\boldsymbol{P}'}{(2\pi)^3 2E'_P} \end{aligned} \tag{2.6}$$

which gives the probability for the scattering of the particles into three-momentum range $\boldsymbol{p}' + d^3\boldsymbol{p}'$ and $\boldsymbol{P}' + d^3\boldsymbol{P}'$. Equation (2.6) includes the following kinematic factors: The denominator in the first factor is the Lorentz-invariant particle flux, the four dimensional δ-function enforces conservation of four-momentum and the last two factors are the density of final states for the scattered electron and proton. This process can be measured in a single arm experiment, where only the electron is detected. In the experiment, the detector only detects the electron in a small part $d\Omega$ of the full solid angle. Assuming full energy acceptance of the electron detector, one can calculate the inclusive cross section by integrating over the proton momentum and the magnitude of the electron momentum. The volume element

$$d^3\boldsymbol{p}' = |\boldsymbol{p}'|^2 d|\boldsymbol{p}'|d\Omega \tag{2.7}$$

can be written in spherical coordinates. This results in the differential cross section $\frac{d\sigma}{d\Omega}$ for the scattering of an electron with the angular components of the momentum inside $d\Omega$.

Apart from basic kinematics, the fundamental interaction is contained in the invariant amplitude. Using Feynman rules for the process in figure 2.1 yields

$$\mathcal{M} = j_\mu \frac{g^{\mu\nu}}{q^2} J^\nu = j_\mu \frac{1}{q^2} J^\mu \,. \tag{2.8}$$

The electron and proton currents are

$$\begin{aligned} j^\mu &= -e\bar{u}(p_2)\gamma^\mu u(p_1) \\ J^\mu &= e\bar{u}(P_2)\Gamma^\mu u(P_1)\,, \end{aligned} \tag{2.9}$$

where u is a spinor that satisfies the Dirac equation and γ^μ are the gamma matrices. Since the proton is not a point-like particle, but has internal structure, the vertex function Γ^μ in the transition current has to be described by a more general parameterization than in the case of the electron. This leads to the introduction of form factors. The vertex function must be a Lorentz vector that also fulfills the important criteria of Hermiticity and gauge invariance. One can show [49], that the most general expression that meets these conditions has the form

$$\Gamma^\mu = \gamma^\mu F_1(Q^2) + i\sigma^{\mu\nu} q_\nu \frac{\kappa}{2M_0} F_2(Q^2) \tag{2.10}$$

with $\sigma^{\mu\nu} = \frac{i}{2}(\gamma^\mu\gamma^\nu - \gamma^\nu\gamma^\mu)$ and the anomalous magnetic moment of the proton $\kappa = \mu_p - 1$. F_1 and F_2 are the Dirac and Pauli form factors, respectively. For a free proton, they only depend on the four momentum transfer q^2.

In the experiment which is presented in this thesis, the polarization of the electron and the proton is not measured. To get an equation for the unpolarized cross section, one has to calculate a spin averaged squared invariant amplitude by averaging the spins in the initial state and summing over the spins in the final state. Using the ansatz for the proton vertex function in equation (2.10) and the spin averaged invariant amplitude in combination with equation (2.6) yields the cross section

$$\begin{aligned} \left(\frac{d\sigma}{d\Omega}\right) &= \left(\frac{d\sigma}{d\Omega}\right)_{\text{Mott}} \\ &\times \left[\left(F_1^2(Q^2) + \tau(\kappa F_2(Q^2))^2\right) + 2\tau(F_1(Q^2) + \kappa F_2(Q^2))^2 \tan^2\frac{\theta}{2}\right] \end{aligned} \tag{2.11}$$

for unpolarized electron-proton scattering in the one photon approximation, with $\tau = Q^2/(4M_0^2)$. Equation (2.11) is known as Rosenbluth's formula [51]. The Mott cross section

$$\left(\frac{d\sigma}{d\Omega}\right)_{\text{Mott}} = \frac{4Z^2\alpha^2 E'^2}{Q^4}\frac{E'}{E}\left(1 - \beta^2\sin^2\frac{\theta}{2}\right) \tag{2.12}$$

is the part that describes the scattering of an electron on a spinless, point-like target. For an easier interpretation and to eliminate the mixed terms in the Rosenbluth cross

section, the Sachs form factors are introduced [54]:

$$\begin{aligned} G_E(Q^2) &= F_1(Q^2) - \tau\kappa F_2(Q^2) \\ G_M(Q^2) &= F_1(Q^2) + \kappa F_2(Q^2)\,. \end{aligned} \tag{2.13}$$

In the Breit frame, where $P_1 = (E_P, \boldsymbol{P})$ and $P_2 = (E_P, -\boldsymbol{P})$, no energy is transferred to the proton and G_E and G_M are found to be the Fourier transform of the distribution of charge and magnetization. In the static limit $q^2 \to 0$ the electron probes the full distribution of electric charge and magnetic moment. The form factors have to be normalized in this limit to give the full charge and magnetic moment:

$$G_E(0) = 1, \quad G_E(0) = \mu_p \tag{2.14}$$

With the Sachs form factors, equation (2.11) becomes

$$\left(\frac{d\sigma}{d\Omega}\right) = \left(\frac{d\sigma}{d\Omega}\right)_{\text{Mott}} \left[\frac{G_E^2(Q^2) + \tau G_M^2(Q^2)}{1+\tau} + 2\tau G_M^2(Q^2)\tan^2\frac{\theta}{2}\right], \tag{2.15}$$

now containing the squares of the form factors without any interference terms. With the photon polarization parameter

$$\varepsilon = \left(1 + 2(1+\tau)\tan^2\frac{\theta}{2}\right)^{-1}, \tag{2.16}$$

equation (2.15) can be written in a concise form:

$$\left(\frac{d\sigma}{d\Omega}\right) = \left(\frac{d\sigma}{d\Omega}\right)_{\text{Mott}} \frac{\varepsilon G_E^2(Q^2) + \tau G_M^2(Q^2)}{\varepsilon(1+\tau)} \tag{2.17}$$

The Rosenbluth cross section does not depend on the azimuthal, or out-of-plane angle φ. It has two independent parameters, which are commonly chosen to be the energy E of the incoming electron and the scattering angle θ, or the momentum transfer Q^2 and the photon polarization parameter ε.

The key task for the experiment is now to extract and disentangle the form factors from the measured cross section. This is traditionally done by a Rosenbluth separation [51]. Equation (2.17) can be written as a reduced cross section:

$$\sigma_{\text{red}} = \varepsilon(1+\tau)\left(\frac{d\sigma}{d\Omega}\right) / \left(\frac{d\sigma}{d\Omega}\right)_{\text{Mott}} = \varepsilon G_E^2(Q^2) + \tau G_M^2(Q^2) \tag{2.18}$$

For a fixed value of Q^2, the reduced cross section depends linearly on ε. When measuring at different values of ε at the same value of Q^2, one can identify $G_E(Q^2)$ as the slope and $\tau G_E(Q^2)$ as the y-axis intercept. Nowadays, an alternative approach is also possible. One can simply perform a multi-parameter fit of form factor models

to the cross section data. With the necessary tools and the computing power being available, fits with a high number of parameters may be readily implemented. This method, sometimes named super Rosenbluth separation, is described in chapter 8.

2.2. Radiative Corrections

The cross section introduced in the previous section is only the lowest order approximation, in which a single photon is exchanged between the electron and the proton. The measured cross section in the experiment, however, also contains higher order processes. These processes are taken into account by a correction factor

$$\left(\frac{d\sigma}{d\Omega}\right)_{\text{exp}} = \left(\frac{d\sigma}{d\Omega}\right)_0 (1+\delta)\,. \tag{2.19}$$

The first order correction

$$\delta = \delta_{\text{vac}} + \delta_{\text{vertex}} + \delta_R + Z\delta_1 + Z^2\delta_2 \tag{2.20}$$

includes the vacuum polarization δ_{vac}, the electron vertex correction δ_{vertex}, the correction for real photon emission in the initial or final state δ_R and hadronic corrections $Z\delta_1$ and $Z^2\delta_2$. The atomic number occurring in the hadronic corrections is set to $Z = 1$ for the proton in the following. Higher order corrections can be taken into account approximately by exponentiating the contributions in equation (2.20). An exception is the vacuum polarization, for which the iteration to higher orders does not lead to an exponentiation. In [55] the total correction was found to be:

$$\left(\frac{d\sigma}{d\Omega}\right)_{\text{exp}} = \left(\frac{d\sigma}{d\Omega}\right)_0 \frac{e^{\delta_{\text{vertex}}+\delta_R+\delta_1+\delta_2}}{(1-\delta_{\text{vac}}/2)^2}\,. \tag{2.21}$$

The calculation of the correction factors in equation (2.20) was done by Vanderhaeghen et al. [55] and by Maximon and Tjon [56]. Their findings are summarized below. All results are given in the ultra relativistic limit $Q^2 \gg m^2$.

2.2.1. Electron Corrections

Figure 2.2 shows the related graphs to the corrections on the electron side. In the calculation of graphs like the electron vertex correction (figure 2.2 bottom), divergent terms occur in the integral over the momentum of the internal photons. Divergent terms are called ultraviolet divergent for high momenta, and infrared divergent for low momenta. The ultraviolet divergences can be resolved by renormalization techniques [55, 56]. The cancellation of infrared divergent terms of real and virtual photon processes of the same order has been known for a long time and was already

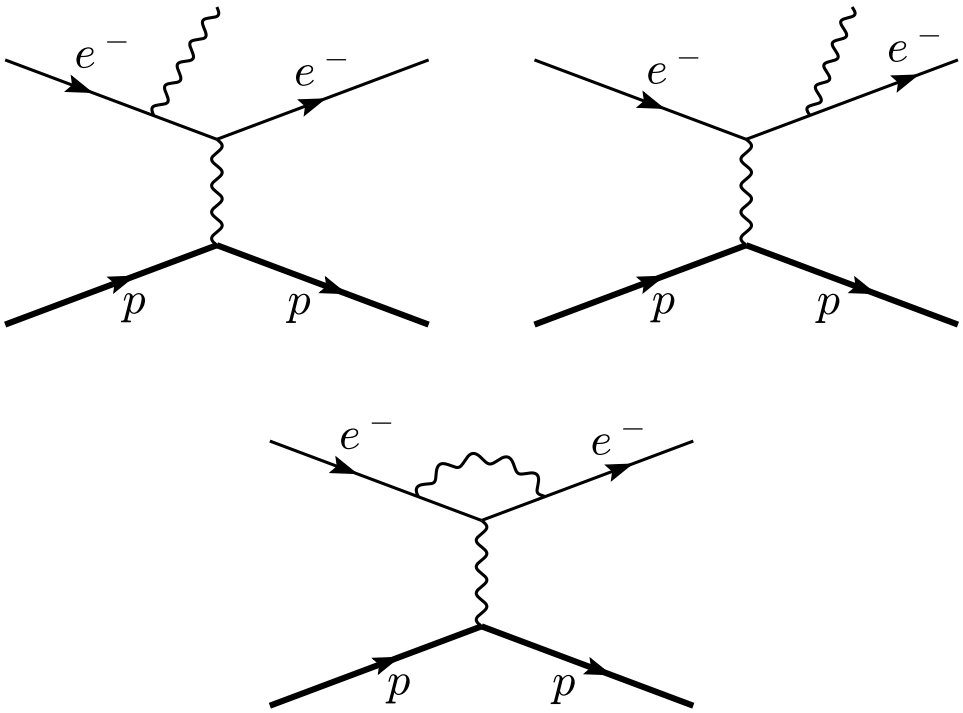

Figure 2.2.: Diagrams for the initial and final state radiation known as the Bethe-Heitler diagrams (top) and the electron vertex correction (bottom).

calculated in [57] and [58]. In this case, the infrared divergent part of the electron vertex correction cancels exactly the infrared divergent terms from the contribution of soft photon emission (figure 2.2 top). The contribution of the electron vertex correction is given by

$$\delta_{\text{vertex}} = \frac{\alpha}{\pi}\left\{\frac{3}{2}\ln\left(\frac{Q^2}{m^2}\right) - 2 - \frac{1}{2}\ln^2\left(\frac{Q^2}{m^2}\right) + \frac{\pi^2}{6}\right\}. \tag{2.22}$$

The correction from soft photon emission depends on the cut-off energy $\Delta E'$. It is the maximally allowed energy loss of the scattered electron due to radiation, so that it is still accepted as an elastically scattered electron. The cut-off energy therefore depends on the properties of the detector and on data analysis cuts. Radiation in the initial and final state lead to the factor

$$\begin{aligned}\delta_{\text{R}} = \frac{\alpha}{\pi}\Bigg\{&\ln\left(\frac{(\eta\Delta E')^2}{EE'}\right)\left[\ln\left(\frac{Q^2}{m^2}\right) - 1\right] \\ &-\frac{1}{2}\ln^2\eta + \frac{1}{2}\ln^2\left(\frac{Q^2}{m^2}\right) - \frac{\pi^2}{3} + \text{Sp}\left(\cos^2\frac{\theta}{2}\right)\Bigg\}\end{aligned} \tag{2.23}$$

with the Spence function (or dilogarithmic function)

$$\mathrm{Sp}(x) = -\int_0^x \frac{\ln(1-t)}{t} dt \tag{2.24}$$

and the recoil factor $\eta = \frac{E}{E'}$. E' is the energy of an elastically scattered electron at an angle θ. Applying a simple correction factor δ_R for each spectrometer setting would not be very accurate, because the correction factor varies over the acceptance of the spectrometer. Instead, within this work the corresponding energy loss distribution will be simulated and compared to the experiment, to achieve the correct $\Delta E'$-dependence.

2.2.2. Vacuum Polarization

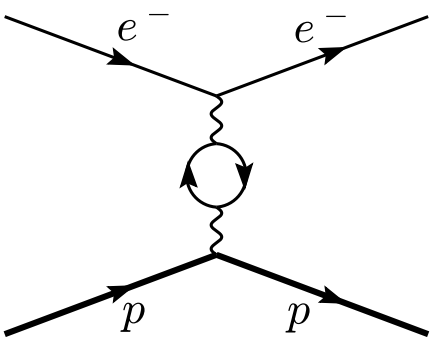

Figure 2.3.: Vacuum polarization diagram.

The contribution of the vacuum polarization process, shown in figure 2.3, is given by:

$$\begin{aligned} \delta_{\mathrm{vac}} &= \frac{\alpha}{\pi}\frac{2}{3}\left\{\left(v^2 - \frac{8}{3}\right) + v\frac{(3-v^2)}{2}\ln\left(\frac{v+1}{v-1}\right)\right\} \\ &\overset{Q^2 \gg m^2}{=} \frac{\alpha}{\pi}\frac{2}{3}\left\{-\frac{5}{3} + \ln\left(\frac{Q^2}{m_l^2}\right)\right\} \\ v^2 &= 1 + \frac{4m_l^2}{Q^2} \end{aligned} \tag{2.25}$$

In the Q^2 range of this experiment, one has not only to take electrons into account in the internal loop, but also muons and tau-leptons by substituting the respective lepton mass m_l into equation (2.25) and subsequent summing up of the individual lepton contributions. Care has to be taken that the approximation $Q^2 \gg m^2$ is only valid for electrons.

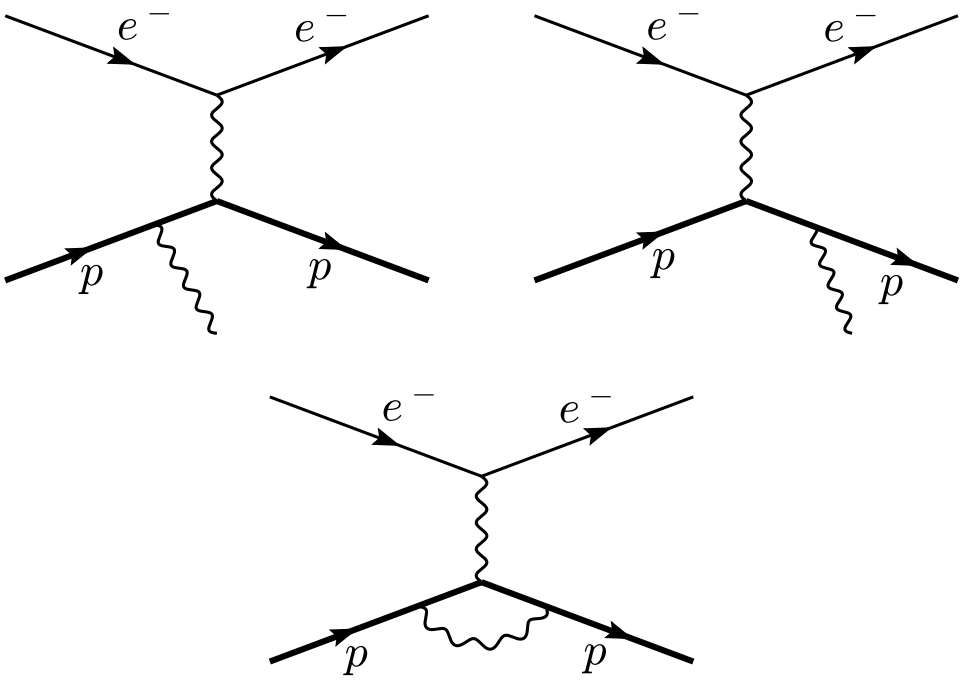

Figure 2.4.: The diagrams for the real photon emission of the proton (top) are known as the Born diagrams. The bottom diagram is the proton vertex correction.

2.2.3. Hadronic Corrections

The hadronic corrections include the corrections on the proton side from figure 2.4, as well as the two photon exchange processes shown in figure 2.5. Unlike the radiative corrections discussed above, the hadronic corrections are not model independent and require information on the internal structure of the nucleus. In the calculation by Maximon and Tjon the box and crossed-box diagrams in figure 2.5 are calculated using a soft photon approximation and the internal structure of the proton is neglected [56]. The hadronic corrections are split into three parts: δ_1 proportional to Z, δ_2 proportional to Z^2 and $\delta_{\text{el}}^{(1)}$ where all the structure dependence of the nucleon is contained. The first two parts are

$$\delta_1 = \frac{2\alpha}{\pi}\left\{\ln\left(\frac{4(\eta\Delta E')^2}{Q^2 x}\right)\ln\eta + \mathrm{Sp}\left(1-\frac{\eta}{x}\right) - \mathrm{Sp}\left(1-\frac{1}{\eta x}\right)\right\}, \tag{2.26}$$

$$\begin{aligned}\delta_2 = \frac{\alpha}{\pi}\Bigg\{&\ln\left(\frac{4(\eta\Delta E')^2}{M_P^2}\right)\left(\frac{E'_P}{|\vec{p}'_P|}\ln x - 1\right) + 1 \\ &+ \frac{E'_P}{|\vec{p}'_P|}\left(-\frac{1}{2}\ln^2 x - \ln x \ln\left(\frac{\rho^2}{M_P^2}\right) + \ln x - \mathrm{Sp}\left(1-\frac{1}{x^2}\right) + 2\mathrm{Sp}\left(-\frac{1}{x}\right) + \frac{\pi^2}{6}\right)\Bigg\}\end{aligned} \tag{2.27}$$

with

$$x = \frac{(Q+\rho)^2}{4M_P^2}\,, \quad \rho^2 = Q^2 + 4M_P^2\,. \tag{2.28}$$

The contribution of the third term $\delta_{\mathrm{el}}^{(1)}$ can be considered negligible in the kinematic range available at MAMI [56].

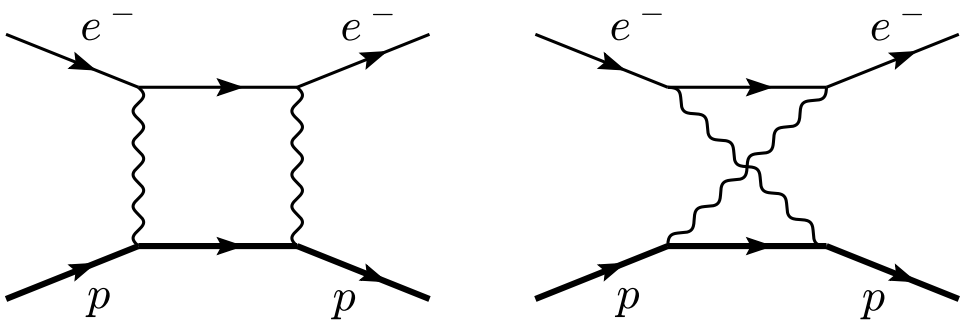

Figure 2.5.: Two photon exchange diagrams.

2.3. Two Photon Exchange (TPE)

The radiative corrections of Maximon and Tjon in section 2.2 do not include the contributions of the Coulomb distortion and the hard two photon exchange (TPE), where both photons carry a large momentum.

The scattering process via many soft photons is referred to as Coulomb Distortion. A simple correction factor $(1 + \delta_F)$ for this effect is the Coulomb correction (also called Feshbach correction) [59, 60]:

$$\delta_F = Z\,\alpha\,\pi\,\frac{\sin\frac{\theta}{2} - \sin^2\frac{\theta}{2}}{\cos^2\frac{\theta}{2}}\,. \tag{2.29}$$

This correction factor is included in the analysis of the previous MAMI data, because it has a direct influence on the extraction of the proton radius [18]. The focus in this work is on the form factors of the proton themselves and furthermore how the form factors shift when the Coulomb correction and the TPE correction are added on top of the radiative corrections of Maximon and Tjon. For this purpose, the two models described below are compared, which include these two corrections. Therefore, the Coulomb correction was divided out in the data from the MAMI measurement in 2010. This has to be kept in mind when comparing this work to the results of the previous MAMI measurement in [18–20]. A more in depth discussion of the Coulomb Distortion can be found in [61].

If both photons in the diagram in figure 2.5 have considerable momentum, the intermediate state can be an excited state of the proton. The modeling of excited intermediate states in theory is difficult and there is still some uncertainty to it. The contribution of the TPE becomes increasingly important at larger Q^2 and could explain the difference in the form factor ratio between polarized and unpolarized electron-proton scattering. Because of the model dependency of the TPE contribution, published cross section data in general has no TPE correction applied. A TPE radiative correction is therefore also not included in the simulation of the experiment in chapter 5. Instead, two models are compared and applied to the cross section data by hand as an additional factor $(1 + \delta_{\mathrm{TPE}})$. The first model is of phenomenological nature:

$$\delta_{\mathrm{TPE}} = -(1 - \varepsilon)\, a\, \ln(b\, Q^2 + 1)\,, \tag{2.30}$$

with two parameters a and b that were determined in a fit to the world data in [20]. The linear dependence in ε and the logarithmic dependence in Q^2, where chosen based on earlier calculations of the TPE in [62]. This model is applied to the data together with the Coulomb correction from equation (2.29). The second model is a recent calculation by Ahmed et al. [63], using a dispersive approach. In addition to the elastic nucleon intermediate state, they include the contributions from all resonances $J^P = 1/2^{\pm}$ and $3/2^{\pm}$ below $1.8\,\mathrm{GeV/c^2}$

$$\begin{aligned} &\Delta(1232)\ 3/2^+,\ N(1440)\ 1/2^+,\ N(1520)\ 3/2^-,\\ &N(1535)\ 1/2^-,\ \Delta(1620)\ 1/2^-,\ N(1650)\ 1/2^-,\\ &\Delta(1700)\ 3/2^-,\ N(1710)\ 1/2^+,\ N(1720)\ 3/2^+, \end{aligned} \tag{2.31}$$

where each individual resonance has a Breit-Wigner shape with a finite, constant decay width. The contribution of the elastic nucleon intermediate state is relative to the Maximon-Tjon corrections and reproduces the Coulomb correction in equation (2.29) for $Q^2 = 0.001\,(\mathrm{GeV/c})^2$. Figure 2.6 shows a comparison of the phenomenological model and the resonance model in the kinematic range of this experiment. The difference in the TPE correction δ_{TPE} between the two models does not exceed 1%. Both models predict a maximum TPE contribution of roughly 2.5% at the highest Q^2 of $2\,(\mathrm{GeV/c})^2$. The impact of the two models on the form factors is compared in chapter 9.

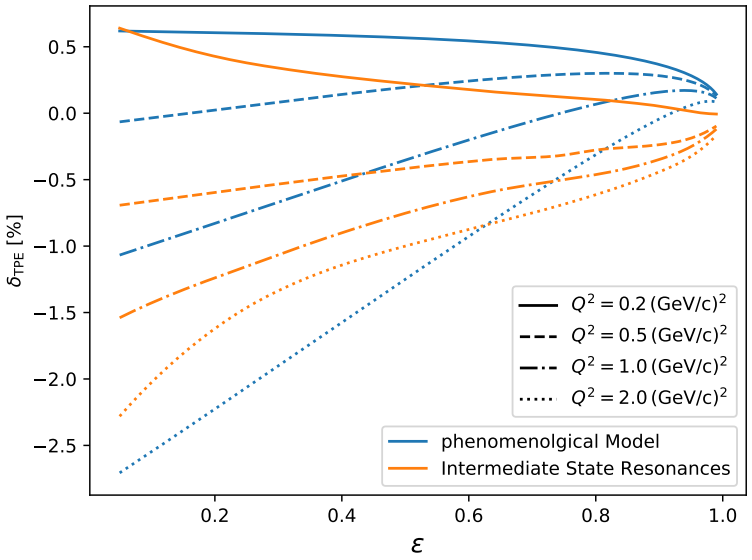

Figure 2.6.: Comparison of two models for the hard two photon exchange correction in elastic electron-proton scattering. The phenomenological Model was determined in a fit to the world data in [20]. The second model is a calculation that includes all hadronic resonant intermediate states with $J^P = 1/2^{\pm}$ and $3/2^{\pm}$ below $1.8\,\mathrm{GeV/c^2}$ [63].

3. Experimental Setup

3.1. The MAMI Accelerator

MAMI (Mainz Microtron) is an electron accelerator located at Johannes Gutenberg-University of Mainz [64, 65]. It is a continuous wave accelerator that can provide unpolarized electron beams with beam currents of up to 100 μA. A GaAs photo cathode is also available which can produce polarized electrons with a maximum beam current of 20 μA. The accelerator facility consists of a linear pre-accelerator, three race track microtrons (RTM) and an harmonic double-sided microtron (HDSM). A floor plan can be seen in figure 3.1.

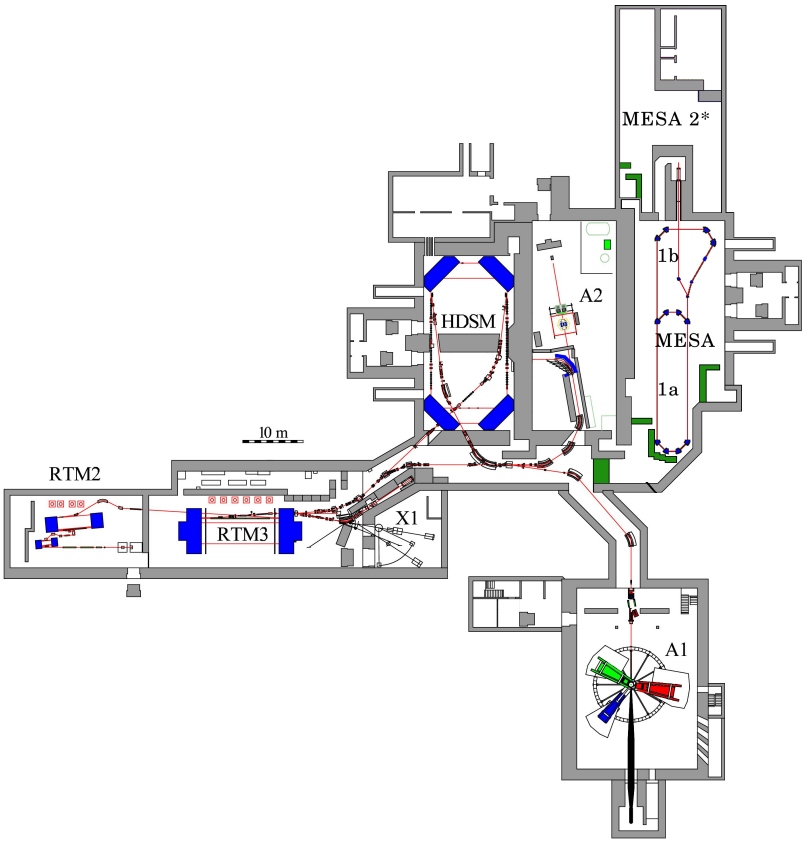

Figure 3.1.: Floor plan of the accelerator facilities and experimental halls.

The acceleration process of MAMI is subdivided into three successive stages. The first stage consists of the linear accelerator and the first two race track microtrons RTM1 and RTM2. Here, the electrons reach 180 MeV, which is the minimal beam energy available for the experiments. The RTM3 as the second and the HDSM as

the third stage are optional and can increase the beam energy up to the design end energies of 855 MeV and 1508 MeV, respectively. At these energies, the 1-σ energy spread is 30 keV and 110 keV. After a few years of operation, the maximum output energy could be increased to 1.6 GeV [66, 67]. By using movable extraction magnets, MAMI can deliver beam energies in steps of 15 MeV. In the case of the RTM3, a dipole magnet can be placed at every other recirculation beam-pipe. It applies a kick to the beam, so it is deflected to the exit beam line system. The Situation is similar for the HDSM, however there is one exception which is discussed in the next section.

3.1.1. 1402 MeV Beam Energy

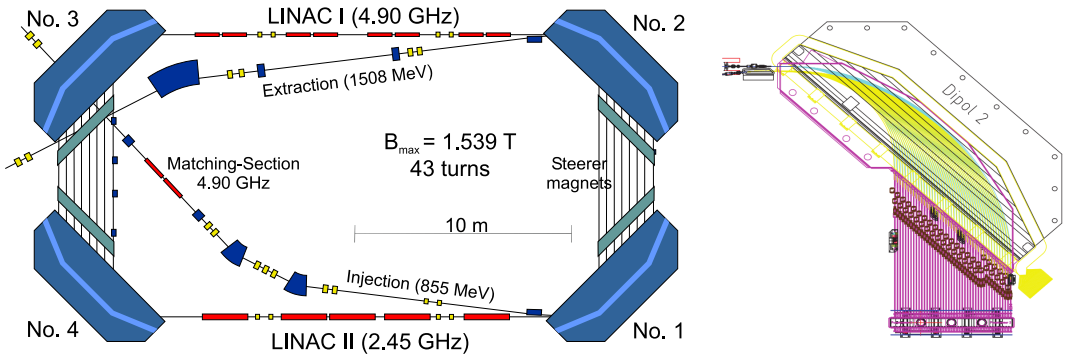

Figure 3.2.: Schematic of the HDSM on the left [67] and the extraction system on the right [68].

Figure 3.2 shows a schematic drawing of the HDSM and the extraction system. A movable magnet to extract the beam at the desired energy is installed in front of dipole No. 2. Because of space limitations, the extraction magnet can not be placed at some of the outer recirculation beam pipes without reconstruction of the steerer magnets. As a result, beam energies between 1322 MeV and 1508 MeV are inaccessible in standard operation [67]. Not being able to measure cross sections within this energy range would be a major restriction for the experiment presented in this work. Especially the high Q^2 settings are important for a precise measurement of the magnetic form factor. This experiment was the first one to request 1402 MeV, one of the missing energies. In January 2015, prior to the main beam time later that year, a few days of beam time were dedicated to test the new energy. Since there were no other experiments planned that demanded one of the missing energies, the MAMI accelerator-group decided against a modification of the relevant parts of the HDSM. Instead, the injection energy into the HDSM was reduced from 855 MeV to 795 MeV. The magnetic field of the HDSM was tuned down and the accelerating field gradient was adjusted accordingly, to get a beam energy of 1402 MeV after

recirculating through all 43 turns [68]. The MAMI operators were able to provide the new energy on the first day of testing.

3.2. Spectrometer Facility of A1

The A1 collaboration operates a setup of high resolution magnetic spectrometers at MAMI. The experimental setup was designed to allow for a wide range of electron scattering experiments and consequently offers high flexibility. All three main spectrometers A, B and C are installed on a ring mount and can be rotated around the target in the center, to measure scattered particles at different angles. Additionally, spectrometer B can be tilted to enable out-of-plane measurements. The spectrometers can be operated in single-arm, double or triple coincidence mode. Positively or negatively charged particles are detectable by changing the polarity of the magnets. Figure 3.3 shows a picture of the experimental hall.

Figure 3.3.: The A1 experimental hall with the spectrometers A in red, B in blue and C in green. Spectrometers A and C are shown with opened shielding houses, revealing the detectors. The beam enters the hall through the thin beam pipe on the right.

A detailed description of the core setup is given in [69]. Over the course of the years, several detectors have been developed that can be added to the setup. These include dedicated spectrometers for measuring pions or kaons and a neutron detector.

3.2.1. Optical Properties of the Spectrometers

The magnet configuration of spectrometer A consists of a quadrupole, a sextupole and two dipoles. It has point-to-point focusing in the dispersive plane for high momentum resolution and point-to-parallel focusing in the non-dispersive plane for a high resolution of the scattering angle. Spectrometer C has the same configuration and focusing conditions, but is scaled down to roughly 80% the size of spectrometer A. The design of spectrometer B consists only of one clam-shell dipole, at which the pole shoes are inclined and not parallel to each other. This design features a narrow footprint and allows for measurements at small forward angles. Spectrometer B has point-to-point imaging in the dispersive as well as in the non-dispersive plane, leading to a higher spatial resolution at the target, at the cost of a smaller acceptance. Figure 3.4 shows the layout of spectrometer A and B and the design parameters of the spectrometers are given in table 3.1.

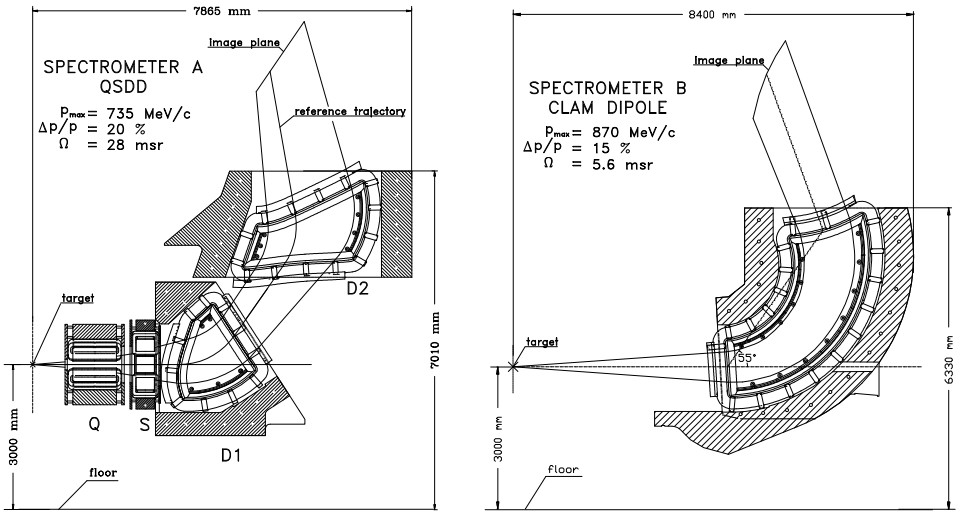

Figure 3.4.: Dimensions and layout of spectrometers A and B. Spectrometer C has the same configuration as spectrometer A but is scaled down to roughly 80% [69].

Table 3.1.: Optical properties of the three spectrometers.

	Unit	A	B	C
Configuration		QSDD	D	QSDD
Maximum Momentum	MeV/c	735	870	551
Reference Momentum	MeV/c	630	810	459
Central Momentum	MeV/c	665	810	490
Solid Angle	msr	28	5.6	28
Momentum Acceptance		20%	15%	25%
Momentum Resolution		10^{-4}	10^{-4}	10^{-4}
Angular Resolution at Target	mrad	<3	<3	<3
Position Resolution at Target	mm	3-5	1	3-5

3.2.2. Detector system

Each spectrometer holds the same standard set of detectors that consists of four layers of vertical drift chambers (VDC), two planes of plastic scintillators and a gas Čerenkov detector. They are enclosed in a shielding house which can be opened to access the detectors, see figure 3.3. A drawing of the detectors is shown in figure 3.5. The detector package and housing are build as a modular system, individual detectors are exchangeable. On spectrometer A for instance, the Čerenkov detector can be replaced by a proton polarimeter.

Vertical Drift Cambers

Two pairs of VDCs serve as focal-plane track detectors to reconstruct the trajectory of passing particles. Each VDC package consist of one x-layer with wires perpendicular to the dispersive plane and one s-layer, where the wires are rotated by 40° with respect to the x-wires. A schematic representation of a single VDC layer is given in figure 3.6.

Cathode foils are placed on either side of a plane of alternating signal and potential wires. The wires are connected to ground potential and a negative voltage between 5.6 kV and 6.5 kV is applied to the cathodes. A mixture of equal parts isobutane and argon is used as counting gas for the VDC. It contains a 1.5% admixture of pure ethanol to minimize aging. When a charged particle passes the gas, it creates electron-ion-pairs along its path. The ions are accelerated towards the cathode and the electrons towards the wires. Near the signal wires, the electric field strength is large enough for the free electrons to cause secondary ionization. The resulting electron avalanches that reach the signal wire create a measurable electric signal. The readout of the signal wires is done in a common stop mode. The first signal

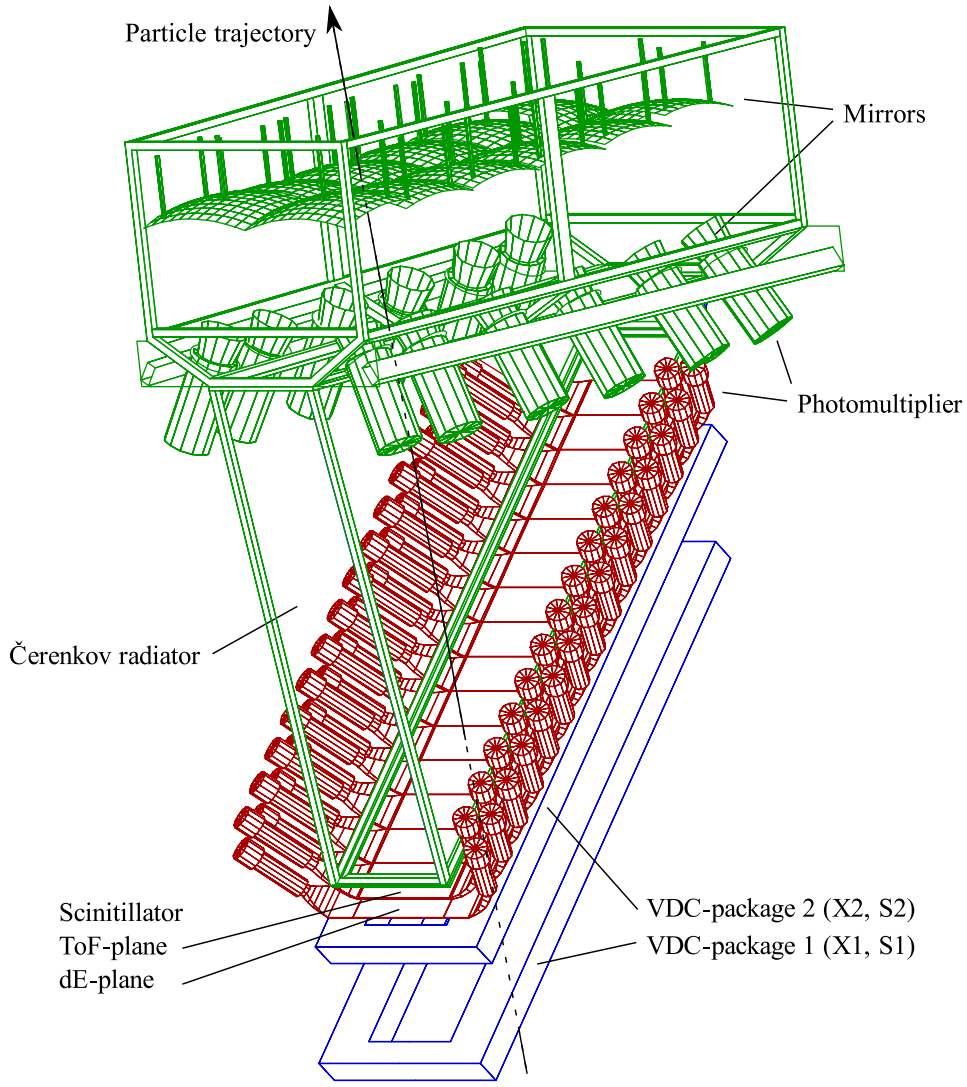

Figure 3.5.: Outline of the detector package. The VDCs a shown in blue, the scintillators in red and the Čerenkov detector in green. Incoming particles pass this setup from the bottom to the top. Figure from [18], original in [69]

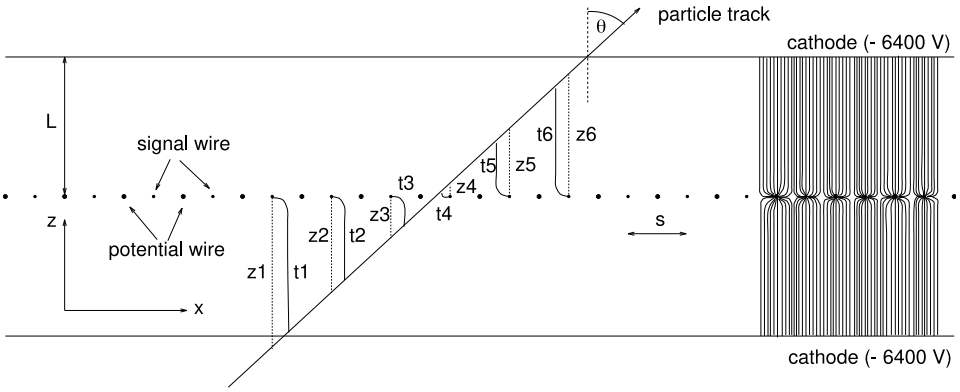

Figure 3.6.: Schematic drawing of one VDC layer. The distance L from the wires to the cathode foils is 12 mm and the gap between two wires is $s = 2.5$ mm. The time it takes the electrons to drift to the wires along the paths t1 to t6 is the measured drift time, from which the corresponding distances z1 to z6 are calculated. On the right, the electric field distribution is shown [69].

on each wire starts a time measurement that is stopped by the delayed scintillator signal. From the measured drift time, the distance of the particle track to each wire is calculated. The drift time depends on a number of parameters that change over time, like the mixture, temperature and pressure of the gas or the high voltage. Therefore, the drift chambers should be calibrated to get the best resolution possible. This process is described in section 6.1. An in-depth description of the VDCs is given in [70].

The focal plane coordinates determined by the VDC need to be translated to the target coordinates. These are the relevant parameters of the scattered particle, the momentum, the vertex position and the two Cartesian angles. This is done by transfer matrices, which are a parameterization of the spectrometers optical properties. Further details can be found in appendix A.

Scintillators

Two segmented planes of plastic scintillators are used as a trigger for the data acquisition system and for coincidence timing between the spectrometers. The fast signal of the scintillators also provides the common stop signal for the time measurement in the drift chambers. In the case of spectrometer A and C, the two planes consist of 15 segments each and are read out by photomultiplier tubes from both sides. Because of the smaller focal plane in spectrometer B, there are only 14 segments and a one-sided readout for the lower plane is sufficient. The segmentation not only improves the time resolution, but also provides a rough estimate of the position of

the particle track. The lower and upper plane are labeled “dE” and “ToF” and have a thickness of 3 mm and 10 mm, respectively. Usually, the ToF-plane defines the timing, but for heavy particles with low momenta the signal of the dE-plane can be used as well. The different energy loss in the two planes enables the separation of heavy particles like protons or deuterons form electrons, positrons and pions.

Čerenkov Detector

A gas Čerenkov detector completes the standard detector package. Its main purpose is to discriminate between electrons or positrons and pions. The gas in use is Hexafluoropropane ($C_3H_2F_6$) with a refractive index of $n = 1.001045$. This sets the threshold for the emission of Čerenkov light at 11 MeV for electrons and positrons. The emitted Čerenkov light is reflected by spherical mirrors onto photomultiplier tubes. Because the threshold for pions is above 3 GeV, heavier charged particles can not be produced at MAMI with sufficient energy to cause a signal in the detector. The Čerenkov detector can also be included in the trigger, which was necessary for this experiment, see sections 4.3 and 6.2.

3.2.3. Targets and Scattering Camber

The scattering chamber that contains the targets for the experiment is located at the spectrometers center of rotation. An exchangeable lid allows to install gas or cryo targets. A cryo target with liquid hydrogen at 22 K and 2 bar was used as a proton target. Figure 3.7 shows a schematic of the scattering chamber with the cryo target. The target is cooled by an outer loop connected to a Phillips compressor. The compressor liquefies hydrogen that flows down to the heat exchanger through a transfer line. Coupled to the heat exchanger is the inner loop (Basel-loop), filled with the liquid target material. Cylindrical target cells in various sizes, as well as a cigar shaped cell are available to be installed in the inner loop. A cylindrical cell with 2 cm outer diameter and a wall thickness of 10 μm of Havar foil was used in this experiment. Havar is an alloy with the main components cobalt, chromium, iron, nickel, tungsten, molybdenum and manganese. To prevent local density fluctuations in the hydrogen due to the heat load of the electron beam, a ventilator recirculates the liquid in the inner loop. The beam was additionally rastered over the target cell to further reduce local overheating. Since the thin Havar foil can not hold the weight of the target loop, a retaining bracket (figure 3.7) stabilizes the target cell. It can only be mounted facing the side of spectrometer A and cuts into the acceptance of spectrometer A at an angle of 110° and above. Especially the large backward angles are important for this measurement, so a new retaining bracket was designed

to increase the measurable angle range to 120°. The new bracket has slanted edges and is mounted at a greater distance from the target cell.

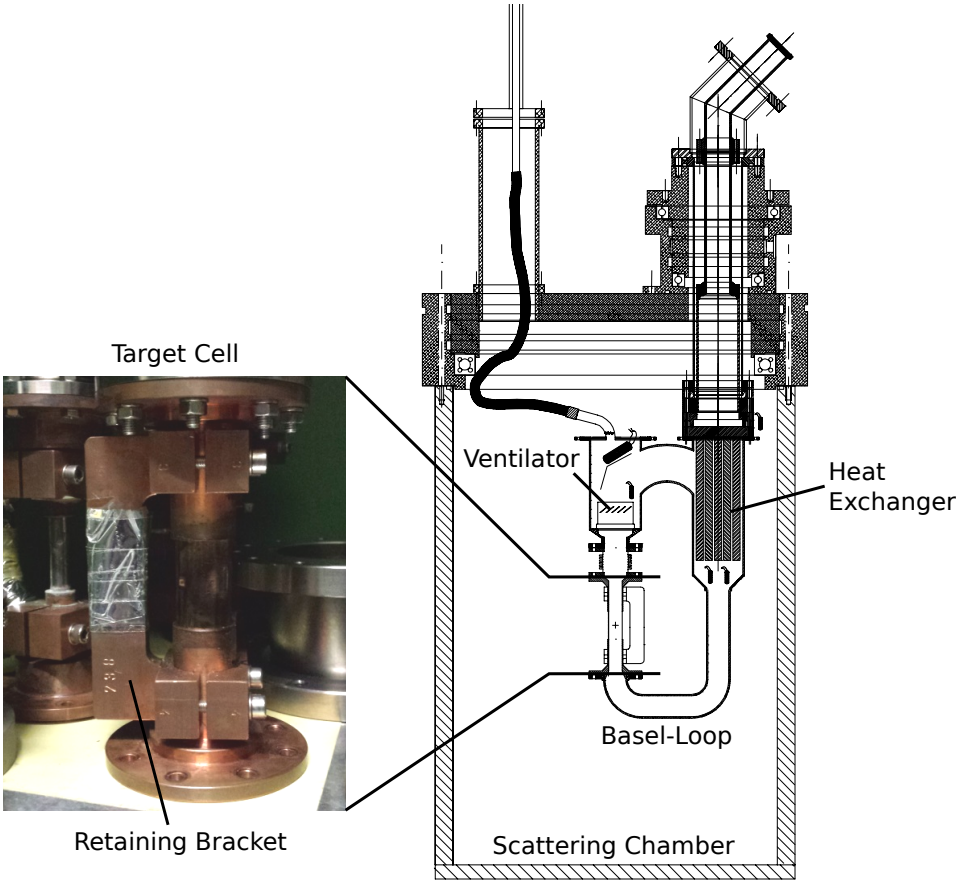

Figure 3.7.: The picture on the left shows the cylindrical target cell. A Schematic of the cryo target is on the right. From this perspective, the hydrogen is circulated clockwise by a ventilator in the inner loop. Technical drawing from [71].

The scattering chamber also houses a target ladder for solid state targets, figure 3.8. It can be moved vertically into the beam to select the different targets. The ladder always contains a luminescent screen (an Al_2O_3 plate) for beam position calibration, as well as a carbon target as a robust general purpose target for beam and detector tests. An empty target cell for background measurements was mounted on top of the target ladder. The empty cell was built with a wall thickness of 30 μm Havar to roughly match the radiation length of the hydrogen filled cryo cell. One can therefore expect a similar amount of energy loss and multiple scattering of the electrons in both targets.

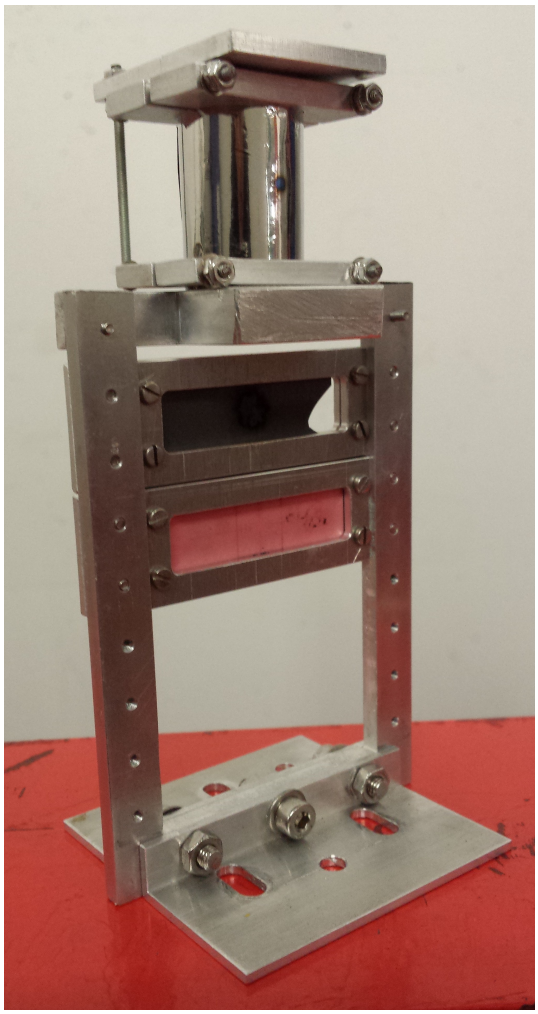

Figure 3.8.: Target ladder with the empty target cell (top) for background measurements, a carbon target (middle) and a luminescent screen (bottom). The screen has a printed on cross hair for beam position calibration.

4. Measuring Program

4.1. Measured Kinematics

As described in section 2.1, a separation of the form factors G_E and G_M at a given value of Q^2 via the Rosenbluth method can be achieved by measuring at different ε. This is not imperatively required when using a global fit. The number of data points at different ε in the Q^2 range of interest nevertheless improves the precision of the separation. To get cross section data for various ε and Q^2, the beam energy and the scattering angle need to be changed.

Setups were measured at seven beam energies between 720 MeV and 1508 MeV. Even though a change of the beam energy at MAMI can be done comparatively quickly and takes about three hours, the assigned beam time did not allow to measure at additional energies. It was also decided not to measure at 1600 MeV, because of the extremely low counting rates at backward angles and the already high background in the hall at 1508 MeV. This would require additional testing and a dedicated beam time. Since spectrometer A has the largest accessible angular range in the standard setup, all settings were measured with this spectrometer. The angular range for spectrometer A is limited by the maximum detectable momentum at low angles and is restricted to 120° by the construction of the target at large angles. The acceptance of spectrometer A is $\pm 100\,\text{mrad} \approx \pm 5.73°$ in the non-dispersive direction. Angles were chosen in steps of 3° to have an overlap between two setups. For each new angle, the momentum was changed to match the elastic scattering kinematics. This takes about 20 minutes, which is the necessary time for the magnets to settle. Spectrometer B was used with reverse polarity providing the great opportunity to detect recoiled protons for coincidence measurements, see sections 4.3 and 6.2. Spectrometer C remained constant at an angle of 105° for the whole beam time to serve as a backup luminosity monitor. 26 days of beam time between April and June 2015 were assigned to this experiment. The number of settings was chosen to collect enough statistics for each setup to reach a relative statistical error of about 0.3% or better. At least one 30 minutes long data run was taken for each setup. The low counting rates at the higher energies made multiple measurements of the same setup necessary.

Figure 4.1 shows all measured kinematics with spectrometer A. The unmarked settings had to be excluded in the final analysis. It was discovered that spectrometer

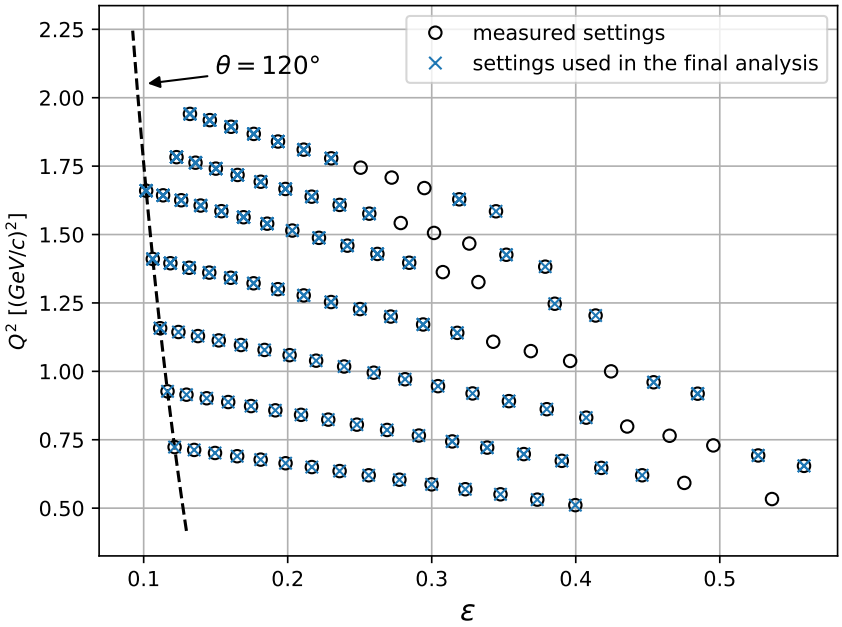

Figure 4.1.: Measured settings in the ε-Q^2-plane. The kinematic constraint do to the maximum spectrometer angle of 120° is indicated by a dashed line. The unmarked setups had to be excluded in the final analysis. For details see text and appendix A.

A has a discontinuity in the current of the quadrupole at the field intensity that corresponds to a central momentum of 576.19 MeV/c. At this value the current in the quadrupole coils changes abruptly by about 2%, and thus, the magnetic field as well. This is caused by an error in the software for the control of the coil drive current. The discontinuity renders the standard transfer matrix, which was calibrated at a central momentum of 495 MeV/c unusable beyond 576.19 MeV/c. The only available transfer matrix above the discontinuity was calibrated for the maximum central momentum of 655 MeV/c. It is only valid for high field intensities close to the maximum, because saturation effects in the iron yoke change the optics of the spectrometer. As a result, the discontinuity entails an area in the detectable momentum range where the calibration of the optics is not good enough for a precise cross section measurement. Further detail on the effect of the discontinuity is given in appendix A. Table 4.1 summarizes the measured kinematics that were used in the analysis. Not listed in the table are the measurements with the empty target cell for background studies, which have been done for selected settings. Because of the excluded settings the original plan for the analysis of the data could not be followed, which is why also external data was used for the final result, see section 7.7.

Table 4.1.: Overview of the measured settings and the total number of individual measurements. The scattering angles were changed in steps of 3°.

Beam Energy [MeV]	Angle Range	Settings	Measurements
720	78° - 120°	15	15
855	72° - 120°	17	22
1002	60°, 63°, 75° - 120°	18	22
1158	66°, 69°, 84° - 120°	15	49
1308	72°, 75°, 87° - 120°	14	60
1402	75°, 78°, 90° - 114°	11	47
1508	78°, 81°, 93° - 111°	9	54

4.2. Overlap with the previous Experiment from 2010

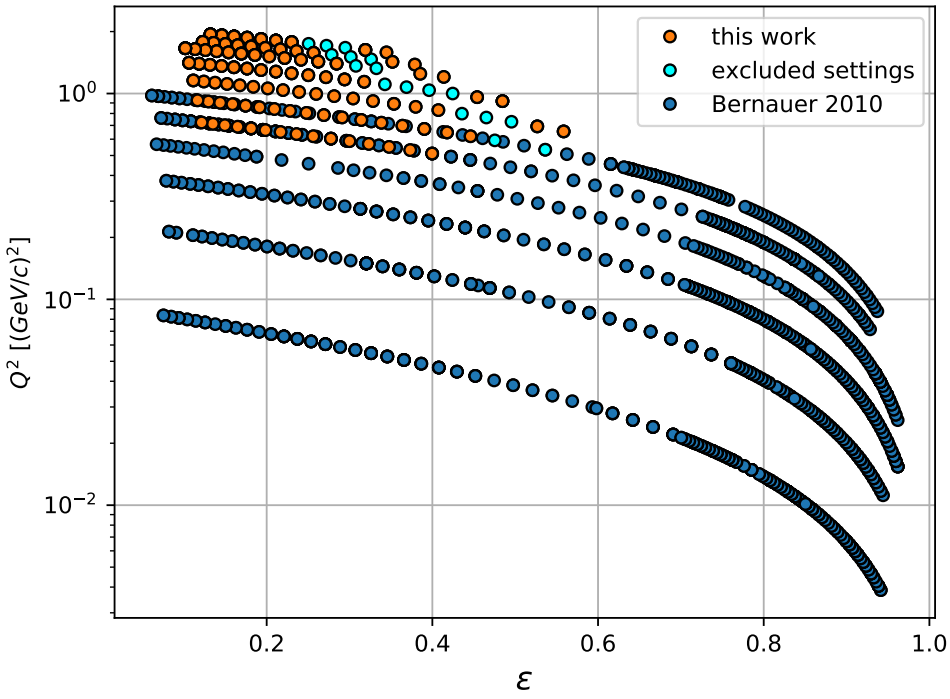

Figure 4.2.: Full MAMI data set of elastic electron-proton scattering. The two experiments have overlapping settings at the beam energies 720 MeV and 855 MeV. The settings which were excluded from the analysis in this work are shown in cyan.

Since the start of the planning of this experiment it was evident that the electric and magnetic form factors of the proton can not be determined precisely from the collected data of this experiment alone. With the current experimental setup it is

impossible to fix the normalization of the data with an error below one percent. The fact that the form factors are normalized at $Q^2 = 0$ to be 1 and μ_p for G_E and G_M, respectively, can be used to obtain the normalization from the data themselves. This however requires cross section data at sufficiently low Q^2. Thus, the kinematics of this experiment was laid out to tie in with the previous experiment at MAMI and A1 from 2010, where the elastic electron-proton cross section has been measured down to a Q^2 of $0.004\,(\mathrm{GeV/c})^2$ [18]. The two measurements have overlapping setups at the beam energies 720 MeV and 855 MeV. The full set of the MAMI elastic electron-proton scattering data is shown in figure 4.2. In the 2010 experiment, the setups were measured at six beam energies between 180 MeV and 855 MeV in 135 MeV steps. All three spectrometers were used to take data. The spectrometer angle between setups was changed by 2.5° for spectrometer A and C and by 0.5° for spectrometer B. The complete MAMI data set will be used in the analysis to extract the electric and magnetic form factors of the proton.

4.3. Čerenkov Trigger

The A1 spectrometer setup was specifically designed with coincidence measurements in mind. It is known that the shielding of the detectors is not enough to completely block all particles related to machine background. Neutrons created in the target material or in the beam dump can penetrate the detector shielding and cause a signal in the scintillators. For most experiments this does not pose a problem. This measurement, however, faced the extreme conditions of high beam energies and a high density target combined with the need for high beam currents, because of the low counting rates at backward angles. The huge radiation level in the hall caused by the simultaneous occurrence of these circumstances was underestimated in the preparation of the beam time. To reduce the background to a reasonable amount, the trigger condition was changed. Normally, only the signal of the upper scintillator plane "ToF" is used as trigger. Using a coincidence of both scintillator planes "dE" and "ToF" is in principle a feasible way to effectively reduce neutron events, because these particles typically deposit a significant amount of energy only in one scintillator layer through charge exchange reactions. This, however, was not an option since the efficiency of the thin dE-plane in spectrometer A has deteriorated too drastically over the long run of the A1 experiment. Instead the trigger condition was changed in spectrometer A and C to a coincidence of the ToF-plane and the Čerenkov detector (ToF & Č). To be able to determine the Čerenkov trigger efficiency, additional, dedicated coincidence settings had to be measured which allow to compare the two trigger conditions ToF and ToF & Č in a quasi background free measurement. The efficiency of the Čerenkov trigger is the topic of section 6.2.

5. Simulation

5.1. Introduction

In this chapter, the simulation of the cross section measurement is described. The simulation is performed with the A1 software package *Simul++*, which is based on Monte Carlo sampling. For the analysis of the cross section data, three separate simulations are performed for each data run: A hydrogen simulation for signal events and one simulation each for elastic and quasi-elastic background events from the wall of the cryo target cell. A precise description of the radiative tail in the simulation allows to extract the Born cross section from the measurement, by dividing the measured cross section by the hydrogen simulation (section 7.1). This way, the included radiative corrections in the simulation cancel out. The event generator for the generation of the radiative tail is described in detail in section 5.3.1. The elastic and quasi-elastic simulations are used for the background subtraction.

5.2. Monte Carlo Integration of the Cross Section

Monte Carlo Integration is a technique to numerically integrate a multidimensional function $f(x)$ over a finite volume V. The integral can be expressed by the mean value

$$\langle f \rangle = \frac{1}{V} \int_V f(x)\, d^n x\,. \tag{5.1}$$

An estimate for the mean value is given by

$$\langle f \rangle \approx \frac{1}{N} \sum_{i=1}^{N} f(x_i) \tag{5.2}$$

where the x_i are a random sample of points in V. The integral is then calculated by

$$I = \int_V f(x)\, d^n x = V \langle f \rangle \approx \frac{V}{N} \sum_{i=1}^{N} f(x_i) \tag{5.3}$$

The error σ_I of the approximation of the integral I depends on the variance of f:

$$\sigma_I = \frac{V}{\sqrt{N}} \sqrt{\langle f^2 \rangle - \langle f \rangle^2}\,. \tag{5.4}$$

For an accurate and efficient integration it is therefore desirable to reduce the variance of f. Instead of drawing random samples from a uniform distribution, one can generate events according to a distribution which is similar to the integrand. This method is called importance sampling [72]. In this way, one can obtain the same accuracy with a smaller sample size. Connected with this is the question of how a random variable from a uniform distribution can be transformed into a random variable that follows a given distribution. This can be achieved with the inverse transformation method [72]. If $f(x)$ is a probability density function, the cumulative distribution function (CDF) is given by

$$\int_{-\infty}^{x} f(t)\,dt = F(x) = u \tag{5.5}$$

where u is in the interval $[0, 1]$. Solving this equation for x yields

$$x = F^{-1}(u) \tag{5.6}$$

with the inverse function $F^{-1}(u)$. If u is now a random variable with a standard uniform distribution, the random variable x is distributed according to $f(x)$.

The simulation makes use of Monte Carlo integration to simulate the number of measured events for a given cross section $\frac{d\sigma}{d\Omega}$ inside the experiment specific acceptance. The number of events n measured in a time period T is given by

$$n = \int_T \int_{\Delta\Omega} A(\Omega)\,\frac{d\sigma}{d\Omega}(\theta)\,L(t)\,d\Omega\,dt \tag{5.7}$$

where A is the acceptance defined by the geometry of the spectrometer. It is considered to be constant over the short measuring time. The integral of the luminosity L over the measuring period is determined in the experiment (see section 7.5) and is an input parameter of the simulation. The integration over the solid angle, or the accepted phase space $\Delta\Omega$, is done by the simulation software *Simul++*.

5.3. Hydrogen Simulation

In section 2.2 the radiative corrections to the first order Born cross section were introduced. The radiative corrections have to be determined to extract the Born cross section from the measured cross section in the experiment. The experimental cross section

$$\left(\frac{d\sigma}{d\Omega}\right)_{\text{exp}} = \left(\frac{d\sigma}{d\Omega}\right)_0 f_{\text{corr}}(\Delta E', E, \theta) \tag{5.8}$$

consists of the lowest order cross section and a radiative correction factor that depends on the cut-off energy $\Delta E'$. To extract the cross section, a comprehensive

simulation is performed using an assumed cross section, based on current knowledge, with the known radiative corrections included. The simulation also accounts for external radiation like the energy loss of the electrons in the target material. If the measured cross section is then divided by the simulation, the included radiative corrections cancel out and one obtains the ratio of the true cross section to the assumed cross section in the simulation. The simulation of an assumed cross section requires a suitable parameterization of the form factors. Here, the form factors from the spline fit to the world data from [20] are used.

Apart from the updated from factors, the simulation is essentially the same as described in [18]. The event generator is based on the concept from [55] and is documented in [73]. Since the simulation of the cross section is an important part of the analysis, the production of the radiative tail by the event generator is described here again.

5.3.1. Event Generator

The event generator in *Simul++* makes use of importance sampling to efficiently generate the kinematics. At each step, the algorithm updates the total weight and returns the final weight for each event, which has to be considered in the calculation of the cross section. The event generator was originally developed for simulating virtual Compton scattering events, therefore, the main diagram for the generator is not the basic one photon exchange graph in figure 2.1. Instead, the Bethe-Heitler diagrams (figure 2.2 top) and the Born diagrams (figure 2.4 top) are the primary diagrams. The generator precisely calculates these processes to accurately account for the emission of a real photon from the electron or the proton in the initial or final state. In the first step the angles $\cos\theta$ and φ of the scattered electron are generated uniformly. In that way, the scattered electrons are distributed uniformly over the spherical angular acceptance of the spectrometer. The energy of the emitted photon is then generated indirectly from the energy loss of the scattered electron $\Delta E'$. The contribution of the electron side to the radiative tail is only the first term from equation (2.23). By introducing the parameter

$$a = \frac{\alpha}{\pi}\left[\ln\left(\frac{Q^2}{m^2}\right) - 1\right], \tag{5.9}$$

the first term in equation (2.23) can be written as

$$\delta_{\mathrm{R}} = a\ln\left(\frac{(\eta\Delta E')^2}{EE'}\right) = a\ln\left(\eta\frac{(\Delta E')^2}{E'^2}\right), \tag{5.10}$$

where $\eta = \frac{E}{E'}$ is again the recoil factor. Here, E' is the energy of an elastically scattered electron into the generated angle. In the exponentiated form, the correction term becomes

$$e^{\delta_R} = \eta^a \left(\frac{\Delta E'}{E'}\right)^{2a} . \tag{5.11}$$

Now, one has to find a distribution that can be sampled to get the correct energy loss of the electron. The integration of this distribution over the energy loss up to the cut-off energy $\Delta E'$ must be equal to equation (5.11). Thus, the distribution has to satisfy

$$\int_0^{\Delta E'} I(x, E', t)\, dx = \left(\frac{\Delta E'}{E'}\right)^t \tag{5.12}$$

with $t = 2a$, if an event is weighted with η^a. This can be solved with the inverse transformation method from equations (5.5) and (5.6). The distribution that satisfies equation (5.12) is

$$I(\Delta E', E', t) = \frac{t}{\Delta E'} \left(\frac{\Delta E'}{E'}\right)^t . \tag{5.13}$$

Events according to the distribution in equation (5.13) can be generated with a random number r, uniformly distributed in $[0, 1]$ and calculating the variable

$$\Delta E'(r) = E' r^{1/t} . \tag{5.14}$$

The proton contribution to the radiative tail can be treated in the same way. The first part of each of the two contributions δ_1 and δ_2 (equations (2.26) and (2.27)) depend on $\Delta E'$:

$$\delta_1 = \frac{2\alpha}{\pi} \ln\left(\frac{4(\eta \Delta E')^2}{Q^2 x}\right) \ln \eta \tag{5.15}$$

$$\delta_2 = \frac{\alpha}{\pi} \ln\left(\frac{4(\eta \Delta E')^2}{M_P^2}\right) \left(\frac{E'_P}{|\vec{p}'_P|} \ln x - 1\right) \tag{5.16}$$

Similar to the case of the electron before, the proton corrections in the exponentiated form can be written as

$$e^{\delta_1} = \left(\frac{4E^2}{xQ^2}\right)^b \left(\frac{\Delta E'}{E'}\right)^{2b} \tag{5.17}$$

$$e^{\delta_2} = \left(\frac{4E^2}{M_P^2}\right)^c \left(\frac{\Delta E'}{E'}\right)^{2c} \tag{5.18}$$

with the parameters

$$b = \frac{\alpha}{\pi} 2 \ln \eta , \quad c = \frac{\alpha}{\pi} \left(\frac{E'_P}{|\vec{p}'_P|} \ln x - 1\right) . \tag{5.19}$$

The electron contribution from equation (5.11) and the proton contributions from equations (5.17) and (5.18) depend on $\Delta E'$ in the same way. The three parts can

therefore be added directly

$$t = 2a + 2b + 2c \tag{5.20}$$

to generate the energy loss of the scattered electron, where each event has the weight factor

$$\eta^a \left(\frac{4E^2}{xQ^2}\right)^b \left(\frac{4E^2}{M_P^2}\right)^c . \tag{5.21}$$

The next step is to generate the direction of the radiated photon. The cross section for photon emission off an electron varies greatly with the angle and is peaked heavily in the direction of the incident or scattered electron. Generating the spherical direction uniformly would therefore be highly inefficient. The angles are instead generated from a distribution that approximates the Bethe-Heitler cross section.

$$\frac{d\sigma}{d\Omega} = \frac{1}{2}\left(\frac{d\sigma}{d\Omega}\right)_e + \frac{1}{2}\left(\frac{d\sigma}{d\Omega}\right)_{e'} \tag{5.22}$$

where the probability for emitting a photon is assumed to be equal for the incoming and scattered electron. The cross section for the incoming electron is given by

$$\begin{aligned} \left(\frac{d\sigma}{d\Omega}\right)_e &= \frac{1}{N(E,\vec{p})} \frac{1-\cos^2\theta_{e\gamma}}{\left(\frac{E}{|\vec{p}|} - \cos\theta_{e\gamma}\right)^2}, \\ N(E,\vec{p}) &= -4 - 2\frac{E}{|\vec{p}|}\ln\left(\frac{\frac{E}{|\vec{p}|}-1}{\frac{E}{|\vec{p}|}+1}\right) \end{aligned} \tag{5.23}$$

where $\theta_{e\gamma}$ is the angle between the incoming electron and the photon. Substituting $E, p, \theta_{e\gamma} \to E', p', \theta_{e'\gamma}$ in equation (5.23) gives the part for the scattered electron. Using again the inverse transformation method, one can generate values according to equation (5.23) with a random variable r uniform in $[0,1]$ by calculating $\theta_{e\gamma} = F^{-1}(r)$. The cumulative distribution function $F(\theta_{e\gamma})$ of equation (5.23) is

$$\begin{aligned} F(\theta_{e\gamma}) &= \int_1^{\cos\theta_{e\gamma}} \left(\frac{d\sigma}{d\Omega}\right)_e d\cos\theta \\ &= \frac{1}{N}\left[\frac{1-\left(\frac{E}{|\vec{p}|}\right)^2}{\frac{E}{|\vec{p}|} - \cos\theta_{e\gamma}} - \cos\theta_{e\gamma} - 2\frac{E}{|\vec{p}|}\ln\left(\frac{\frac{E}{|\vec{p}|} - \cos\theta_{e\gamma}}{\frac{E}{|\vec{p}|}+1}\right) - 2 + \frac{E}{|\vec{p}|}\right] . \end{aligned} \tag{5.24}$$

The inversion of the function F in this case is done via bisection. The approximate Bethe-Heitler cross section is only used for the generation of the angles. An event has to be weighted by the inverse of equation (5.22) to divide out the approximation. The kinematic properties of the scattered electron and the emitted photon are fixed at this point. The generator then proceeds with the calculation of the Bethe-Heitler

diagrams (figure 2.2 top) and Born diagrams (figure 2.4 top) for the lowest order cross section of the $e\,p \to e'p'\gamma$ process.

5.4. Background Simulation

The main background in this experiment arises from elastic and quasi-elastic scattering on the atoms in the wall of the cryo target cell. Elastic and quasi-elastic scattering are simulated separately and independently from each other. The cryo target cell is a thin foil of Havar, which is an alloy with the main components cobalt, chromium, iron, nickel, tungsten, molybdenum and manganese. For each simulated background event a type of target nucleus is selected according to the quantity ratio of the constituent nuclei of Havar. The radiative tail is generated similar to the hydrogen simulation. The charge distribution of the nuclei

$$\rho_H(r) = \rho_S(r, R) * \rho_G(r, \sigma) \tag{5.25}$$

is approximated by a convolution of a homogeneously charged sphere ρ_S and a Gaussian distribution ρ_G. This model is often called Helm's model. The values for the radius R of the sphere and the sigma of the Gaussian are taken from [74]. The form factor is then the Fourier transform of $\rho_H(r)$

$$F_H(q) = F_S(q) \cdot F_G(q)\,, \tag{5.26}$$

which is a product of the two components according to the convolution theorem. Quasi-elastic scattering is calculated with the de Forest off-shell cross section [75]. Both the model for elastic scattering, as well as the model for quasi-elastic scattering do not produce an absolute cross section, but only produce the correct shape. The amplitude has to be fitted to the data, which is described in section 7.4.

5.5. Combining the models

The simulation contains parameters to simulate the resolution of the detector. They control the width of the distributions of the simulation and need to be adjusted to match the data. With optimized resolution parameters, the combination of the hydrogen and the two background simulation parts can describe the data very well. This can be seen for the $\Delta E'$ spectrum of a measurement at 60° and 1002 MeV in figure 5.1. The figure shows the absolute difference of the $\Delta E'$ quantity between data and the sum of the hydrogen and background simulation in the lower plot. The process of matching the simulation to the data and optimizing the resolution parameters is described in section 7.4.

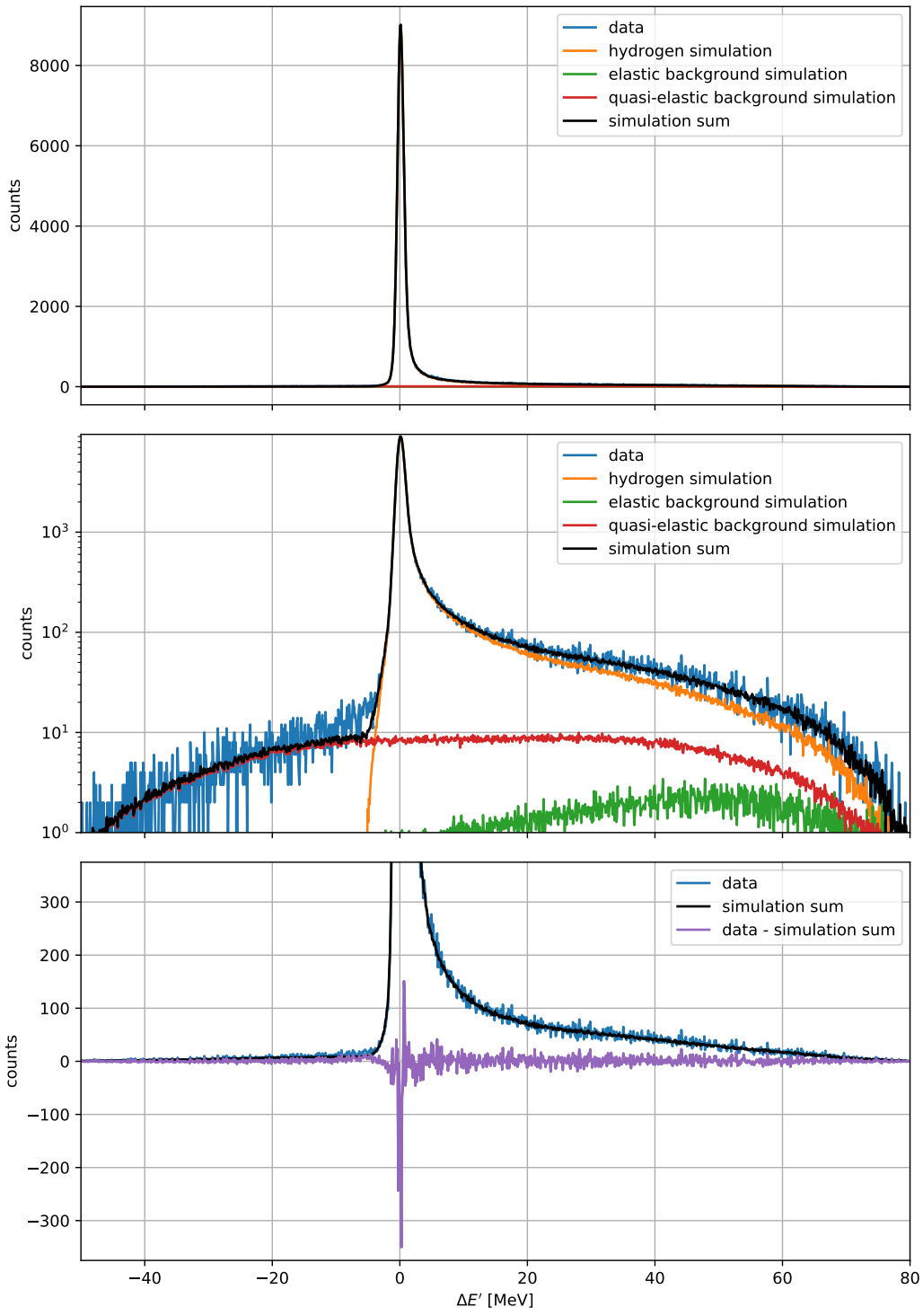

Figure 5.1.: Hydrogen and background simulation for a measurement at 60° and 1002 MeV in linear representation (top) and logarithmic representation (middle). The plot on the bottom shows the absolute difference between data and the sum of the three simulations.

6. Detector Calibration

6.1. VDC Calibration

The raw data from the experiment is stored in run files. They contain the full detector information for each event, such as the VDC wires that have fired or which scintillator bars have been hit. The run files are analyzed with the A1 software package Cola++ (Cindy OnLine Analysis). One of its tasks is the reconstruction of the particle trajectories from the information of the VDC. The algorithm for the track reconstruction needs the drift velocity and a drift time offset as input parameters. Both parameters depend on the characteristics of the VDC, like the gas mixture, temperature, pressure and the high voltage, which change over time. The drift velocity and drift time offset thus have to be optimized for each individual measurement. The reconstruction algorithm provides an error estimate for the reconstructed focal plane coordinates. This is shown in figure 6.2 using the non-dispersive angle φ as an example. From the histogram of the estimated error, the product of the width and the position of the peak is used as the optimization variable. SciPy's implementation of the Nelder-Mead method was used for the optimization process. The process was done in two steps. First, the error of the reconstructed x-coordinate was minimized by varying the drift velocity and the TDC offsets for the two x-layers. In the second step, the TDC offsets and a correction factor for the drift velocity for the s-layers were varied to minimize the error of the y-coordinate. This correction factor was introduced because of the rotation of the wires in the s-layer by 40° with respect to the x-wires. The calibrated drift velocities for spectrometer A are shown in figure 6.1.

The two apparent peaks are caused by a replacement of the isobutane bottle. An interpretation is that small impurities enter the system in the process. These are possibly residual gasses, lighter than isobutane, that accumulate at the top of a new bottle. A blow-off of some isobutane can mitigate this issue in some cases. An incident like this changes the drift velocity up to about 5%. Figure 6.2 shows the impact of such a change on the error estimate of the non-dispersive angle φ in the focal plane. Without calibration, a shift of the peak position and a broadening of the histogram are evident. Because the information from all four VDC layers is needed to calculate φ, the estimated error for this angle is a good indicator for the overall effectiveness of the optimization.

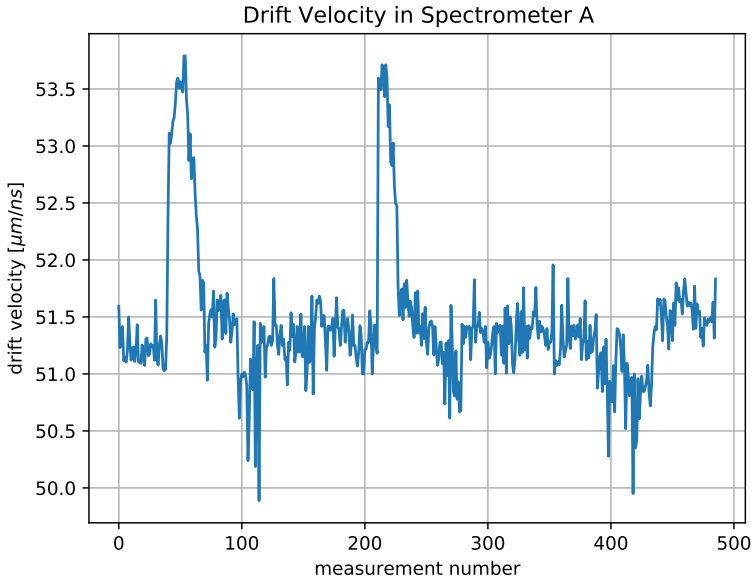

Figure 6.1.: The calibrated drift velocity for each measurement of the experimental campaign. The two peaks occurred after the isobutane bottle was changed.

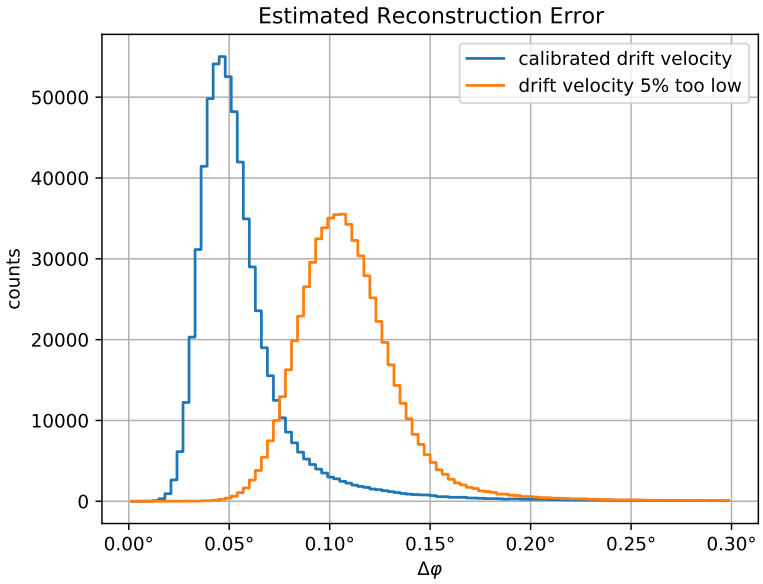

Figure 6.2.: Estimated reconstruction error for the non-dispersive angle φ. The same measurement is shown, once with a calibrated drift velocity and once with a drift velocity that is 5% too low. Replacing an isobutane bottle can cause an effect of this magnitude.

6.2. Čerenkov Trigger Efficiency

The trigger condition in the experiment was changed from the standard upper scintillator plane only (ToF), to a coincidence of this scintillator layer and the Čerenkov detector (ToF & Č). This was a necessary step to reduce the background, see section 4.3. To investigate the trigger efficiency of the Čerenkov detector, coincidence settings were measured. Elastically scattered electrons were detected in spectrometer A in coincidence with the knocked out protons, out of the hydrogen target, in spectrometer B. This setup ensures a quasi background free measurement, where only random coincidences can accompany the reaction of interest. Each setting was measured with the two trigger conditions ToF and ToF & Č. Since the angular acceptance in the non-dispersive direction of spectrometer A is larger than the one of spectrometer B, coincidence events are only detected in a subarea of the focal plane in spectrometer A. Therefore, spectrometer B was moved to different angles while spectrometer A remained at a fixed angle for a scan across the focal plane in A. This procedure was repeated on several days of the beam time, to be able to identify changes over time. A total of 18 settings were measured at the kinematics listed in table 6.1.

Table 6.1.: Settings for the electron-proton coincidence measurements.

Beam Energy [MeV]	Momentum of Spec. A [MeV/c]	Angle of Spec. A	Angle Range of Spec. B
720	479.9	72°	35.4°, 40.5°
855	651.8	51°	43.9°, 51.6°
855	616.4	57°	41.6°, 43.9°

The efficiency of the Čerenkov detector was expected to be very close to 100%. If this holds true, the spectra measured with the two trigger settings should coincide with each other, or in other words, the difference of the spectra should be compatible with zero. This was tested with a two-tailed χ^2-test with a confidence level of 95%. The test was performed twice for each setting with a different normalization procedure of the spectra, once the spectra were divided by the measured integrated luminosity and once the integral of the spectra was normalized to one. An example for a test with the luminosity as normalization is shown in figure 6.3.

Both test methods yield comparable results: Two out of the 18 settings were found outside of the confidence region. It should be noted that with a sample size of 18 and a confidence interval of 95%, one would expect the test to fail once, just on the basis of statistics. Furthermore, the instances where the test failed can be explained by a small shift of the magnetic field in spectrometer A between the two measurements.

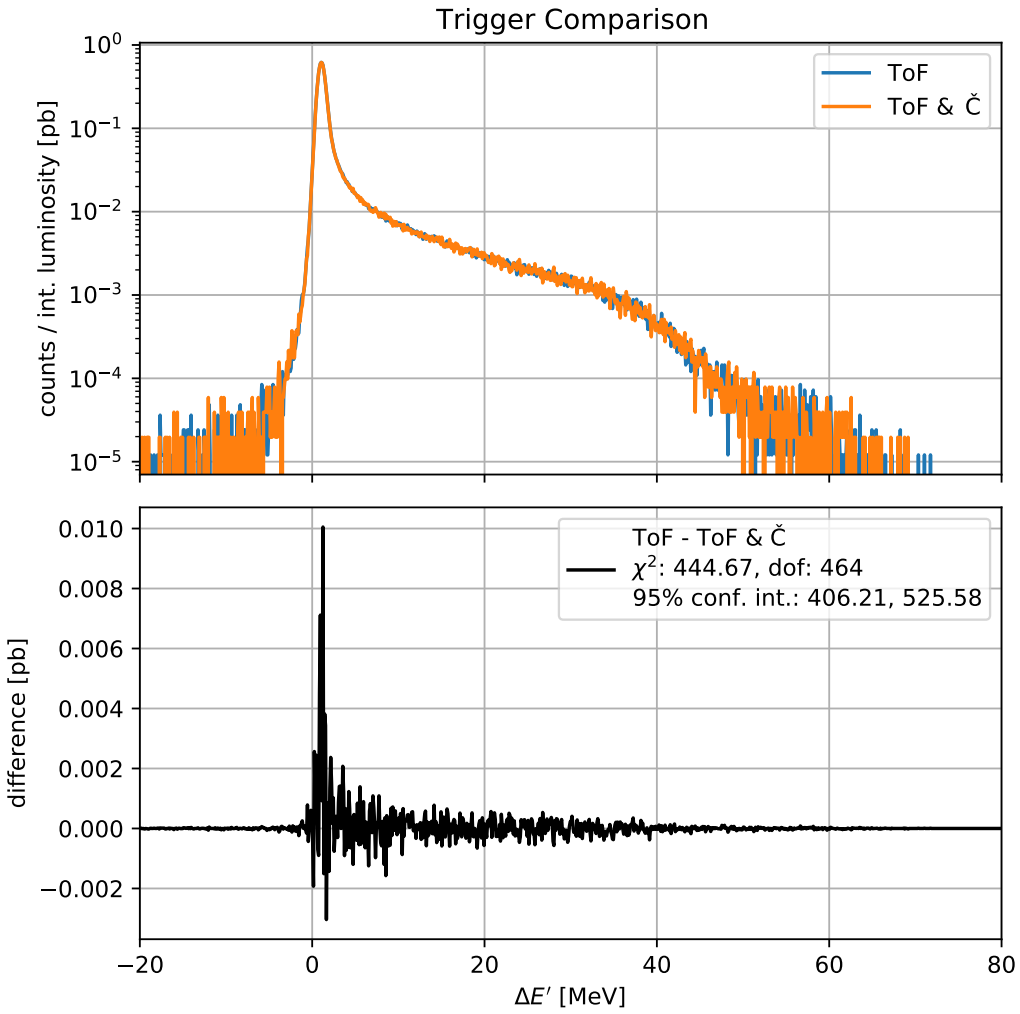

Figure 6.3.: Comparison of the trigger conditions scintillator only (ToF) and a coincidence of scintillator and Čerenkov detector (ToF & Č). Spectrometer A is at 57° and spectrometer B at 42.8°. The beam energy is 855 MeV. The χ^2-test shows that the difference of both spectra is indistinguishable from zero.

This would shift the spectra against one another along the x-axis. Indeed, the test is passed when repeated with a slightly shifted momentum for one of the two compared measurements. One can conclude that no statistically significant difference between the trigger conditions could be found. Since a possibly constant efficiency offset is already part of the global normalization, a correction factor solely for the efficiency of the Čerenkov was not applied to the data. What remains, is a possible change of efficiency for different positions of the elastic peak in the focal plane. This effect is accounted for in section 8.4.2 by a systematic error that covers the complete detector package.

7. Data Analysis

7.1. Method for Determining the Cross Section

The measured events and the luminosity are two of the outcomes of the analysis. One could then calculate the experimental cross section

$$\left(\frac{d\sigma}{d\Omega}\right)_{\text{exp}} = \frac{N_{\text{exp}} - N_B}{\Delta\Omega\, L_{\text{int}}}\,, \tag{7.1}$$

where N_{exp} is the number of measured events, N_B is the estimated background and L_{int} the luminosity integrated over time. This would require complete knowledge of $\Delta\Omega$, the integral over the acceptance of the spectrometer. The acceptance, however, is not known precisely enough as it is not just a constant factor. It does not only depend on the geometry of the collimator, but also on the length and position of the target, the angle of the spectrometer and the particle momentum. Apart from the acceptance, further complication poses the fact that the experimental cross section

$$\left(\frac{d\sigma}{d\Omega}\right)_{\text{exp}} = \left(\frac{d\sigma}{d\Omega}\right)_{0,\,\text{exp}} f_{\text{exp}}(\Delta E', E, \theta) = \frac{N_{\text{exp}} - N_B}{\Delta\Omega\, L_{\text{int}}}\,, \tag{7.2}$$

is not equal to the leading order Born cross section, but also contains higher order radiative terms $f_{\text{exp}}(\Delta E', E, \theta)$ like the ones discussed in section 2.2. As mentioned in section 5.3, these contributions give rise to a radiative tail that has to be determined to extract the lowest order cross section. The best possible way to handle these difficulties is a comprehensive simulation including the detector acceptance, the known radiative corrections and in this context also external radiation, like the energy loss of the electrons in the target. Analogous to equation (7.2), the cross section for the simulation is

$$\frac{N_{\text{sim}}}{\Delta\Omega\, L_{\text{int}}} = \left(\frac{d\sigma}{d\Omega}\right)_{0,\,\text{sim}} f_{\text{sim}}(\Delta E', E, \theta)\,. \tag{7.3}$$

For the assumed cross section in the simulation, the form factors from the spline fit to the world data from [20] are used. The radiative correction factor f_{exp} in equation (7.2) can be divided into two parts

$$f_{\text{exp}}(\Delta E', E, \theta) = f_{\text{sim}}\, f_{\text{TPE}}\,, \tag{7.4}$$

which are the known radiative corrections included in the simulation f_{sim}, and the two photon exchange correction f_{TPE}. One can then determine the measured cross section relative to the simulation by dividing equation (7.2) by equation (7.3):

$$\left(\frac{d\sigma}{d\Omega}\right)_{0,\,\text{exp}} = \left(\frac{d\sigma}{d\Omega}\right)_{0,\,\text{sim}} \frac{N_{\text{exp}} - N_B}{N_{\text{sim}}} \frac{1}{f_{\text{TPE}}} \,. \tag{7.5}$$

This way, the known radiative corrections cancel out. The unknown radiative corrections not included in the simulation are assumed to be small, leaving only the TPE correction. The two models for the TPE correction presented in section 2.3 are applied to the data by hand.

The luminosity measured in the experiment is an input parameter for the simulation of the cross section. Although the luminosity does not appear explicitly in equation (7.5), the uncertainty of the luminosity still enters the final result. With the current experimental setup the luminosity can not be determined with sufficiently high precision for an absolute normalization of the cross section. The luminosity, which includes the detector efficiencies, the beam current calibration and the length of the target, is only known to the level of a few percent. The data of this experiment is therefore grouped into sets of data points. The luminosity is used for a relative, point-to-point normalization of the data points within the same set. In the final analysis the absolute normalization will be determined by a global fit, using the fixed normalization of the form factors at $Q^2 = 0$. One scaling parameter for each set of data points will be included in the fit. The fitting procedure is described in section 8.1.

7.2. Event selection

The quality of the recorded data can be improved by discarding background events and events from deficiently reconstructed particle tracks. As mentioned before, the raw data is analyzed by the A1 software *Cola++*. The program reconstructs the particle trajectories from the information of the VDC and calculates the target coordinates from the focal plane coordinates via the transfer matrix. It is also used to generate histograms of the important quantities and it allows to apply cuts to the data. Elastic events can be identified by the energy of the outgoing electrons. The energy of an elastically scattered electron, detected at an angle θ has the energy:

$$E'(\theta) = \frac{E}{1 + \frac{E}{M_0}(1 - \cos\theta)} \,. \tag{7.6}$$

Higher order radiative processes or energy loss in the target may lower the energy of the electron. One can calculate the difference

$$\Delta E' = E'(\theta) - E'_{\text{exp}} \tag{7.7}$$

of the expected energy $E'(\theta)$ from equation (7.6) and the detected energy E'_{exp} of the scattered electron. Figure 7.1 shows the $\Delta E'$ spectrum for two measurements at a beam energy of 1002 MeV with the spectrometer angles 87° and 111°. The elastic events form a sharp peak near zero, followed by a radiative tail to the right.

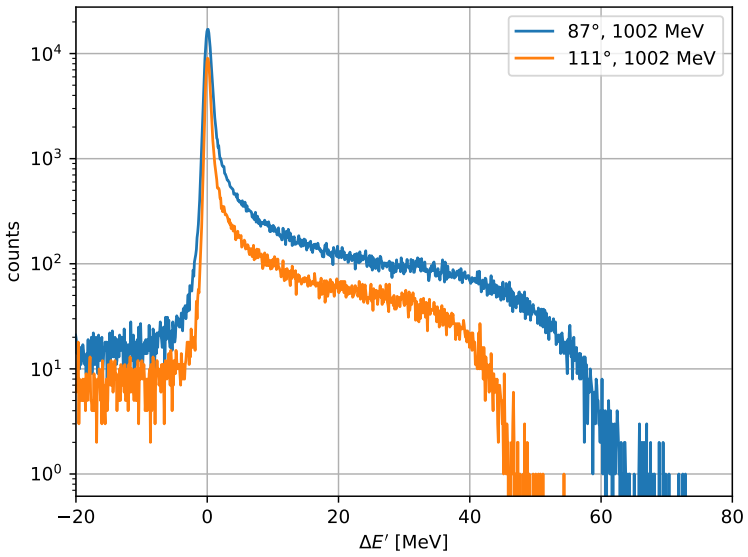

Figure 7.1.: $\Delta E'$ spectrum for two measurements at 1002 MeV beam energy at the spectrometer angles 87° and 111°. The energy where the spectrum drops to zero varies greatly with the angle and also with the beam energy. It is therefore difficult to cut away the lowest momenta at high $\Delta E'$ consistently across all settings.

Since the momentum acceptance of the spectrometer is not well defined by the collimator, the lowest and highest momenta have to be cut away. The low momenta correspond to the events with a high $\Delta E'$. As can be seen in figure 7.1, the energy where $\Delta E'$ drops to zero varies greatly between the two angles. The drop off also varies with the beam energy, which makes it difficult to cut away the highest momenta in the $\Delta E'$ histogram consistently across all settings. The preferable way is a cut in the relative momentum Δp, the difference of the particle momentum from the central momentum of the spectrometer. Figure 7.2 shows the Δp spectrum for the same two measurements like in figure 7.1. The shape of the Δp histogram is independent of the scattering angle and the beam energy. The same cut in Δp can

therefore be applied to all measured data runs. The cut condition

$$-5.3\% \leq \Delta p \leq 9\%$$

was chosen in the analysis.

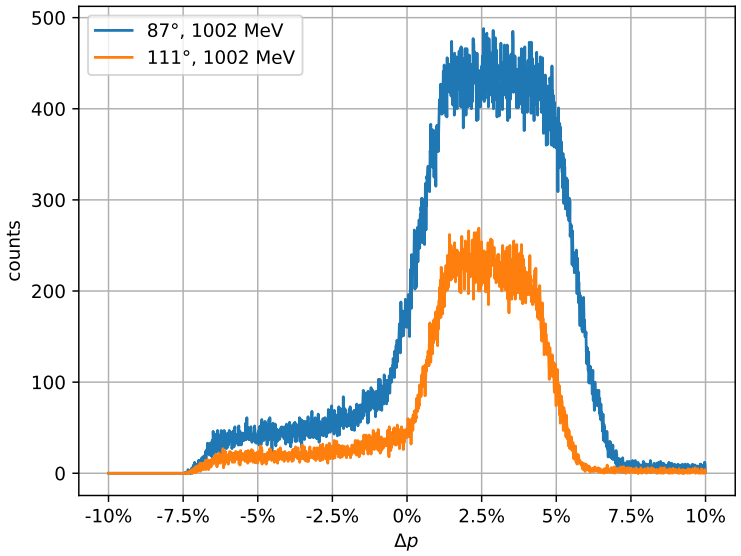

Figure 7.2.: The Δp for the same measurements like in figure 7.1. The shape of this histogram is similar for all settings, independent of the scattering angle and the beam energy. The same cut condition can therefore be applied to all measured data runs.

For extended targets like the cryo target cell, the angular acceptance of the spectrometer is not fully defined by the collimator. Particle trajectories with an interaction point far from the center of the target along the beam axis can have large in-plane angles. Such trajectories can pass the collimator, but are then lost inside the spectrometer without reaching the detectors, due to collisions with the pole pieces or the vacuum chamber. This can be avoided by reducing the acceptance of the spectrometer, so that no particles are lost in the magnet system. Spectrometer A is equipped with three collimators with solid angles 28.0 msr, 21.5 msr and 15.8 msr to reduce the nominal angular acceptance. By mistake the data for this experiment was measured with the largest collimator giving the full spectrometer acceptance. Particle tracks with large angles that pass through the corners of this collimator are lost in the spectrometer. This effect is clearly visible in the histogram of the accepted in-plane and out-of-plane angles Φ_0 and Θ_0 in figure 7.3. The data should have been measured with the small collimator which has an opening in-plane angle when looking from the center of the target of 6° and restricts the accepted angles to $\Phi_0 \approx \pm 4°$. The geometry of all collimators is parameterized in the simulation

software. To avoid a dependence of the vertex position in the data, the software cut that resembles the 15.8 msr collimator was also applied to the data. Unlike in the simulation, however, where the vertex and particle trajectory is known, the reconstruction of the trajectories is subject to errors due to the limited resolution of the spectrometer. Applying this collimator cut to the data introduces an additional systematic error that has to be considered in the analysis, see section 8.4.2.

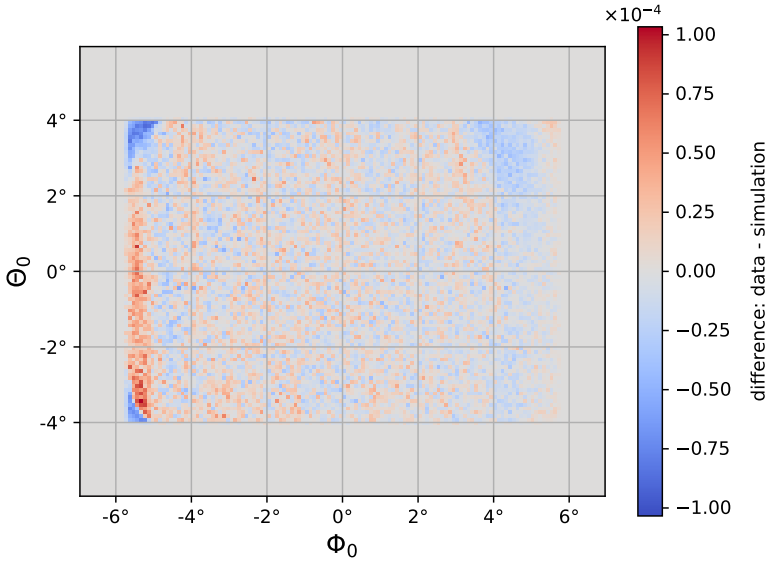

Figure 7.3.: The difference of data and simulation at 855 MeV beam energy and spectrometer angle 75°. Φ_0 and Θ_0 are the in-plane and out-of-plane angles in the target coordinate system. The sum of the histogram was normalized to 1 for the measured data and the simulation in each case in order to compare local deviations. Blue areas indicate an excess of simulated events. One can see that data events are lost in the corners of the acceptance, especially at the low Φ_0-angles.

7.3. Background Subtraction

In section 3.2.3 the cryo target was introduced. It was mentioned already that the liquid hydrogen is contained in a cylindrical cell made of Havar. The background in this experiment arises from elastic and quasi-elastic scattering on this cell. The elastic background is a superposition of several elastic peaks and their radiative tails, due to the different masses of the nuclei in the Havar foil. At high values of Q^2, like in this experiment, the difference in recoil between the heavy nuclei and the protons in the hydrogen is so large that the elastic background peaks are outside of the acceptance of the spectrometer. Even at the lowest measured Q^2 no background peaks can be seen and only their elastic tails contribute to the background. For

all settings measured in this experiment, the main background is caused by quasi-elastic scattering and is inevitably situated under the elastic hydrogen peak. The quasi-elastic spectrum is broadened by the Fermi motion inside the nucleus and is shifted towards smaller energies by the separation energy. The upper histogram in figure 7.4 shows a typical background spectrum. One can see the largest contribution coming from quasi-elastic scattering and a lesser amount coming from the tails of the elastic background peaks. A common way to separate data from background is via a kinematic cut. In a single arm experiment, like presented here, this is only possible with a cut on the vertex position in order to suppress events from the foils. Such a cut however is not feasible for this experiment. The vertex resolution is different for each angle and moreover, spectrometer A was not designed for a high vertex resolution.

Instead, the background is estimated by simulation. A fit of the elastic and quasi-elastic background models to data is part of the optimization process described in the next section 7.4. The scaling parameters a_{el} and a_{qel} that estimate the background level are determined with equation (7.8). To get a consistent background subtraction, the scaling parameters are averaged for all data runs measured with the same kinematic setup, i.e. the same scattering angle and the same beam energy. An example for the estimated background can be seen in figure 7.5.

7.4. Fit of the Simulation to Data

The simulation contains parameters to simulate the resolution of the detector. These are the resolution of the momentum, the vertex position and the in-plane and out-of-plane angles Φ_0 and Θ_0. They control the width of the distributions of the simulation and need to be adjusted to match the data. Since the detector resolution depends on the kinematics, the parameters have to be determined for each setup individually. In addition to the parameters of the simulation, the position of the peak in the $\Delta E'$ histogram in simulation and data has to coincide. The peak position depends on the field of the spectrometer magnets. Usually, the magnetic field of the spectrometers is adjusted so that elastically scattered particles hit the center of the focal plane in the dispersive direction, which corresponds to $\Delta E' = 0$. In this experiment, the magnetic fields in spectrometer A were chosen to be 2% higher, which shifts the point of impact of elastically scattered electrons to the lower half of the focal plane, as well as the peak position in the $\Delta E'$ histogram to negative values. This was done to detect most electrons in a region of the Čerenkov detector where the efficiency was expected to be the highest.

To find the optimal parameters, a least-squares optimization is performed using SciPy's minimize function with the Nelder-Mead method. At each iteration the simulation is run, the relevant histograms of data and simulation are compared and a combined χ^2 is calculated. The scaling parameters a_h, a_{el}, a_{qel} for the simulation models are determined by minimizing

$$\chi^2(a_h, a_{el}, a_{qel}) = \sum_i \left(\frac{N_i - (a_h h_i + a_{el} e_i + a_{qel} q_i)}{\Delta N_i} \right)^2 \tag{7.8}$$

with the measured events N_i and the simulated events h_i, e_i and q_i for hydrogen, elastic and quasi-elastic background in the i-th bin. As mentioned in section 5.4, the background models for elastic and quasi-elastic scattering off the target cell only reproduce the correct shape. The size of the scaling parameters a_{el} and a_{qel} for the background models is therefore mostly arbitrary. The hydrogen simulation on the other hand produces a real cross section. Here, the scaling parameter a_h models unknown effects in the data, like the difference in the assumed form factors to the real form factors, uncertainties in the determination of the luminosity and unknown radiative corrections.

The process to match data and simulation is done in two steps. First, the target offset and the vertex resolution are optimized. The vertex resolution can be found easiest by comparing the background simulation and the data from the empty cell measurements. In this step, only the two background models have to be updated after each iteration. The histogram of the z-coordinate of the vertex has two distinct peaks where the beam enters and exits the cylindrical target cell. The $\Delta E'$ histogram is also included in the optimization process to ensure the correct ratio of the elastic and quasi-elastic background models. An example of an optimized setup is shown in figure 7.4. For the kinematic settings where no empty cell data was measured, the values for the vertex resolution are determined via interpolation of the values from the optimized settings. In the second step the momentum, the angular resolution and the momentum resolution, as well as the scaling parameters for the background and hydrogen simulation are all optimized at the same time. The histograms of $\Delta E'$, Δp and the angles Φ_0 and Θ_0 are compared. This time also the data analysis has to be updated after each iteration since the momentum value shifts the data histograms. Figure 7.5 shows the matched simulation to a hydrogen measurement with the same setting as the empty cell measurement in the previous figure.

Because the scaling parameters for the simulation were also determined in the last step, one can now directly subtract the background from the data.

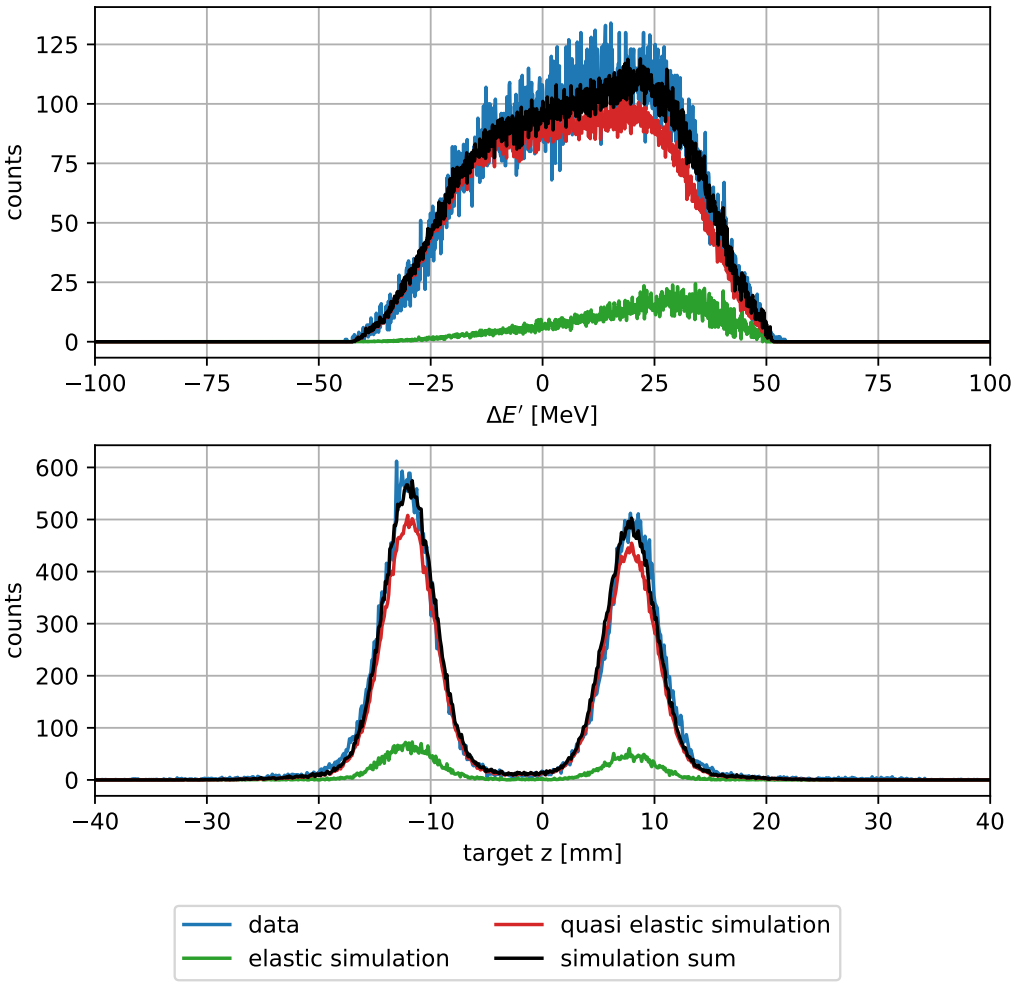

Figure 7.4.: Data and simulation for an empty cell measurement at an angle of 87° and 855 MeV beam energy. The empty target cell was mounted on the target ladder (figure 3.8) slightly shifted towards the direction of the beam, which is why the peaks in the lower plot are not symmetric around zero.

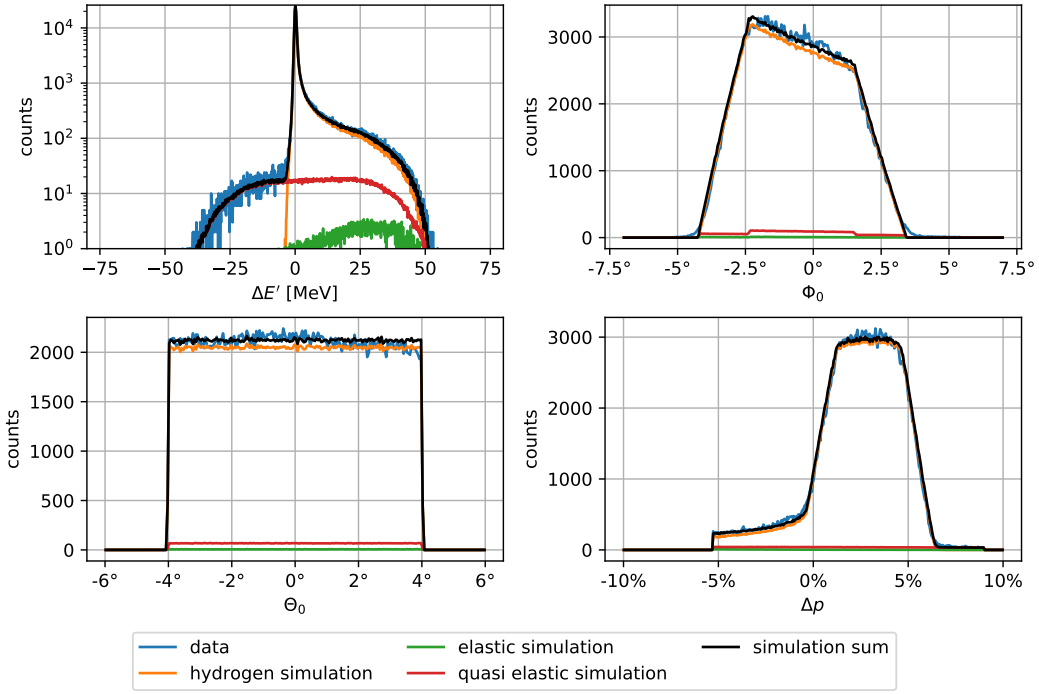

Figure 7.5.: Optimized simulation and background estimate for a measurement at an angle of 87° and 855 MeV beam energy.

7.5. Luminosity

In a fixed target experiment the luminosity is defined as the product of the number of incident particles per time and the target particles per unit area. To calculate the cross section, the integrated luminosity

$$L_{\text{int}} = \int L \, dt = n_t \, N_e \tag{7.9}$$

has to be determined, where n_t is the number of particles per unit area and N_e denotes the total number of beam electrons. By integrating the beam current of the accelerator I over the duration of a measurement, one obtains:

$$N_e = \frac{1}{e} \int I \, dt = \frac{Q}{e} \, . \tag{7.10}$$

The variable n_t is given by the properties of the target:

$$n_t = \rho \, d \, \frac{N_A}{M_H} \tag{7.11}$$

with the density of the liquid hydrogen ρ, the target length d, the molar mass of hydrogen M_H and Avogadro's constant N_A. Thus, the integrated luminosity

becomes

$$L_{\text{int}} = \rho\, d\, \frac{N_A\, Q}{M_H\, e}\,. \tag{7.12}$$

During the experiment the liquid hydrogen is cooled down to around 22 K at a pressure of 2 bar. Temperature and pressure are continuously monitored and an average target density is calculated for each measurement. Under these conditions it is difficult to determine the absolute target length with a precision of better than one percent. These uncertainties contribute to the global normalization as a constant factor, which will be determined by a normalization parameter in the fit.

The beam current in this experiment is measured by a Förster probe, also called flux gate magnetometer. The probe measures the induced magnetic field of the electron beam, which is then converted to a current signal. This current is used as a feedback to drive a compensation coil. The current that cancels out the induced field is the measured current of the electron beam. The Förster probe is installed at a position in the RTM3 where all recirculations pass trough. In this way, each recirculation contributes to the induced signal, improving the precision of the current measurement. For N recirculations, the uncertainty can be estimated to be $50/N$ nA. A larger uncertainty is caused by a drift of the probe for long measurement periods. Without a periodic zero-point adjustment that can only be done when the beam is turned off, the probe drifts over time [76]. Since the magnitude of this drift is difficult to quantify, the statistical errors are examined in section 7.6 for such effects. Finally, the luminosity has to be corrected for the dead time of the detector and the data acquisition to get the effective measurement time. This is done by the program *luminosity++*, which also calculates the charge by integrating the values of the Förster probe.

7.6. Statistical Errors

As described in section 7.1 the data is grouped in sets and the luminosity is used for a relative point-to-point normalization for the data within the same set. For the data taken in this experiment, each normalization group is essentially constituted by all cross sections measured at the same beam energy. The relative point-to-point error in each group is not only given by the error from counting statistics, but also by a number of other factors, such as the statistical uncertainty of the background estimation or undetected effects connected to the accelerator performance like fluctuations in the measurement of the beam current. The size of the contributions to the point-to-point errors beyond pure counting statistics was tested by a polynomial fit for each beam energy. Figure 7.6 shows the measured cross sections relative to the cross section calculated with the standard dipole form factor and the fit curves.

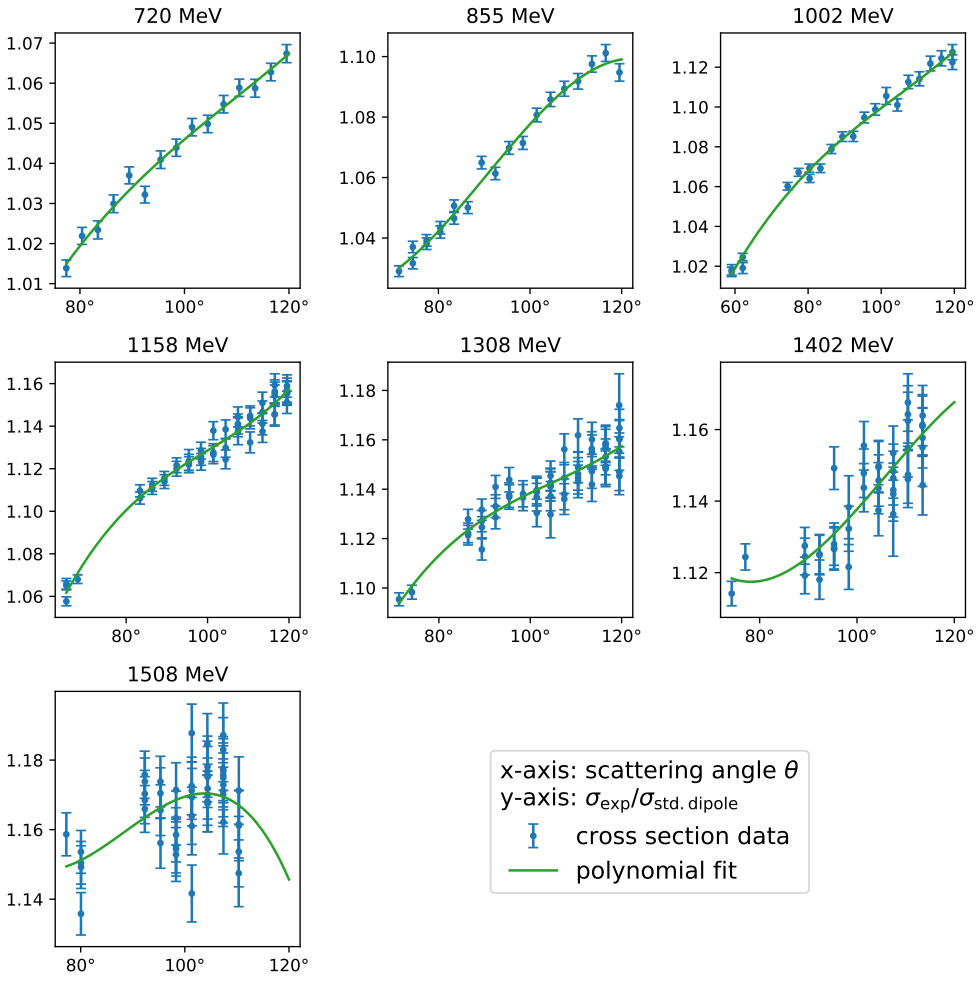

Figure 7.6.: Polynomial fit of the cross section data for each energy.

The results for the χ^2 of the residuals and the underlying distributions are given in figure 7.7. As can be seen, the χ^2-values are close to or greater than the mean value for all beam energies in which two are just outside of the 95% confidence interval. The overall tendency to the right tail of the distributions indicates that the size of the statistical errors is slightly underestimated. The error bars at each beam energy are therefore scaled by the square root of the respective reduced χ^2. In this way each normalization group is given the same statistical weight in the fit. The scaling factors for the statistical errors are listed in table 7.1. It was tested that this correction of the errors changes the normalization by the fit in section 9.2 by a maximum of 0.27%.

Table 7.1.: The statistical error bars at each beam energy are scaled by the square root of the reduced χ^2. This leads to a more accurate estimate of the statistical error than if only the error from pure counting statistics is taken into account.

Beam Energy [MeV]	DOF	χ^2_{red}	$\sqrt{\chi^2_{\text{red}}}$
720	11	1.124	1.060
855	17	1.680	1.296
1002	18	1.888	1.374
1158	43	1.036	1.018
1308	54	1.002	1.001
1402	37	1.301	1.141
1508	46	1.537	1.240
1402	37	1.301	1.141
1508	46	1.537	1.240

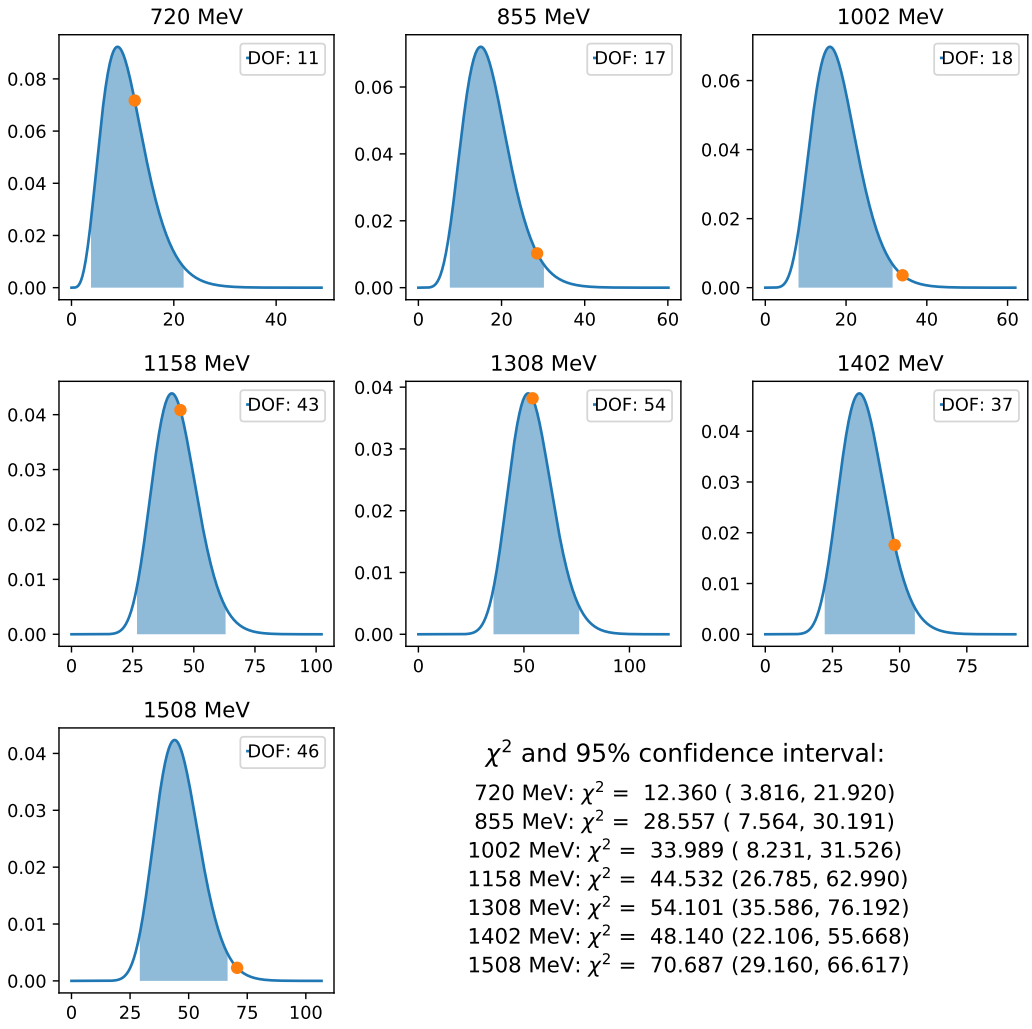

Figure 7.7.: χ^2-values and corresponding χ^2-distributions for the polynomial fits of the data in figure 7.6. The blue shaded area marks the 95% confidence interval.

7.7. Inclusion of External Data

Due to the discontinuity in the quadrupole field in spectrometer A, which was described in section 4.1, there is an area in the detectable momentum range of spectrometer A where the calibration of the optics is not good enough for a precise cross section measurement. Up to four settings at each beam energy had to be excluded from the final analysis, see figure 4.1. Because of the excluded settings the original plan for the analysis of the data could not be followed. It was to be expected that the decreasing kinematic overlap of the measured settings at higher Q^2 leads to a less reliable separation of the form factors, but the excluded settings exacerbate the situation. The fit to the MAMI data in chapter 8 will show that there is not enough kinematic overlap anymore between the data subsets at the higher beam energies to constrain the fit. Similar to the classical Rosenbluth separation, the fit method relies on a sufficient redundancy of data points at different values of ε with roughly the same Q^2. Only then the Rosenbluth formula represents a strong constraint on the individual normalization sets into which the data are grouped. To remedy this deficit in the measured data, the fit will be rerun in chapter 9 with the previous world data included as well. The additional data provides more stability for the fit in the range $Q^2 > 1\,(\mathrm{GeV/c})^2$.

Chapter 8 presents the fitting procedure and the results from the fit to the MAMI data alone. It also describes how the statistic and systematic confidence bands of the form factors are calculated. The same techniques will be used to obtain the statistic confidence bands in the fit to the world data in chapter 9. Since the form factor results from the world data fit are expected to be more accurate, the discussion of the influence of the TPE correction on the form factor ratio will be in chapter 9 as well. The results from the MAMI data alone nevertheless show the precision with which the form factors can be extracted.

8. Fit of the Cross Section Data

8.1. Fit Method

With the method presented in the previous chapter, 254 cross section points were analyzed in this thesis. The form factors are now determined by a direct fit of the cross section data with a given form factor model. The fit will also fix the absolute normalization of the data. As mentioned before, the normalization via the luminosity has an uncertainty of a few percent. The normalization must therefore be determined from the data themselves using the known values of the form factors at $Q^2 = 0$. This however requires cross section data at sufficiently low values of Q^2. Thus, the data from this work is combined with the data from the previous experiment at MAMI and A1 from 2010, where 1422 elastic electron-proton cross sections have been measured down to a Q^2 of $0.004\,(\mathrm{GeV/c})^2$ [18]. The two measurements have overlapping setups in the Q^2 range from 0.5 to $1\,(\mathrm{GeV/c})^2$.

The new data measured in this work, as well as the existing data, are grouped in sets with a relative normalization via the luminosity. Each group of data is assigned a unique combination of up to two normalization constants as free parameters in the fit. These scaling parameters model the difference in the normalization for each set of data points. The scaling parameters can easily be determined by the fit, because the data subsets are constrained by kinematic overlaps of the different subsets. Eight normalization constants are introduced for the data presented in this work, one for each of the seven beam energies and one additional constant is added to account for a possible difference between the two transfer matrices (see appendix A). The 2010 data was measured with all three spectrometers and was analyzed with the same method as described here. 31 normalization constants were used to fit the data, most of which model the difference in the normalization between the spectrometers at each beam energy. For more detailed information on the old data see [18]. The normalization of the previous data will be fit anew, resulting in a global fit of a total of 1676 cross sections with 39 normalization constants as free parameters in addition to the parameters of the form factor model.

The global fit minimizes the quadratic sum

$$M^2 = \sum_i \left(\frac{r_i - \Pi_i \, m_i}{\Delta r_i} \right)^2 \tag{8.1}$$

where Π_i is the product of the normalization constants for the subset the measured cross section ratio r_i belongs to. All cross section ratios, as well as the cross sections calculated with the form factors from the fit model m_i are extracted relative to the cross section for the standard dipole:

$$r_i = \frac{\left(\frac{d\sigma}{d\Omega_i}\right)}{\left(\frac{d\sigma}{d\Omega_i}\right)_{\text{std.dipole}}}, \quad m_i = \frac{\left(\frac{d\sigma}{d\Omega_i}\right)_{\text{model}}}{\left(\frac{d\sigma}{d\Omega_i}\right)_{\text{std.dipole}}} \tag{8.2}$$

It should be noted that the sum M^2 in equation (8.1) can not be proven to follow a true χ^2-distribution. The true theory curve is unknown and thus, it can not be verified if the residuals are following a Gaussian shape with a variance that matches the estimated errors Δr_i. The minimum $M^2_{\text{min}} \approx \chi^2$ can nevertheless serve as an indicator for the quality of the fit.

8.2. Form Factor Model

The true functional form of the form factor is unknown to this day. Early measurements in the 1950s [12–14] showed that the electric and the magnetic form factor approximately follow a dipole shape. The standard dipole

$$G_{\text{std.dipole}}(Q^2) = \left(1 + \frac{Q^2}{0.71\ (\text{GeV/c})^2}\right)^{-2} \tag{8.3}$$

was used for the electric form factor and, scaled with μ_p, also for the magnetic form factor for a long time. By this time it is known that this simple model is unable to describe the current data. However, the standard dipole still serves as a rough approximation, especially at low Q^2. It is also frequently used to divide out the general trend in the cross section data to better visualize any discrepancies.

A number of different models for the form factors come into consideration such as polynomials, splines, dipole models and also more elaborate models based on theoretical approaches. A representative selection of models was compared extensively in [20] and thus, will no be repeated here. While the choice of a particular model is subjective at first, the selected model might introduce a bias. In [20] the bias was studied with Monte Carlo data sets generated with form factors from previous publications. The reliability in reproducing the initial form factors was then tested for different models. Two cubic spline models proved to be best suited to reproduce a given parameterization of the form factors with a small bias and high precision. The first model

$$G^{E,M}_{\text{spline}}(Q^2) = G^{E,M}(Q^2 = 0)\ \left(1 + Q^2 S^{E,M}(Q^2)\right) \tag{8.4}$$

is essentially a single cubic spline function $S(Q^2)$. In the second model

$$G^{E,M}_{\text{spline}\times\text{dipole}}(Q^2) = G^{E,M}(Q^2=0)\, G_{\text{std.dipole}}(Q^2)\, \left(1 + Q^2 S^{E,M}(Q^2)\right) \tag{8.5}$$

the previous ansatz is multiplied by the standard dipole. Both models are normalized to $G^E(Q^2=0)=1$ for the electric form factor and normalized to $G^M(Q^2=0)=\mu_p$ in the case of the magnetic form factor. The additional dipole term in equation (8.5) has several advantages for the fit of the cross sections. The dipole reflects the rough trend of the form factors and the spline is only used to describe the relative difference. This provides more stability for the data at higher Q^2 where the kinematic overlaps of the normalization groups are getting smaller. The model is also less sensitive to the choice of the knot locations that are needed for the definition of the spline function, see section 8.2.1. Moreover, it was found in [20] that models with an included dipole term can achieve a comparable fit result with fewer parameters. Therefore, the fit of the cross section data will be performed with the spline × dipole model from equation (8.5). The next section describes how the spline function $S(Q^2)$ can be constructed with B-splines.

8.2.1. B-splines

A spline of degree n is composed of piecewise polynomials of the same or lower degree and is $(n-1)$-times continuously differentiable. It is defined over a sequence of ordered x-values, called knots $t_i \leq t_{i+1}$ that divide its domain in intervals. One way of constructing a spline is via basis splines or B-splines [77]. In this representation, a spline function

$$S(x) = \sum_i^N a_i B_{i,k}(x) \tag{8.6}$$

is the sum of B-splines $B_{i,k}(x)$ of order k, which are piecewise polynomials of degree $n = k-1$. The number N of coefficients a_i,

$$N = m - n - 1\,, \tag{8.7}$$

is given by the degree of the spline n and the number of knots m. B-Splines are well suited for least squares problems since they represent a linear model by construction. Additionally, the coefficients a_i only affect a part of the spline and can thus be easily determined in a fit, even for a large number of parameters. B-splines can be defined recursively by means of the Cox-de Boor recursion formula [77]. The lowest order B-splines

$$B_{i,1}(x) = \begin{cases} 1 & t_i \leq x < t_{i+1} \\ 0 & \text{otherwise} \end{cases}, \tag{8.8}$$

are a constant value of 1 over each interval. The higher order B-splines can be calculated by the recursion formula

$$B_{i,k}(x) = \frac{x - t_i}{t_{i+k-1} - t_i} B_{i,k-1}(x) + \frac{t_{i+k} - x}{t_{i+k} - t_{i+1}} B_{i+1,k-1}(x) \tag{8.9}$$

as linear combinations of B-splines of the order $k-1$. A single B-spline of the order k only spans over the interval $[t_i, t_{i+k})$ and is zero otherwise. On the basis of the definition in equations (8.8) and (8.9) the B-splines are normalized

$$\sum_i B_{i,k}(x) = 1 \tag{8.10}$$

for all x in the domain of the spline function.

In order to obtain an accurate spline fit of given data, the locations of the knots have to be chosen appropriately. The knots are best placed at prominent points that reflect the general trend of the data, like extremes, inflection points or in areas where the slope changes rapidly. If the density of the data points varies considerably the spacing of the knots should be adjusted accordingly. As an example, figure 8.1 shows generated data that was fitted with cubic B-splines. It illustrates a suitable placement of the knots in this particular case. In order to restrict all B-splines to the chosen interval, the first knot and the last knot have to be added three more times each in the case of a cubic spline.

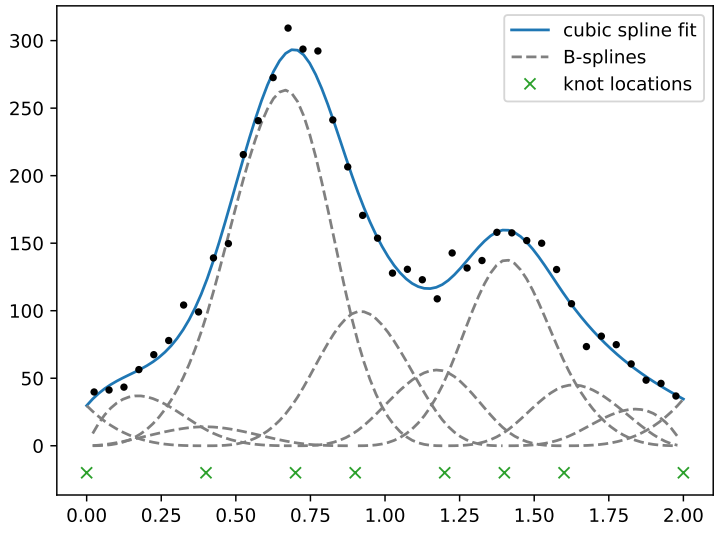

Figure 8.1.: Example of a fit of generated data using B-splines. The blue curve is a fitted cubic spline that is composed by a sum of B-splines (dashed gray). The locations of the knots are indicated by green crosses.

8.2.2. Model Optimization

To find the optimal knot positions for the spline model, the data was fitted with randomized knots. Starting from a uniform knot spacing between 0 and 2 $(\mathrm{GeV/c})^2$, the locations of the inner knots were varied between half the distance to the previous and to the next knot. The number of knots was also varied between five and eight. 50 000 fits were performed for each number of knots. The fits with five knots did not provide models with enough flexibility to fit the data and produced large χ^2. The fits with seven and eight knots did not improve the average achieved χ^2 significantly over the fits with six knots and also showed visible oscillations in some cases, which is a sign of overfitting. Not only the best χ^2, but also the total curvature of the resulting form factors was considered in selecting the optimal knots for the model. The total curvature in the interval $[a, b]$ of a function $f(x)$ is defined by [72]

$$\int_a^b \left[f''(x)\right]^2 dx\,. \tag{8.11}$$

A comparatively high or low curvature was also an exclusion criterion in the selection of the optimal model. The optimal knot locations that produced a good χ^2 without having excessively high or low curvature were determined to be the six knots at the positions:

$$0,\ 0.3,\ 0.65,\ 1.0,\ 1.4,\ 2.0 \quad (\mathrm{GeV/c})^2 \tag{8.12}$$

The same knot locations are used in the spline $\times$ dipole model in equation (8.5) for both form factors.

8.3. Fit Results

The results for the cross sections with the new normalization from the fit are presented in figures 8.2 to 8.6. The cross sections shown are divided by the cross section calculated with the standard dipole form factors to better visualize the statistical error bars. The data includes all radiative corrections described in section 2.2, but not the Feshbach Coulomb correction and no TPE correction. An overview of the complete MAMI data set as a function of Q^2 can be seen in figure 8.2. Figures 8.3 to 8.6 show the fitted data for each beam energy as a function of the scattering angle. The fit achieved a minimum value of

$$\chi^2_{\mathrm{min}} = 1989.9 \tag{8.13}$$

with 1676 data points and 55 fit parameters (39 normalization parameters and 16 parameters for the form factors). The new fit leaves the normalization of the previous MAMI data largely unchanged. At the beam energies where only measurements from

2010 exist, the normalization parameters scatter around 1 with a standard deviation below 0.1%. It has to be taken into account that the normalization parameters determined by the fit depend to some extent on the fit model. Tests with different models in [20] have shown that fits which achieve good χ^2 produce a comparable normalization as well. An average standard deviation of 0.073% was found for the normalization parameters from different models, which is in good agreement with the deviation observed here.

The normalization of the new data by building on the normalization of the previous MAMI data only worked to a limited extent. Figure 8.2 shows the discrepancy between the unnormalized data in gray and the new data with the normalization by the fit in orange. Up to the beam energy of 1002 MeV, the normalization of each data subset only changes by about 1% or less. This is well within the range of the expected uncertainty of the luminosity. However, the change of the normalization increases strongly for the data at the beam energies above. The fit modified the normalization of the data subset at 1508 MeV by more than 10%. A shift of this magnitude is much larger than expected and can not be explained by errors in the measurement or in the calculation of the cross section. Past measurements at A1, including the first part of this experiment in 2010, have shown that cross sections can be measured with an accuracy of one to two percent with the A1 setup. This drastic change in the normalization is much more a direct consequence of the missing setups which had to be excluded from the analysis. As it was already mentioned in section 7.7, there is not enough kinematic overlap in Q^2 anymore between the data subsets at the higher beam energies to constrain the fit. To remedy this deficit in the measured data, the fit will be rerun in chapter 9 with the previous world data included as well. The additional data provides more stability for the fit in the range $Q^2 > 1.2\,(\mathrm{GeV/c})^2$.

The next section presents the from factor results from the fit in figure 8.2 and describes how the statistic and systematic confidence bands of the form factors are calculated. The same techniques will be used to obtain the statistic confidence bands in the fit of the world data in chapter 9.

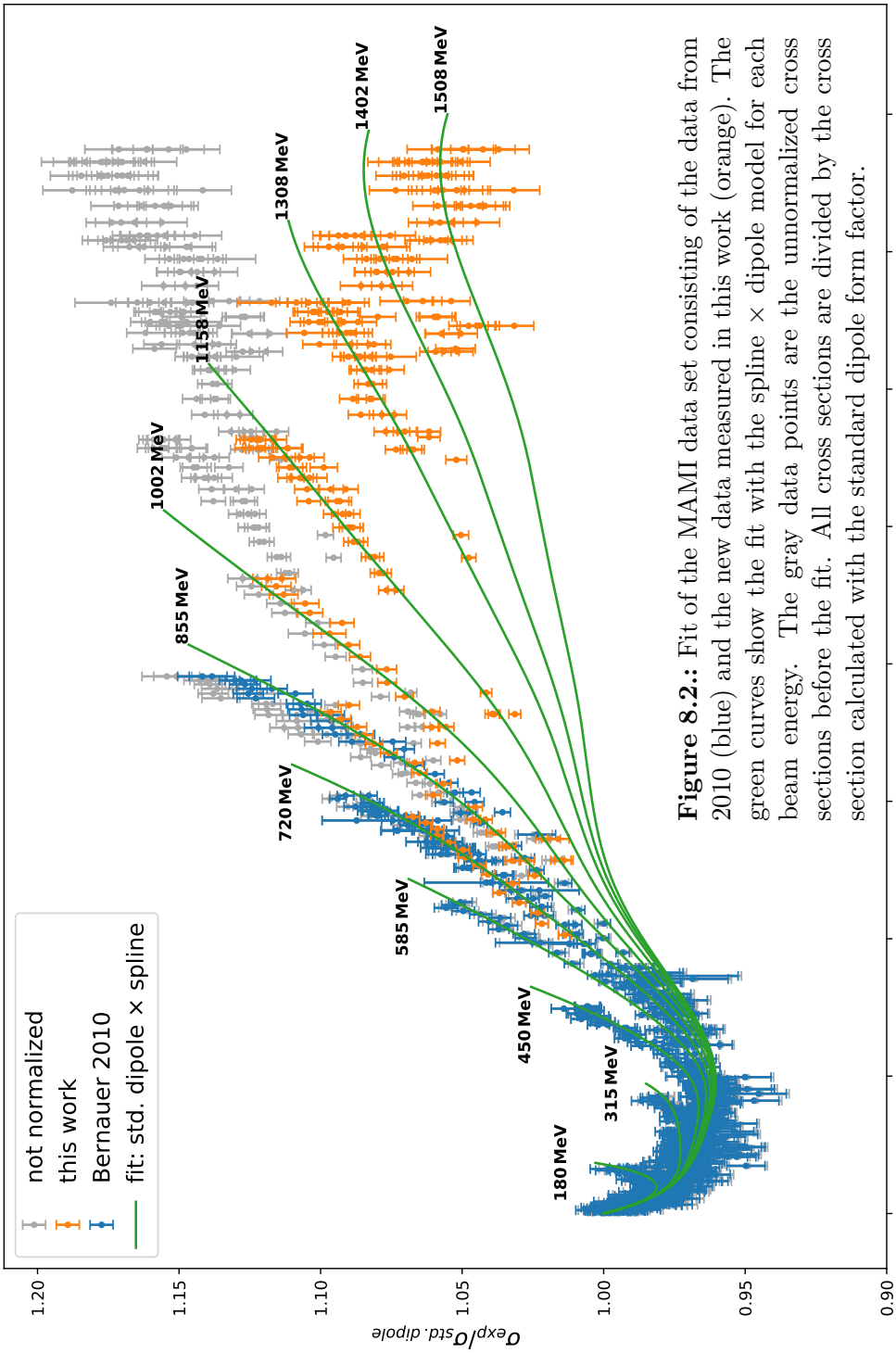

Figure 8.2.: Fit of the MAMI data set consisting of the data from 2010 (blue) and the new data measured in this work (orange). The green curves show the fit with the spline × dipole model for each beam energy. The gray data points are the unnormalized cross sections before the fit. All cross sections are divided by the cross section calculated with the standard dipole form factor.

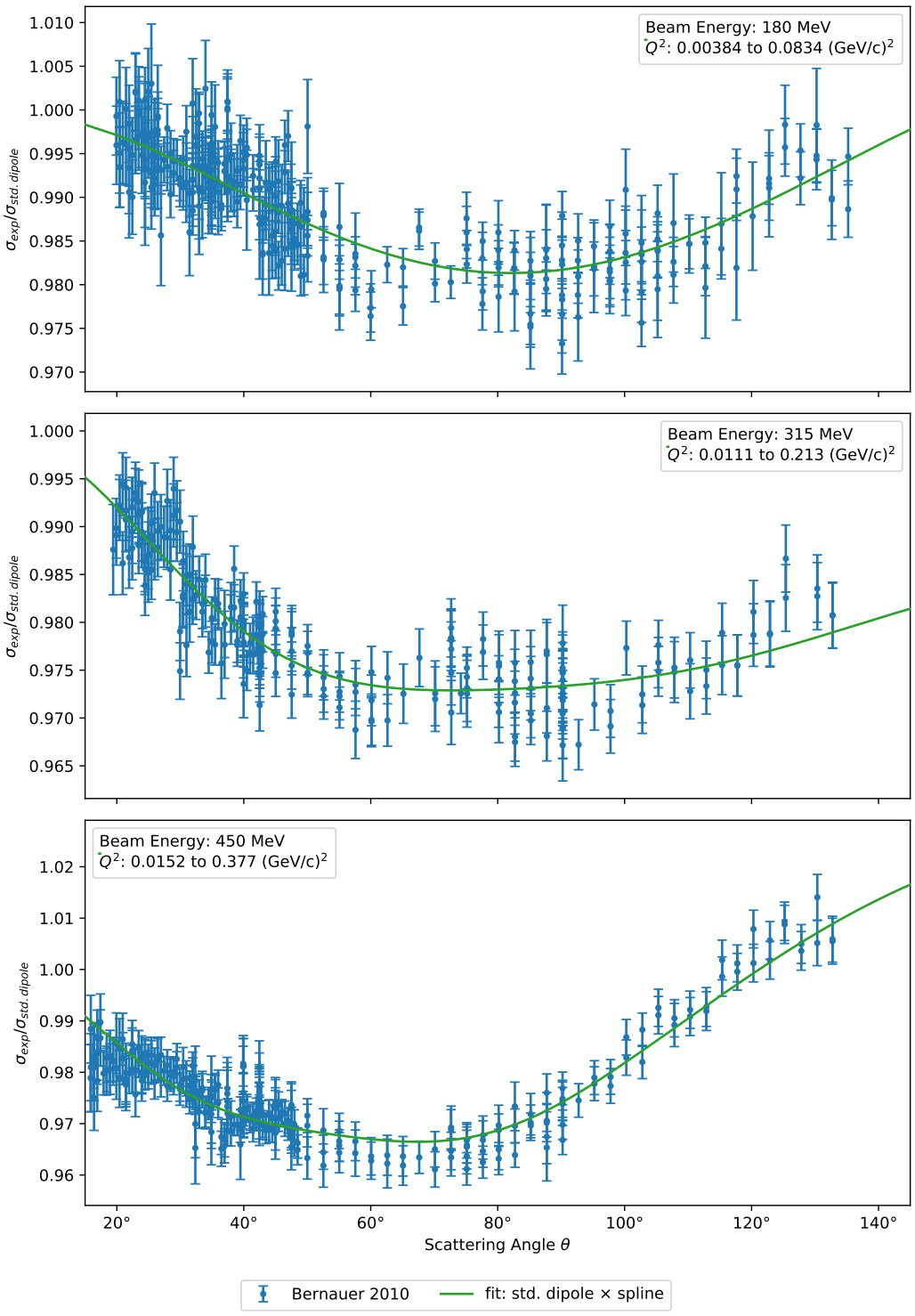

Figure 8.3.: Cross sections and fit of the data at 180 MeV (top), 315 MeV (center) and 450 MeV (bottom) as function of the scattering angle. The minimum and maximum Q^2 value of the data at each beam energy is given in the legend.

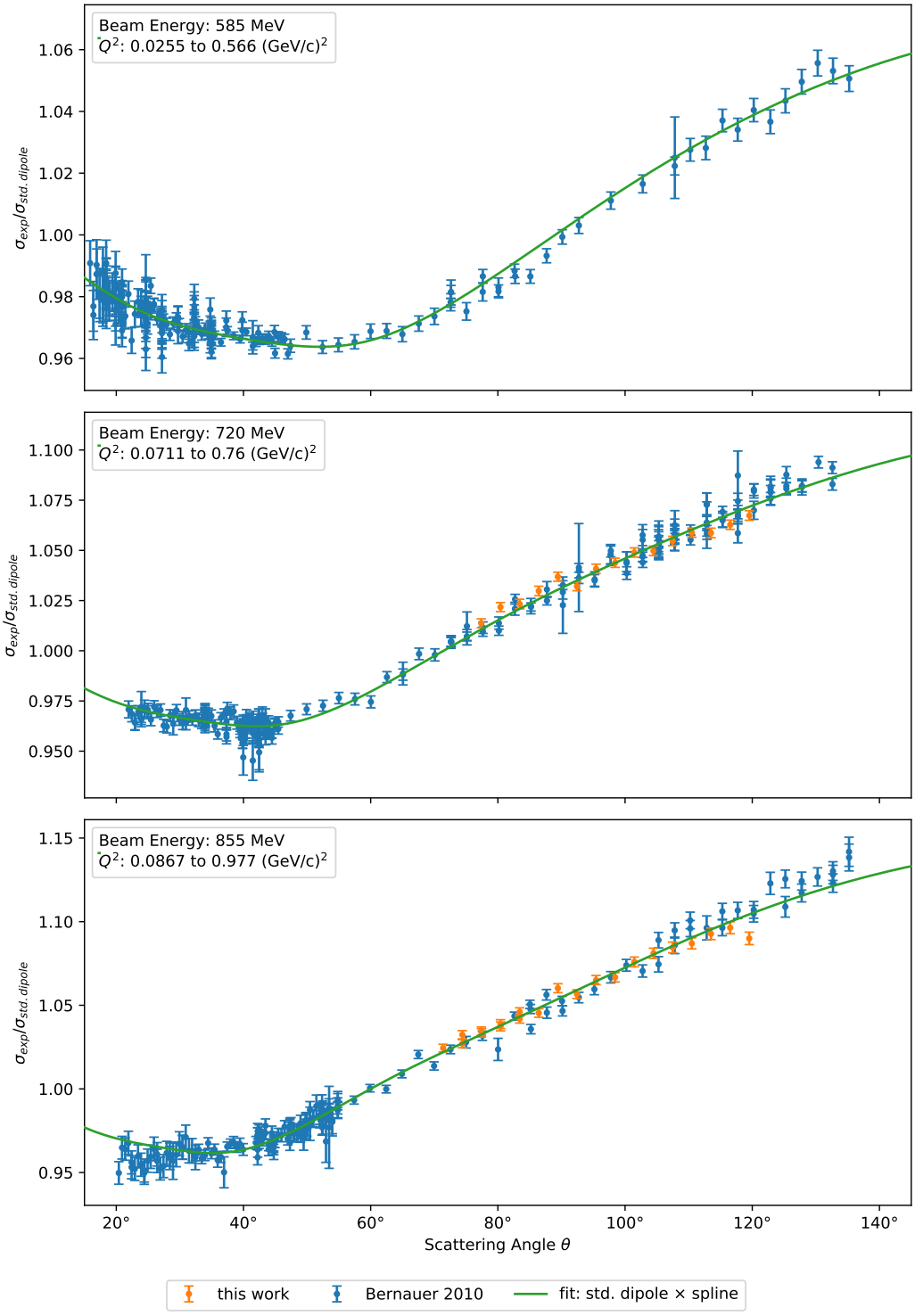

Figure 8.4.: Same as figure 8.3, but for the beam energies 585 MeV (top), 720 MeV (center) and 855 MeV (bottom). The two data sets overlap at the beam energies of 720 MeV and 855 MeV.

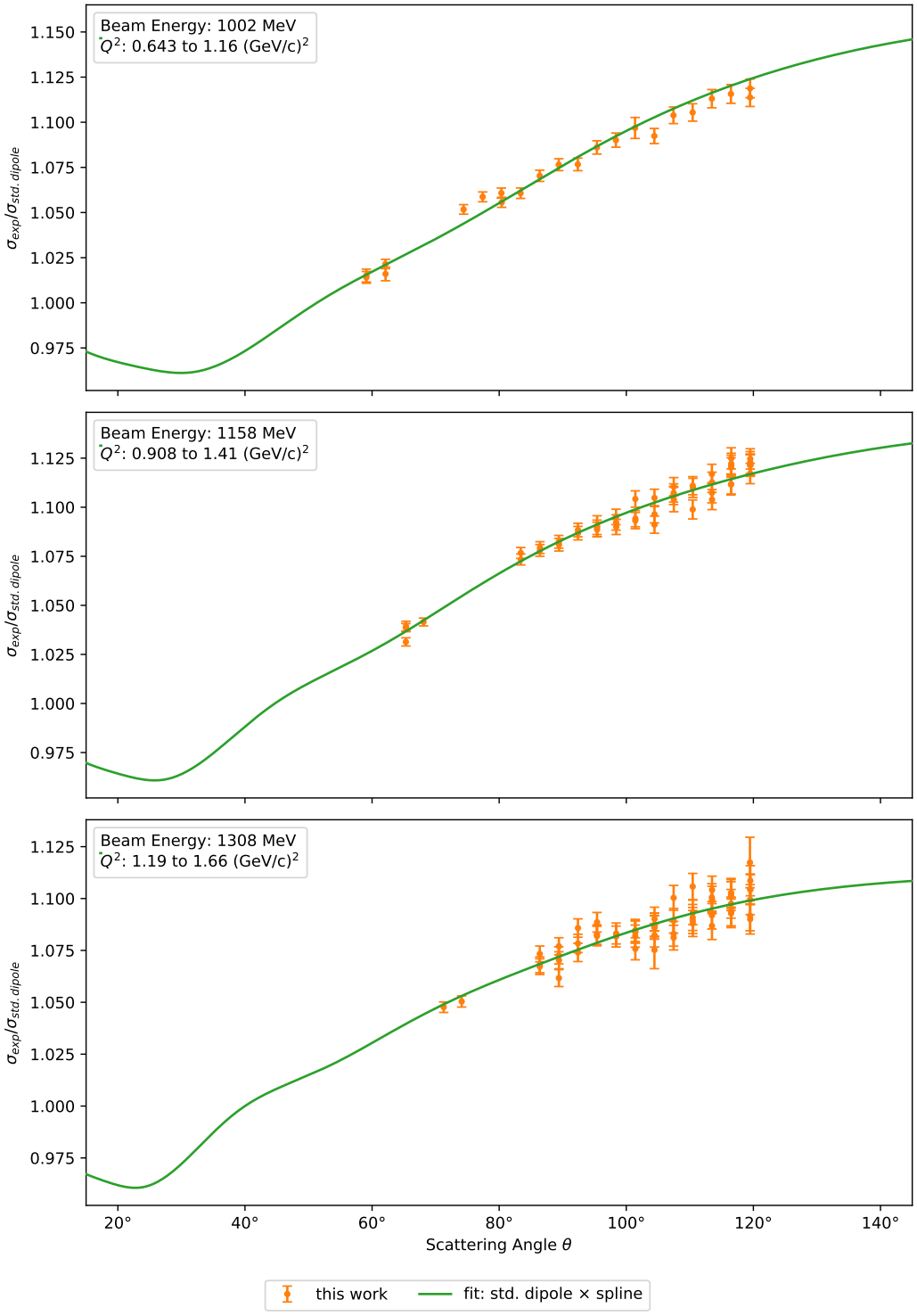

Figure 8.5.: Same as figure 8.3, but for the beam energies 1002 MeV (top), 1158 MeV (center) and 1308 MeV (bottom).

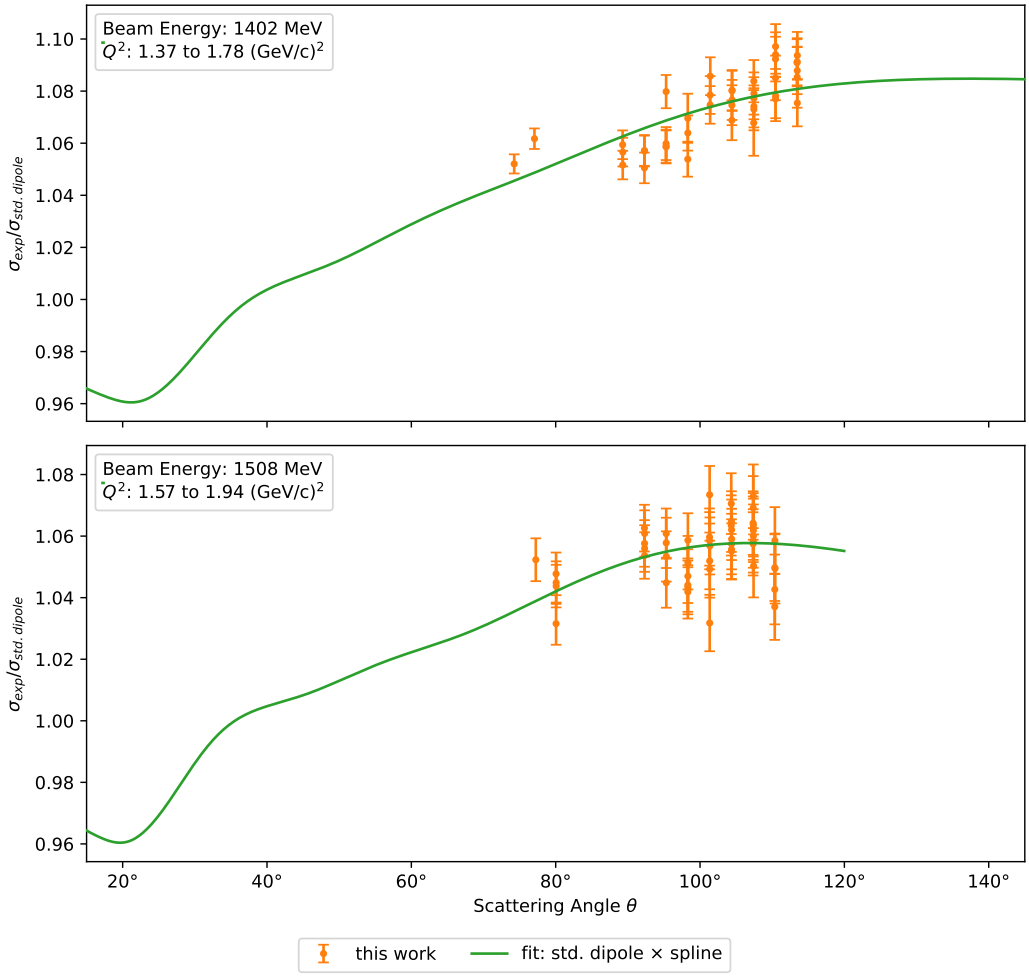

Figure 8.6.: Same as figure 8.3, but for the beam energies 1402 MeV (top) and 1508 MeV (bottom).

8.4. Form Factor Results

8.4.1. Statistical Confidence Bands

The error on the extracted form factors is expressed as a confidence band. The statistical confidence band originates from the statistical errors of the cross section data. Standard error propagation with the covariance matrix gives the well known 1-σ error, a symmetrical error band around the fit with a confidence level of 68.3%. This method is exact for a linear model. The cross section data, however, do not depend linearly on the parameters of a form factor model, since the form factors enter the Rosenbluth formula quadratically. The covariance matrix is only an approximation in this case. Furthermore, an uncertainty in the normalization determined by the fit can not be accounted for, either.

The statistical confidence bands were therefore determined by a Monte Carlo technique which is often called the bootstrap method. Pseudo data sets were generated where each data point was varied according to a Gaussian distribution with a standard deviation of the individual statistical error. The normalization of each normalization group was additionally varied by 5% to test if a global shift is absorbed in the fit. If the fitting procedure is correctly, the influence of such a shift on the final result will be negligible. 50 000 data sets were generated this way and fitted with the same model like in the original fit. One can then construct pointwise confidence bands by calculating the interval that comprises 68.3% of the fits at each Q^2. The bootstrap method fully covers all nonlinear effects and gives a better estimate of the confidence bands. It is evident that the resulting confidence band is model dependent. The form factors with the statistical confidence bands are shown in figure 8.7.

8.4.2. Systematic Errors and Confidence Bands

Systematic errors that cause a global shift of the data are absorbed in the floating normalization and have little to no influence on the result of the fit. Besides that, an uncertainty of the normalization of 5% is already included in the statistical confidence bands described above. Only systematic effects that change the slope of the data have not been considered up to now. Theses are drifts over time during the data taking or drifts over the scattering angle caused by the applied cuts in the analysis. While some of these systematic effects can be tested, others have to be estimated. The following points were identified as sources of experimental systematic errors for the cross section:

Drift of the Normalization: A change in the event rate could be caused by unaccounted dead time effects in the detectors or in the readout electronics. This

error was estimated to be below 0.05%, based on long-term experience in operating the detector setup.

Change of Efficiency over the Focal Plane: The detection efficiency depends on the position where a particle is detected in the focal plane. All three focal plane detectors, the VDC, the scintillators and the Čerenkov detector have a slightly different efficiency depending on the position and the angle of the particle trajectory. Since the central momentum was adjusted for each setup, the elastic events were mostly detected in the same spot in the focal plane. The error on the cross section was estimated to be equal to or less than 0.05%.

Acceptance Cut: The error of the acceptance cut can be tested by varying the cut position. For the settings at the lowest beam energy of 720 MeV, the largest error due to a change in the cut position is about 0.09%. It increases up to 0.34% for the settings at the highest beam energy of 1508 MeV.

Cut in Δp: Like in the previous case, the error introduced by this cut can be tested by varying the cut position as well. The cut in Δp discards far fewer events than the acceptance cut and thus has a lower influence on the cross section. The error was determined to be between 0.01% at 720 MeV and 0.07% at 1508 MeV.

Background Estimation: In section 7.4 the background level was determined for each data run by a fit of the simulation to the data. For the kinematic setups at which multiple data runs where measured, the fitted backgrounds were averaged to get a consistent background subtraction. The systematic error of the optimization procedure was estimated from the standard deviation of the determined background levels for these setups. Again, the error estimate changes with the beam energy from 0.19% at 720 MeV to 0.62% at 1508 MeV.

The listed systematic errors are considered to be independent and are added quadratically. To simulate the effect of a slope, a liner function $f_E(\theta)$ was created for each beam energy. The functions interpolate from zero to the full systematic error at the largest scattering angle of the respective beam energy. The cross sections were then multiplied by these functions and the fit was redone to get the upper bound of the systematic confidence bands of the form factors. Repeating this procedure with the negative slopes of the functions $f_E(\theta)$ gives the lower bound. The systematic confidence bands are added linearly to the statistic confidence bands from section 8.4.1.

8.4.3. Fit Results of the Form Factors

Figure 8.7 shows the form factors from the fit to the data set measured at MAMI. The statistical and systematic error bands give a correct estimation of the precision that can be achieved with a fit to the MAMI data, but do not necessarily indicate the accuracy of the form factor result. The error bands are calculated from the cross section data and are constructed around the optimal fit, and therefore do not reflect the systematic shift in the normalization of the cross section data introduced by the fit (section 8.3). Because of the large shift of the data sets at the higher beam energies, no exact statement about the accuracy of the form factors at $Q^2 > 1.25\,(\mathrm{GeV/c})^2$ can be made at this point. A more accurate result for the form factors is expected from the fit of the world data in section 9.2.

The data measured within this work was laid out to focus on a precise determination of the magnetic form factor. G_M is the dominant contribution to the cross section at the measured kinematics. The contribution of the electric form factor G_E to the cross section decreases at higher Q^2. One can see the decreasing sensitivity to G_E for $Q^2 > 1\,(\mathrm{GeV/c})^2$ from the expanding statistic and systematic error bands. Attention must be paid to the different y-scales for G_E and G_M in figure 8.7. The maximum width of the full error band of G_E is roughly 18 times larger than the one of G_M. The precision of G_E in this Q^2 range can not be improved much further with the experimental setup at A1. One would have to measure at low forward angles where the contribution of G_E to the cross section is highest. Low forward angles at the measured energies are, however, kinematically inaccessible with the A1 setup, because the momentum of the outgoing electron gets too large. For the magnetic form factor, the systematic error dominates up to $Q^2 = 1\,(\mathrm{GeV/c})^2$. In the range above the statistical error increases and becomes the largest source of error. At $Q^2 > 1.5\,(\mathrm{GeV/c})^2$ the fitting procedure is not working properly anymore. Since the magnetic form factor is always forced on a similar downward trend by the fit, the systematic error becomes small.

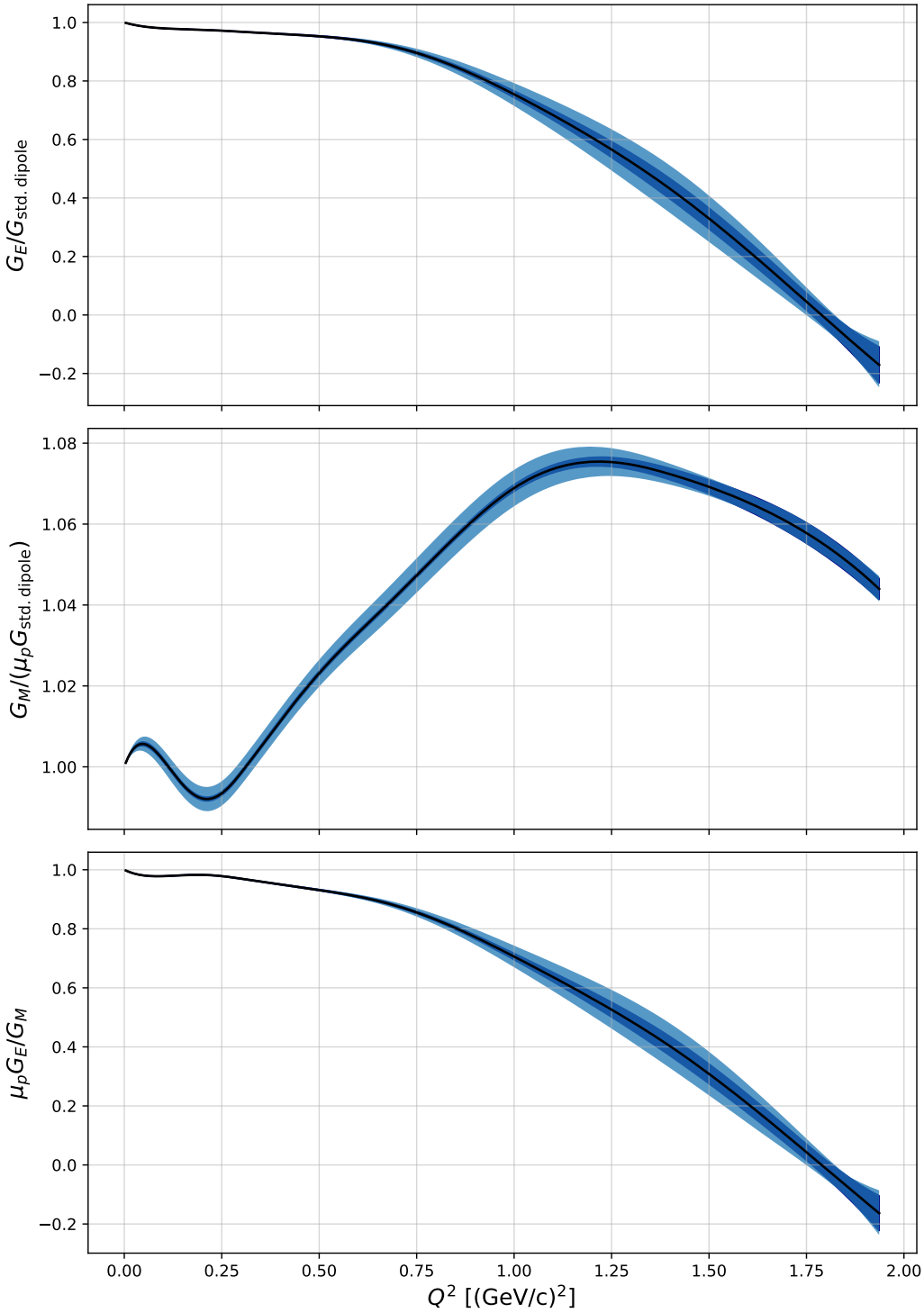

Figure 8.7.: Extracted form factors from the fit of the MAMI data. The upper and the middle plot show the electric and magnetic from factor, respectively, divided by the standard dipole form factor. The lower plot shows the form factor ratio $\mu_p G_E/G_M$. The dark blue area corresponds to the statistical 1-σ confidence band and the light blue area is the experimental systematic error.

9. Fit of the World Data

9.1. External Data

The external cross section data is included in the fit in the same way as in the publication of the previous MAMI data in [20]. As described therein, the radiative corrections of the external data were updated to the prescription of Maximon and Tjon where possible. An overview of the measurements from which the data originate is given in table 9.1. In total, the external data consists of 441 cross sections in the Q^2 range from $0.005\,(\mathrm{GeV/c})^2$ to over $30\,(\mathrm{GeV/c})^2$. The kinematic settings that enter the fit are shown in figure 9.1. One can see that the data measured in this work complements the external data very well. The external data between a Q^2 of $1\,(\mathrm{GeV/c})^2$ and $2\,(\mathrm{GeV/c})^2$ was measured mostly at large ε, whereas the settings of the new data fill the gap at $\varepsilon < 0.5$. This greatly increases the accuracy of the separation of the electric and magnetic form factor by the fit.

Table 9.1.: External cross section data from Rosenbluth measurements included in the fit with the respective Q^2 range and the year of publication.

Year	Q^2 range $[(\mathrm{GeV/c})^2]$	Reference
1966	0.16 - 1.17	Janssens et al. [78]
1970	0.27 - 5.84	Goitein et al. [79]
1970	0.10 - 3.74	Litt et al. [80]
1971	0.27 - 1.75	Price et al. [81]
1974	0.0052 - 0.084	Borkowski et al. [82]
1975	0.012 - 0.18	Borkowski et al. [83]
1975	0.098 - 1.85	Stein et al. [84]
1980	0.0051 - 0.055	Simon et al. [85]
1990	0.49 - 1.75	Bosted et al. [86]
1992	2.50 - 10.0	Rock et al. [87]
1993	2.86 - 31.2	Sill et al. [88]
1994	1.75 - 8.83	Andivahis et al. [89]
1994	0.10 - 3.0	Walker et al. [90]
2004	0.42 - 5.37	Christy et al. [91]
2005	0.50 - 4.10	Qattan et al. [92]

The external data are treated as normalization groups, by introducing one normalization parameter $N_{\mathrm{ext},\,j}$ in the fit for each external data set. The only exception

is reference [89], where two parameters are included, since the data were measured with two different spectrometers. A constraint

$$\left(\frac{1 - N_{\mathrm{ext},\,j}}{\Delta N_{\mathrm{ext},\,j}}\right)^2 \tag{9.1}$$

on each external normalization parameter is also included in the fit, were $\Delta N_{\mathrm{ext},\,j}$ is the normalization uncertainty as quoted in the respective publication. The terms in equation (9.1) are added to the quadratic sum in equation (8.1), which is minimized by the fit. Without any restrictions on the normalization of the external data, the fit would gravitate strongly towards the MAMI data. In the range $Q^2 < 2\,(\mathrm{GeV/c})^2$, 315 cross sections were measured by the experiments in table 9.1 and 1676 cross sections were measured at MAMI. The constraints are therefore introduced to add more weight to the already existing normalization of the external data.

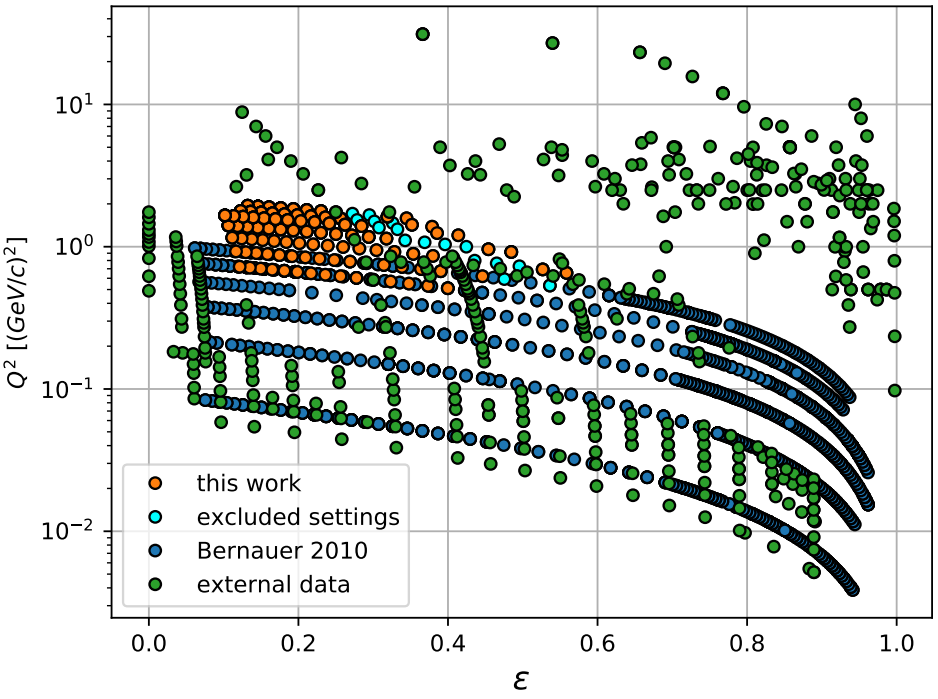

Figure 9.1.: Kinematic settings of the MAMI data (see figure 4.2 for reference) and external data (green).

9.2. World Data Fit

The same spline × dipole model as in chapter 8 is also used here, but with an extended knot vector for the spline to span the entire range of the external data:

$$0,\ 0.3,\ 0.65,\ 1.0,\ 1.4,\ 3.0,\ 5.0,\ 10.0,\ 40.0 \quad (\mathrm{GeV/c})^2 \tag{9.2}$$

The knot spacing is chosen according to the density of the data points. The result of the fit to the world data is shown in figure 9.2 and the optimized values for the parameters of this fit are listed in appendix B. As before, the cross section data includes the radiative corrections from section 2.2, but not the Feshbach Coulomb correction and no TPE correction. It clearly shows that the inclusion of the world data achieved the expected stabilization of the fit. The shift in the normalization of the new data is now consistent for all beam energies. In the range from 720 MeV to 1408 MeV the cross sections are shifted towards smaller values by about 1% or less, and by 1.9% for the cross sections at the highest beam energy of 1508 MeV (table B.2). Based on the precision with which the luminosity can be determined, this shift is well in the expected range and shows that the new data is indeed a seamless continuation of the previous measurement at MAMI, which was one of the main goals of this thesis. The external cross sections, on the other hand, are mostly shifted upward, with 13 out of the 16 external normalization parameters smaller than 1, indicating a discrepancy between the MAMI and the external data. One should however be careful when comparing the data sets at a cross section level. The cross sections at the same Q^2 were measured under completely different conditions, in particular at different scattering angles and beam energies. This results in different values in ε (see figure 9.1), and therefore in a much different sensitivity to the electric and magnetic form factor.

The fit presented here achieved a minimum value of

$$\chi^2_{\mathrm{min}} = 2680.4 \tag{9.3}$$

with 2117 data points and 77 fit parameters. This value is more than 5σ away from the mean of the underlying distribution. The deviation in the normalization between the measurements at MAMI and the previous experiments is one reason why one can not expect to achieve a good fit of the world data. On the theory side, the true functional form of the form factors is unknown and the contribution of the TPE is also not known precisely. The main goal of the fit is to get an estimate by how much the TPE contribution shifts the form factors. Since the TPE model from intermediate state resonances by Ahmed et al. introduced in section 2.3 is only valid up to a Q^2 of $5\,(\mathrm{GeV/c})^2$, the form factors are compared up to this value.

Nearest-neighbor extrapolation is used for data points outside of the domain of the resonance model. Figure 9.3 shows how the form factors change when one of the two TPE models introduced in section 2.3 is applied to the data before the fit. The TPE models cause a decrease of the electric form factor and an increase of the magnetic form factor. As a result, the $\mu_p G_E/G_M$ form factor ratio decreases, which is more in line with the results from polarized measurements. In the next section, the form factor ratio determined in the fit is compared to the data from polarization experiments.

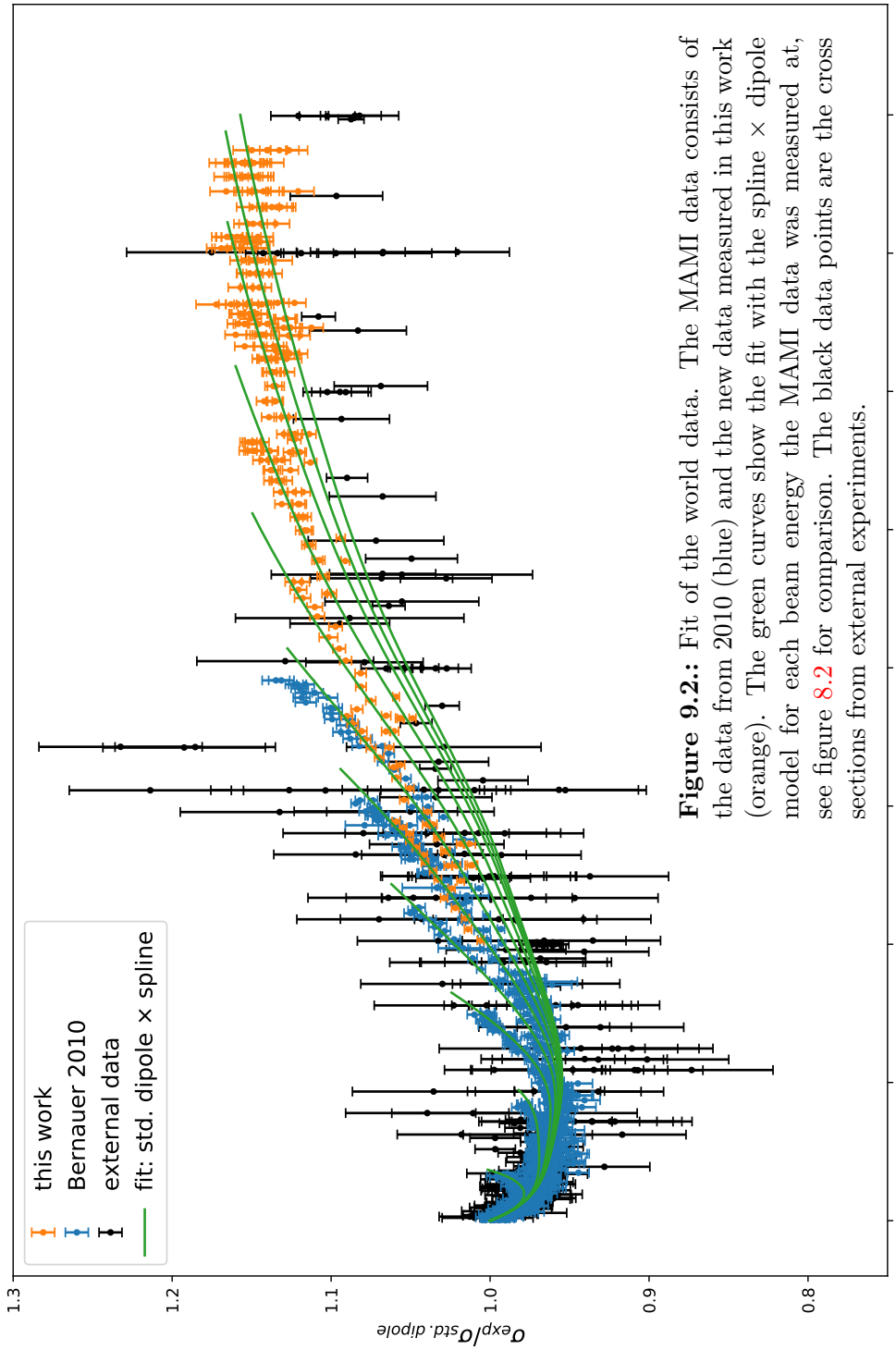

Figure 9.2.: Fit of the world data. The MAMI data consists of the data from 2010 (blue) and the new data measured in this work (orange). The green curves show the fit with the spline × dipole model for each beam energy the MAMI data was measured at, see figure 8.2 for comparison. The black data points are the cross sections from external experiments.

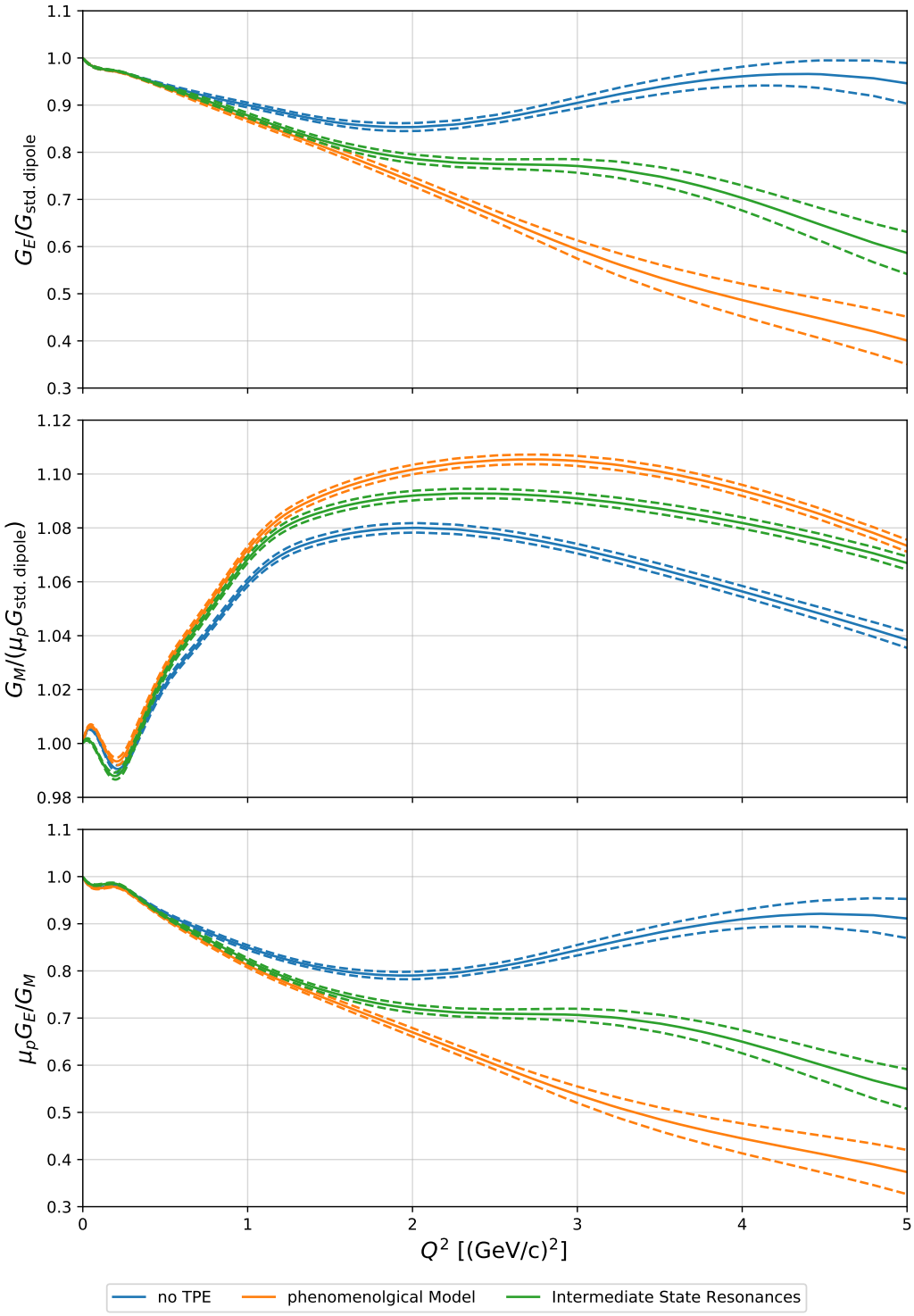

Figure 9.3.: Influence of the TPE correction on the form factors. The blue curves are the result of the fit in figure 9.2 without any TPE correction. A fit with the phenomenological TPE model from [20] applied to the cross sections gives the orange form factors. If the TPE calculation from intermediate state resonances by Ahmed et al. [63] is used instead, the form factors shown in green are obtained. The dashed lines indicate the statistic confidence bands.

9.3. Proton Form Factor Ratio $\mu_p G_E/G_M$

The electromagnetic form factor ratio of the proton has also been measured in many polarization experiments over the years. Most experiments utilize the technique of polarization transfer, in which longitudinally polarized electrons are scattered on unpolarized protons and the transferred polarization to the recoil proton is measured. The polarization components perpendicular (transverse) and parallel (longitudinal) to the proton momentum in the scattering plane are given by [93, 94]

$$I_0 P_T = -2\sqrt{\tau(1+\tau)}\,\tan\frac{\theta_e}{2}\,G_E\,G_M \tag{9.4}$$

$$I_0 P_L = \frac{E+E'}{M}\sqrt{\tau(1+\tau)}\,\tan^2\frac{\theta_e}{2}\,G_M^2 \tag{9.5}$$

with $I_0 = G_E^2 + \frac{\tau}{\varepsilon}G_M^2$. In the Born approximation the third polarization component normal to the scattering plane vanishes. Taking the ratio of the two non-zero components gives the electric to magnetic form factor ratio:

$$\frac{G_E}{G_M} = -\frac{P_T}{P_L}\,\frac{E+E'}{2M}\,\tan\frac{\theta_e}{2}\,. \tag{9.6}$$

Table 9.2 lists the polarization experiments with which the results for the form factor ratio are compared. Not all experiments were measurements of electron-proton scattering, but also other target nuclei were used.

Table 9.2.: Polarization measurements of the electric to magnetic form factor ratio with the respective Q^2 range and the year of publication. The data is shown in figure 9.4. The experiments by Jones et al. in 2006 and by Crawford et al. are beam-asymmetry measurements.

Year	Q^2 range [(GeV/c)^2]	Reference
1998	0.38 - 0.5	Milbrath et al. [95]
2000	0.4	Dieterich et al. [96]
2000	0.49 - 3.47	Jones et al. [17]
2001	0.32 - 1.77	Gayou et al. [97]
2001	0.37 - 0.44	Pospischil et al. [98]
2002	3.5 - 5.56	Gayou et al. [99]
2005	0.50 - 3.48	Punjabi et al. [100]
2006	1.51	Jones et al. [101] $\vec{p}(\vec{e},e)p$
2006	1.13	MacLachlan et al. [102]
2007	0.16 - 0.59	Crawford et al. [103] $\vec{p}(\vec{e},e)p$
2011	2.49	Meziane et al. [104]
2011	0.22 - 0.47	Ron et al. [40]
2011	0.30 - 0.70	Zhan et al. [26]

Figure 9.4 compares the form factor ratio determined in the world data fit with the results from the polarization experiments in table 9.2. It has to be noted that the goal here is not to find the best model for the TPE correction. As already mentioned, both the phenomenological model and the resonance model predict a maximum contribution of about 2.5% to the cross section at $Q^2 = 2\,(\mathrm{GeV/c})^2$. The predictions of the two models in this range differ by less than 1% at the cross section level, which is even smaller. This is exactly in the same range as the shift of the normalization by the fit of the cross section data. With the current data it is therefore impossible to determine which model can describe the effect of the TPE the best. In Figure 9.4 one can see the change of the form factor ratio when one of the two TPE models is applied to the data. In the range below $2\,(\mathrm{GeV/c})^2$ where the MAMI data dominates the world Rosenbluth data, the trend of the form factor ratio is in good agreement with the polarization data. This is independent of the applied TPE model. At $Q^2 > 2\,(\mathrm{GeV/c})^2$ where no MAMI data exists, the models continue to diverge. The trend of the curve without any TPE model changes from a negative slope to a horizontal course. The TPE contribution from the resonance model shifts the form factor ratio towards smaller values, but is unable to describe the polarization data at higher Q^2. As in the previous case, the form factor ratio transitions from a linear decreasing ratio to an approximately constant one around $Q^2 = 2\,(\mathrm{GeV/c})^2$. The phenomenological model, on the other hand, was empirically constructed to reconcile the form factor ratio between polarized and unpolarized measurements. By design, the model attributes the full discrepancy to the TPE alone. The parameters for this model were determined in a fit to the world Rosenbluth data with the polarization data used as a constraint on the form factor ratio [20]. One can see that the curve of the phenomenological model is now slightly below the polarization data. This means that the inclusion of the cross section data measured in this work results in an overall smaller form factor ratio than before. The magnitude of the TPE contribution is now slightly overestimated by this model.

It can be concluded that the MAMI data produce a linear decreasing form factor ratio and no constant ratio like the data from previous Rosenbluth measurements. Furthermore, the TPE contribution from intermediate state resonances calculated by Ahmed et al. [63] can not explain the difference in the form factor ratio between polarized and unpolarized measurements alone. The new data measured in this work indicate that the cause for the discrepancy is more likely a combination of two factors: The TPE contribution and a different electric to magnetic form factor ratio than seen in previous unpolarized experiments.

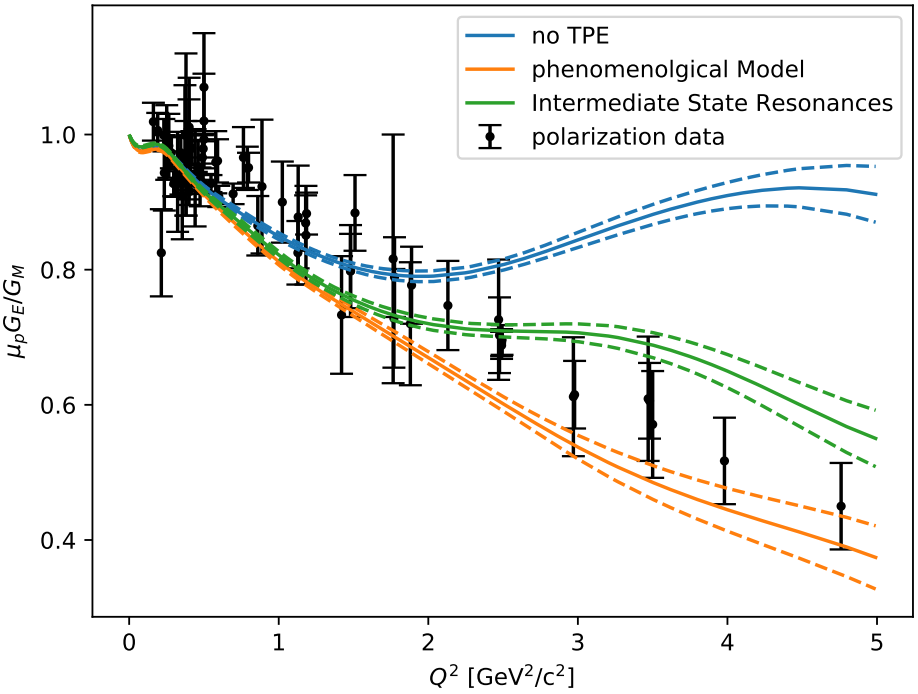

Figure 9.4.: Comparison of the form factor ratio determined in polarized and unpolarized measurements as a function of Q^2. The black data points show the form factor ratios measured in polarization experiments listed in table 9.2. The curves are fits to the world Rosenbluth data (unpolarized measurements). Shown are the results without any TPE correction (blue), with the phenomenological TPE model from [20] included (orange) and with the TPE contribution from intermediate state resonances, calculated by Ahmed et al. [63]. The dashed lines indicate the statistical uncertainty.

10. Summary and Outlook

10.1. Summary

A measurement of new elastic electron-proton scattering data at the MAMI accelerator using the 3-spectrometer setup of A1 was presented in this work. The measured cross sections are in the Q^2 range from $0.5\,(\mathrm{GeV/c})^2$ to $2\,(\mathrm{GeV/c})^2$. The data was measured primarily at the beam energies provided by the third accelerator stage of MAMI, called MAMI C. These higher beam energies had not been available in an earlier experiment at the same facility in 2010, where elastic cross sections had been measured between 0.004 and $1\,(\mathrm{GeV/c})^2$.

As a follow up experiment, the first goal of this thesis was to achieve a seamless continuation of previous measurement towards higher Q^2. The settings were therefore laid out with some kinematic overlap to get a consistent data set in the full kinematic range accessible at MAMI and A1. By employing a direct fit to the cross section data with a spline $\times$ dipole model the electric and magnetic form factors of the proton were extracted. The absolute normalization was also determined in the fit by dividing the data into groups of subsets with the same normalization and by utilizing the known values of the form factors at $Q^2 = 0$. However, the normalization by the fit proved to have stability issues, especially for the data measured at the higher beam energies. Settings excluded from the analysis were identified as the main reason for this issue: Due to a previously unknown defect in the calibration in one of the spectrometers, some settings had to be excluded from the final analysis. As a result, the kinematic overlap between the data subsets at these energies decreased significantly and, thus, the necessary constraint for the fit as well. This deficit in the MAMI data could be compensated by including the world data measured in previous experiments, which provided great stability for the fit. The fit of the world data demonstrated the excellent agreement between the experiment presented here and the previous experiment at MAMI in 2010.

The second goal was to investigate the influence of the TPE on the electric to magnetic form factor ratio of the proton, and also if the discrepancy in the form factor ratio between polarized and unpolarized experiments can be explained by the TPE correction. The extracted form factors from the fit of the world data were compared to the data from polarization experiments. The form factor ratio determined in the fit showed that the MAMI data up to a Q^2 of $2\,(\mathrm{GeV/c})^2$ produce a linear decreasing

form factor ratio, independently of the applied TPE correction. This trend has not been observed in previous unpolarized experiments. At higher Q^2 where no MAMI data exists, the TPE contribution from intermediate state resonances calculated by Ahmed et al. [63] can not explain the difference in the form factor ratio alone. These results are an indication for an overall lower electric to magnetic form factor ratio than seen in previous Rosenbluth experiments, which could play an important role in solving the discrepancy between polarized and unpolarized electron-proton scattering data.

10.2. Extraction of the Proton Radius

Since the radius of the proton is still a hotly debated topic in the field, a few comments shall be made here on how the findings of this thesis affect the extraction of the proton radius. Once more, it has to be noted that the goal of this measurement was not the determination of the proton radius itself. The main motivation was to get a consistent overall picture of the proton form factors in the kinematic range available at MAMI. Besides that, the new data at high Q^2 has very little influence on the charge radius or the magnetic radius determination and would not change the extracted values in a significant way. The extraction was therefore not redone. The analysis in this thesis could confirm the results of the experiment at MAMI in 2010, which can be seen from the excellent agreement of the cross sections in the overlap region. Since the analyses of the two experiments are independent to a large degree, this is an important confirmation that the data measured at MAMI was analyzed correctly.

Part of the debate about the proton radius is also weather the extraction of the radius from the MAMI data is done correctly [105]. The extrapolation of the slope of the form factor to $Q^2 = 0$ is thereby a central point of contention. In a reanalysis of the MAMI data in [106], Gramolin and Russell determined the proton radius by using the transverse charge density (see section 10.3.1). This technique allows to extract the radius from a wide range of data in Q^2 and does not require an extrapolation. They find a charge radius compatible with the original result in [20]. This can be interpreted as an indication that the radius of the proton was extracted correctly and that the puzzle of the proton radius is not caused by an error in the data analysis.

10.3. Outlook

10.3.1. Possible Improvements of the Analysis

On the experimental side, the biggest improvement of the analysis can be made by recovering the excluded settings, see section 4.1. This could provide the opportunity to determine the form factors from the MAMI data independently of the world data, as it was originally intended. The best way to regain the settings is to dedicate a few days of beam time to a new calibration of the optics of spectrometer A, where at least two new transfer matrices should be calibrated: The first matrix at a momentum slightly above the discontinuity in the quadrupole field, for instance at 580 MeV, and one matrix at around 630 MeV where saturation effects start to occur. Once a new calibration is available, the reconstruction of the already measured data can be easily redone and these data points can be included in the analysis. Beyond that, the number of data points in not yet measured kinematic regions can not be improved much further at MAMI/A1. Measuring at backward angles larger than 120° or at 1600 MeV would only marginally increase the kinematic range in Q^2 and ε. Moreover, the extremely high background and low count rates at these kinematics would require long measuring times for only little new data. The available kinematic range can thus be considered as covered.

For the fit of the cross section data the model based on orthogonal polynomials by Gramolin and Russell [106] could be a better alternative to the spline models. Although the spline models are reliable and easy to work with, they lack a deeper physical motivation. In [106] the Dirac and Pauli form factors F_1 and F_2 are related to the transverse charge and magnetization density. For this purpose, the space-time coordinates are changed to

$$(x^0, x^1, x^2, x^3) \rightarrow (x^+, x^-, \mathbf{b}) \tag{10.1}$$

with the light-cone variables $x^\pm = (x^0 \pm x^3)/\sqrt{2}$ and the transverse position vector $\mathbf{b} = (x^1, x^2)$. By using the infinite momentum frame where $q^+ = 0$, the four momentum has only transverse components:

$$q^\mu = (0, 0, \mathbf{q}_\perp), \quad Q^2 = \mathbf{q}_\perp^2 \tag{10.2}$$

The Dirac form factor $F_1(Q^2)$ can then be related to the transverse charge density of the proton $\rho_1(b = |\mathbf{b}|)$ via a two-dimensional Fourier transformation and the same applies for F_2 and ρ_2. The transverse densities are approximated as a dipole term times a series of orthogonal polynomials. This parameterization is chosen such that the transverse densities and the form factors can be calculated analytically. Using this model for the analysis of the data has several advantages: Unlike the spatial

charge distribution, ρ_1 has a proper density interpretation also in the relativistic case. The parameterization of F_1 and F_2 also has the same asymptotic behavior at high Q^2 as predicted by the dimensional scaling laws [107]

$$F_1 \propto \left(\frac{\Lambda}{Q}\right)^4, \quad F_2 \propto \left(\frac{\Lambda}{Q}\right)^6, \tag{10.3}$$

where Λ is the mass parameter in the dipole term. Additionally, the radius of the proton can be calculated from the mean-square of the transverse charge density:

$$r_E = \sqrt{\frac{3}{2}\left(\langle b_1^2\rangle + \frac{\kappa}{M_0^2}\right)}, \quad \langle b_1^2\rangle = 2\pi \int_0^\infty b^2 \rho_1(b) db \tag{10.4}$$

This allows to extract the radius from a wide range of data in Q^2 and does not require an extrapolation to $Q^2 = 0$.

10.3.2. MAGIX at MESA

The electron accelerator MESA (Mainz Energy-Recovering Superconducting Accelerator) provides a promising new opportunity to measure Rosenbluth data at low energies. MESA is currently under construction at the Institute for Nuclear Physics in Mainz [108, 109]. The main acceleration system consists of two cryo modules with two superconducting cavities each. MESA can be operated as an Energy Recovery Linac (ERL), where the beam is guided back into the cavities with a phase shift of 180°. The electrons are then decelerated and transfer most of their energy back to the cavities, which allows for a power-efficient acceleration of the beam. In ERL mode MESA will provide beam energies of up to 105 MeV and beam currents of more than 1 mA. The experimental setup of MAGIX (MAinz Gas Injection target eXperiment) will be operated in ERL mode of MESA. It consists of two identical high resolution spectrometers and a gas jet target [110]. An overview of the planned setup is shown in figure 10.1.

To be able to recover the beam after the interaction with the target of the experiment, only thin targets can be used. MAGIX will therefore employ a windowless gas jet target, which has already been tested at MAMI and A1 [110]. Compared to the liquid hydrogen target used in this work and in previous form factor measurements at A1, the narrow gas jet presents an almost point-like target for the electron beam, drastically reducing multiple scattering and energy loss. Moreover, because of the absence of any vacuum foils and a target cell the background will be minimal. At energies below the pion production threshold MAGIX and MESA will be an ideal facility to perform a wide range of high precision electron scattering experiments.

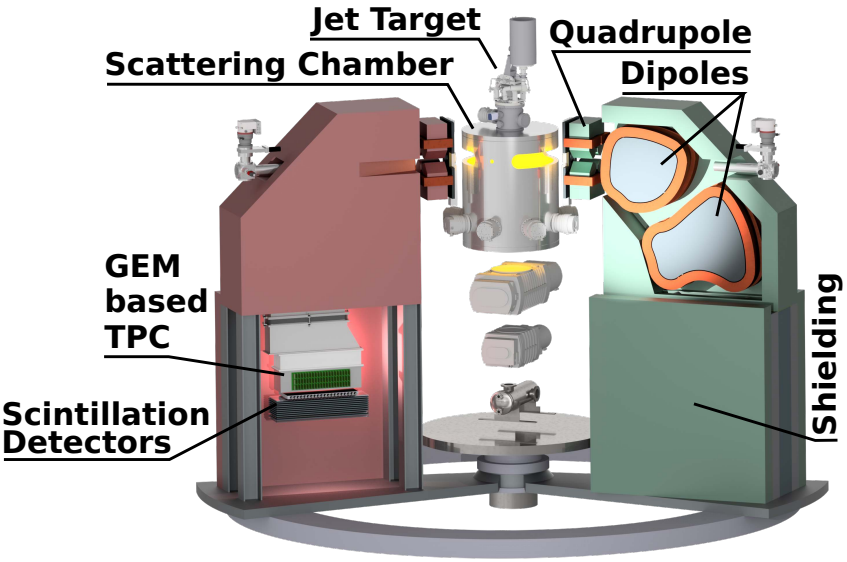

Figure 10.1.: Overview of the planned MAGIX setup [110]. The two spectrometers have a quadrupole-dipole-dipole configuration and are identical in construction. The detector setup in each spectrometer will feature a time projection chamber (TPC) for particle tracking and a trigger and veto system consisting of plastic scintillators and lead absorbers. A gas jet target will be mounted in a scattering chamber at the center of rotation.

With this setup, the form factors of the proton can be measured at Q^2 down to $10^{-4}\,(\mathrm{GeV/c})^2$ and below, which allows for a precise measurement of the proton charge radius [110]. The contribution of the magnetic form factor to the cross section is very low in this range of Q^2 and is difficult to measure precisely. At MAGIX it will however be possible to increase the sensitivity to the magnetic form factor by measuring at large backward angles. This could also provide important new insights on the slope of the magnetic form factor and the TPE at low Q^2.

A. Discontinuity in the Quadrupole Field of Spectrometer A

The coordinates of the particles are measured in the focal plane by the VDCs. The focal plane coordinates are the positions and angles of the trajectory x, θ in the dispersive direction and y, ϕ in the non-dispersive direction. Transfer matrices are used to reconstruct the target coordinates from the measured focal plane coordinates. The transformation from the focal plane coordinates to the target coordinates is parameterized in a Taylor expansion:

$$T = \sum_{i,j,k,l} \langle T | x^i \theta^j y^k \phi^l \rangle x^i \theta^j y^k \phi^l \tag{A.1}$$

where T is one of the target coordinates Y_0, Θ_0, Φ_0, δ, with $\delta = (p - p_{\mathrm{ref}})/p_{\mathrm{ref}}$, the relative difference to the reference momentum p_{ref}. The other two directions perpendicular are assumed to be zero due to the small beam spot size. The resulting coefficients are the elements of the so-called transfer matrix, which can be determined by measuring data with a sieve-slit collimator, see [111] for details.

There are two transfer matrices available for spectrometer A using an extended target: One standard matrix at 495 MeV and one matrix calibrated at the maximum central momentum of 665 MeV. During the analysis of the data of this work it was discovered that spectrometer A has a discontinuity in the current of the quadrupole at the field intensity that corresponds to a central momentum of 576.19 MeV. At this value the current in the quadrupole coils changes abruptly by about 2%, and thus, the magnetic field as well. This is caused by an error in the software for the control of the coil drive current. The discontinuity renders the standard transfer matrix unusable beyond 576.19 MeV, because it leads to a distortion in the reconstruction of the target coordinates. A consequence of this effect is depicted in figure A.1. The figure shows the difference of raw data and simulation for two adjacent settings which were measured directly one after another during the beam time. The data in the left plot was measured at a momentum slightly above the jump in the quadrupole field and the data on the right was measured below the jump. One can clearly see that the spectrum of the data is not upright like it is the case in the simulation, but is tilted to the left.

The only available transfer matrix above the discontinuity was calibrated for the maximum central momentum of 665 MeV. This matrix is only valid for high field intensities close to the maximum, because saturation effects in the iron yoke change the optics of the spectrometer. If there is a demand for the data that had to be excluded from the analysis because of the discontinuity (see section 4.1), at least two new transfer matrices should be calibrated: The first matrix at a momentum slightly above the discontinuity, for instance at 580 MeV and one matrix at around 630 MeV where saturation effects start to occur. Once a new calibration is available, the reconstruction of the already measured data can be easily redone.

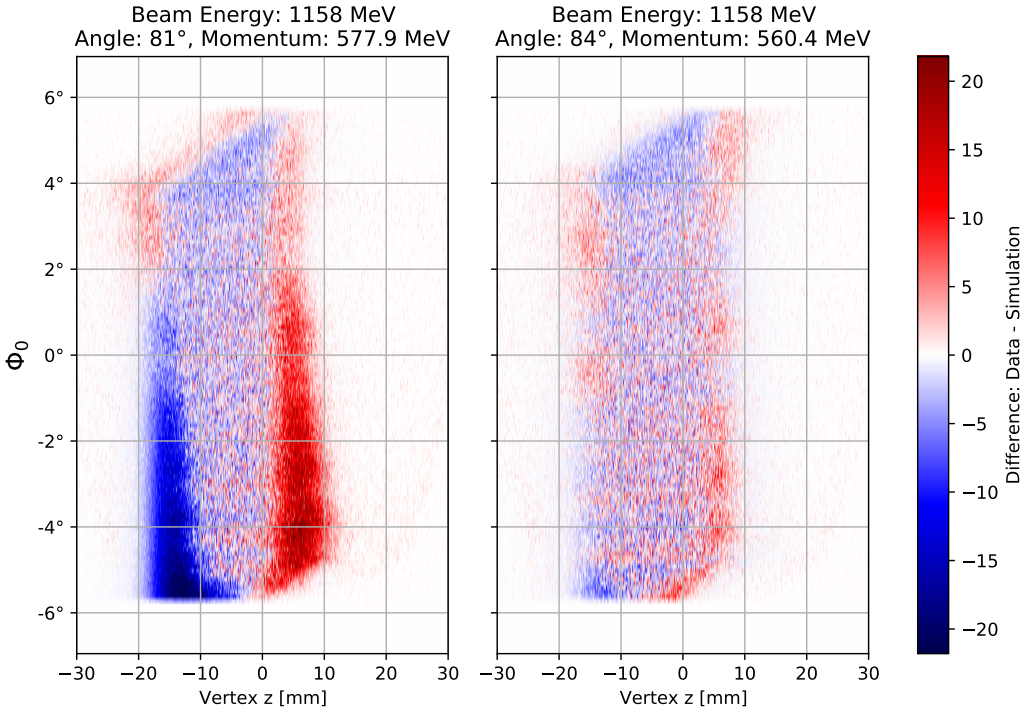

Figure A.1.: Difference of the raw data and the simulation for the in-plane target angle Φ_0 as a function of the z-coordinate of the vertex. The data shown in the left plot was measured at a momentum slightly above the jump in the quadrupole field. The spectrum of the data is not upright like in the plot on the right, but is tilted to the left due to the miss match between the quadrupole and the other magnets.

B. Form Factor and Normalization Parameters

The model used in the fit for the electric and the magnetic form factor consists of a cubic spline multiplied by the standard dipole

$$G^{E,M}_{\text{spline}\times\text{dipole}}(Q^2) = G^{E,M}(Q^2=0)\left(1+\frac{Q^2}{0.71\,(\text{GeV/c})^2}\right)^{-2}\left(1+Q^2 S^{E,M}(Q^2)\right), \tag{B.1}$$

where the model parameters are the coefficients $a_i^{E,M}$ of the B-Splines

$$S^{E,M}(x) = \sum_i^N a_i^{E,M} B_{i,k}(x)\,. \tag{B.2}$$

By construction, this model is normalized to $G^E(Q^2=0)=1$ for the electric form factor and normalized to $G^M(Q^2=0)=\mu_p$ in the case of the magnetic form factor. The knots for the spline are

$$0,\ 0.3,\ 0.65,\ 1.0,\ 1.4,\ 3.0,\ 5.0,\ 10.0,\ 40.0 \quad (\text{GeV/c})^2 \tag{B.3}$$

with the first and the last knot added three more times each for a cubic spline. Table B.1 lists the results for the parameters determined by the fit in section 9.2. An implementation of the spline × dipole model in Python using the Cox-de Boor formula is provided in listing B.1. The code calculates the form factor values in table C.3.

Apart form the model parameters, the fit also determines a large number of normalization constants. As described in section 8.1, the MAMI data is grouped into subsets of data with different normalization. The 2010 data was measured with all three spectrometers A, B, and C and, thus, requires at least three normalization constants for each beam energy. However, the number of normalization constants had to be increased because of shortcomings in the measurement. For more information on the parameters for the old MAMI data see [18]. The new data in this work was measured using only spectrometer A, so one normalization parameter was added for each beam energy. At the beam energies of 1002 MeV and above, however, two transfer matrices were used: One for the settings at momenta of 576.19 MeV/c and below, and one for the settings close to the maximum central momentum of

655 MeV/c. Since the two transfer matrices represent a different calibration of the spectrometer optics, it has to be assumed that there is a difference in the normalization of the measured data as well. Therefore, parameter 39 was introduced that accounts for a possible difference between the two transfer matrices. The external data were treated in the fit as individual normalization groups, by introducing one normalization parameter for each external data set. The normalization parameters of the world data are listed in table B.2 with the corresponding beam energy given for the MAMI data.

Listing B.1: Implementation of the spline × dipole model in Python. The code calculates the form factor values in table C.3.

```
#!/usr/bin/env python

# created by Michael O. Distler, Julian Mueller

import numpy as np


def bsplineCoeff(p, knots, u):
    """Calculates a list of the base splines with degree p, evaluated at the
    location u."""
    m = len(knots) - 1
    n = m - p - 1
    N = [0.] * (n + 1)
    if u < knots[0] or knots[m] < u:
        return np.array(N)
    if u == knots[0]:
        N[0] = 1.
        return np.array(N)
    if u == knots[m]:
        N[n] = 1.
        return np.array(N)
    for k in range(m):
        if knots[k] <= u and u < knots[k + 1]:
            break
    N[k] = 1.
    for d in range(1, p + 1):
        N[k - d] = (knots[k + 1] - u) / (knots[k + 1] -
                                         knots[k - d + 1]) * N[k - d + 1]
        for i in range(k - d + 1, k):
            N[i] = (u - knots[i]) / (knots[i + d] - knots[i]) * N[i] + (knots[
                i + d + 1] - u) / (knots[i + d + 1] - knots[i + 1]) * N[i + 1]
        N[k] = (u - knots[k]) / (knots[k + d] - knots[k]) * N[k]
    return np.array(N)


def stdDip(Q2, p=0.71):
    """standard dipole"""
    return (1 + Q2 / p)**(-2)


def cubic_spline(Q2, params, knots):
    """cubic b-spline"""
    spline = np.array([np.dot(bsplineCoeff(3, knots, i), params) for i in Q2])
    return 1 + Q2 * spline


def splineXdipole(Q2, params, knots):
    """standard dipole times cubic b-spline"""
    return stdDip(Q2) * cubic_spline(Q2, params, knots)
```

```
knots = np.array([
    0.0, 0.0, 0.0, 0.0, 0.3, 0.65, 1.0, 1.4, 3.0, 5.0, 10.0, 40.0, 40.0, 40.0,
    40.0
])
a_GE = np.array([
    -0.443268, -0.135773, -0.119749, -0.112718, -0.097350, -0.089237,
    -0.011718, 0.007465, -0.656919, 0.975318, -1.406412
])
a_GM = np.array([
    0.280497, -0.137792, 0.043312, 0.050851, 0.063651, 0.042272, 0.019299,
    0.000157, -0.026469, 0.002996, -0.019084
])
# 100 values evenly spaced on a logarithmic scale between 4e-3 and 5 (GeV/c)**2
Q2 = np.logspace(np.log10(4e-3), np.log10(5), 100)

GE = splineXdipole(Q2, a_GE, knots)
# GM / mu_p
GM = splineXdipole(Q2, a_GM, knots)
```

Table B.1.: Results for the parameters of the spline×dipole model. The data for the fit includes the radiative corrections by Maximon and Tjon, but not the Feshbach Coulomb correction and no TPE correction.

a_i	G_E	G_M
1	-0.443268	0.280497
2	-0.135773	-0.137792
3	-0.119749	0.043312
4	-0.112718	0.050851
5	-0.097350	0.063651
6	-0.089237	0.042272
7	-0.011718	0.019299
8	0.007465	0.000157
9	-0.656919	-0.026469
10	0.975318	0.002996
11	-1.406412	-0.019084

Table B.2.: Final results for the normalization parameters of the world data. The data for the fit includes the radiative corrections by Maximon and Tjon, but not the Feshbach Coulomb correction and no TPE correction.

N	Experiment	E_{Beam} [MeV]	Value	N	Experiment	E_{Beam} [MeV]	Value
1	Bernauer	180	0.999348	2	Bernauer	180	0.999501
3	Bernauer	180	1.000691	4	Bernauer	180	1.001071
5	Bernauer	180	1.000441	6	Bernauer	315	0.998627
7	Bernauer	315	1.000065	8	Bernauer	315	1.000019
9	Bernauer	315	1.001983	10	Bernauer	450	0.996970
11	Bernauer	450	1.000040	12	Bernauer	450	0.998007
13	Bernauer	450	1.003951	14	Bernauer	450	1.005546
15	Bernauer	450	1.006529	16	Bernauer	585	0.998460
17	Bernauer	585	0.998684	18	Bernauer	585	1.002768
19	Bernauer	585	1.004859	20	Bernauer	585	1.005676
21	Bernauer	720	0.998025	22	Bernauer	720	1.002034
23	Bernauer	720	0.998195	24	Bernauer	720	1.005407
25	Bernauer	720	1.006153	26	Bernauer	720	1.006052
27	Bernauer	855	0.996665	28	Bernauer	855	1.007540
29	Bernauer	855	1.008172	30	Bernauer	855	0.999241
31	Bernauer	855	1.010114	32	this work	720	1.008151
33	this work	855	1.010561	34	this work	1002	1.003870
35	this work	1158	1.006399	36	this work	1308	1.001934
37	this work	1402	0.999053	38	this work	1508	1.019030
39	this work		1.002285	40	Simon		1.001352
41	Janssens		0.973746	42	Qattan		0.983607
43	Andivahis N_1		0.966123	44	Andivahis N_2		1.007850
45	Christy		0.978172	46	Walker		0.972693
47	Sill		0.950943	48	Rock		0.919803
49	Bosted		0.965725	50	Stein		0.990585
51	Borkowski 1974		0.987045	52	Borkowski 1975		0.977321
53	Litt		0.975278	54	Price		0.992287
55	Goitein		1.006674				

C. Numerical Values for the Cross Sections and Form Factors

The elastic cross sections that were measured at MAMI are given below. Table C.1 contains the 1422 data points from 2010 with the updated normalization. The new data measured in this work are listed in table C.2. All cross section values are relative to the cross section calculated with the standard dipole form factor. The Maximon and Tjon correction was applied to the data, but not the Feshbach Coulomb correction and no TPE correction. This makes it easier to test different TPE models against the data. It is important to note that the final results presented in [18] do have the Feshbach Coulomb correction applied. The tables also specify the beam energy, the central angle of the spectrometer and the average Q^2 for each setting. The column labeled N contains the combination of normalization constants for this data point. As an example, the notation 1,3 in table C.1 means that this data point was normalized in the fit by the product of the normalization constants N_1 and N_3, see section 8.1 and equation (8.1) for details. Table C.3 contains 100 numerical values for the form factors with 1-σ statistical errors. To take the higher density of measurements at low Q^2 into account, the Q^2 values are spaced evenly on a logarithmic scale.

Table C.1.: Cross sections from the 2010 measurement at MAMI with updated normalization. No Feshbach Coulomb correction and no TPE correction was applied to the data listed here.

E_{Beam} [MeV]	Spec., θ [°]	Q^2_{avg} [$\frac{\text{GeV}^2}{\text{c}^2}$]	$\frac{\sigma_{\text{exp}}}{\sigma_{\text{dip}}}$	$\Delta\frac{\sigma_{\text{exp}}}{\sigma_{\text{dip}}}$	N	E_{Beam} [MeV]	Spec., θ [°]	Q^2_{avg} [$\frac{\text{GeV}^2}{\text{c}^2}$]	$\frac{\sigma_{\text{exp}}}{\sigma_{\text{dip}}}$	$\Delta\frac{\sigma_{\text{exp}}}{\sigma_{\text{dip}}}$	N
180	A,35.50	0.0113	0.9888	0.0031	3	180	A,35.50	0.0113	0.9924	0.0030	3
180	A,35.50	0.0113	0.9909	0.0031	3	180	A,35.50	0.0113	0.9918	0.0030	3
180	A,35.50	0.0113	0.9971	0.0038	3	180	A,35.50	0.0113	0.9898	0.0037	3
180	A,35.50	0.0113	0.9873	0.0037	3	180	A,35.50	0.0113	0.9917	0.0038	3
180	A,35.50	0.0113	0.9883	0.0038	3	180	A,35.50	0.0113	0.9939	0.0042	3
180	A,35.50	0.0113	0.9887	0.0042	3	180	A,38.00	0.0128	0.9987	0.0036	3
180	A,38.00	0.0128	0.9890	0.0035	3	180	A,38.00	0.0128	0.9902	0.0034	3
180	A,38.00	0.0128	0.9884	0.0034	3	180	A,38.00	0.0128	0.9980	0.0035	3
180	A,38.00	0.0128	0.9977	0.0035	3	180	A,40.50	0.0145	0.9910	0.0031	3
180	A,40.50	0.0145	0.9910	0.0031	3	180	A,40.50	0.0145	0.9929	0.0031	3
180	A,40.50	0.0145	0.9920	0.0031	3	180	A,43.00	0.0162	0.9915	0.0031	3
180	A,43.00	0.0162	0.9887	0.0031	3	180	A,43.00	0.0162	0.9847	0.0062	3
180	A,43.00	0.0162	0.9919	0.0030	3	180	A,43.00	0.0162	0.9925	0.0035	3
180	A,45.51	0.0180	0.9868	0.0056	3	180	A,45.51	0.0180	0.9818	0.0033	3
180	A,45.51	0.0180	0.9918	0.0029	3	180	A,48.00	0.0198	0.9888	0.0052	3
180	A,48.00	0.0198	0.9851	0.0031	3	180	A,48.00	0.0198	0.9824	0.0054	3
180	A,48.00	0.0198	0.9863	0.0036	3	180	A,48.00	0.0198	0.9863	0.0033	3
180	A,50.51	0.0217	0.9861	0.0039	3	180	A,50.51	0.0217	0.9834	0.0023	3
180	A,50.51	0.0217	0.9958	0.0054	3	180	A,50.51	0.0217	0.9811	0.0030	3
180	A,50.51	0.0217	0.9851	0.0032	3	180	A,53.01	0.0236	0.9809	0.0032	3
180	A,53.01	0.0236	0.9806	0.0038	3	180	A,53.01	0.0236	0.9857	0.0028	3
180	A,53.01	0.0236	0.9860	0.0028	3	180	A,55.50	0.0256	0.9774	0.0048	3
180	A,55.50	0.0256	0.9773	0.0029	3	180	A,55.50	0.0256	0.9776	0.0034	3
180	A,55.50	0.0256	0.9844	0.0050	3	180	A,55.50	0.0256	0.9806	0.0022	3

E_{Beam} [MeV]	Spec., θ [°]	Q^2_{avg} [$\frac{\text{GeV}^2}{\text{c}^2}$]	$\frac{\sigma_{\text{exp}}}{\sigma_{\text{dip}}}$	$\Delta\frac{\sigma_{\text{exp}}}{\sigma_{\text{dip}}}$	N	E_{Beam} [MeV]	Spec., θ [°]	Q^2_{avg} [$\frac{\text{GeV}^2}{\text{c}^2}$]	$\frac{\sigma_{\text{exp}}}{\sigma_{\text{dip}}}$	$\Delta\frac{\sigma_{\text{exp}}}{\sigma_{\text{dip}}}$	N
180	A,58.00	0.0276	0.9813	0.0047	3	180	A,58.00	0.0276	0.9809	0.0024	3
180	A,58.00	0.0276	0.9799	0.0024	3	180	A,58.00	0.0276	0.9771	0.0024	3
180	A,60.50	0.0296	0.9773	0.0021	3	180	A,63.00	0.0317	0.9801	0.0020	3
180	A,65.49	0.0338	0.9798	0.0021	3	180	A,65.49	0.0338	0.9753	0.0021	3
180	A,68.01	0.0359	0.9843	0.0021	3	180	A,68.01	0.0359	0.9839	0.0021	3
180	A,70.50	0.0380	0.9805	0.0021	3	180	A,70.50	0.0380	0.9779	0.0021	3
180	A,72.99	0.0401	0.9781	0.0019	3	180	A,75.50	0.0422	0.9818	0.0021	3
180	A,75.50	0.0422	0.9801	0.0021	3	180	A,78.00	0.0443	0.9827	0.0022	3
180	A,78.00	0.0443	0.9770	0.0021	3	180	A,80.50	0.0463	0.9764	0.0040	3
180	A,80.50	0.0463	0.9803	0.0025	3	180	A,80.50	0.0463	0.9797	0.0022	3
180	A,83.01	0.0484	0.9770	0.0045	3	180	A,83.01	0.0484	0.9817	0.0023	3
180	A,85.51	0.0505	0.9792	0.0046	3	180	A,85.51	0.0505	0.9805	0.0027	3
180	A,85.51	0.0505	0.9730	0.0023	3	180	A,85.51	0.0505	0.9732	0.0051	3
180	A,85.51	0.0505	0.9745	0.0035	3	180	A,85.51	0.0505	0.9788	0.0027	3
180	A,88.00	0.0525	0.9819	0.0051	3	180	A,88.00	0.0525	0.9817	0.0023	3
180	A,90.50	0.0545	0.9744	0.0030	3	180	A,90.50	0.0545	0.9801	0.0052	3
180	A,90.50	0.0545	0.9761	0.0021	3	180	A,93.01	0.0565	0.9741	0.0050	3
180	A,93.01	0.0565	0.9828	0.0031	3	180	A,93.01	0.0565	0.9787	0.0030	3
180	A,95.50	0.0584	0.9799	0.0053	3	180	A,95.50	0.0584	0.9796	0.0031	3
180	A,95.50	0.0584	0.9822	0.0027	3	180	A,97.99	0.0603	0.9796	0.0051	3
180	A,97.99	0.0603	0.9844	0.0030	3	180	A,97.99	0.0603	0.9783	0.0030	3
180	A,97.99	0.0603	0.9792	0.0030	3	180	A,97.99	0.0603	0.9816	0.0030	3
180	A,100.50	0.0622	0.9886	0.0046	3	180	A,100.50	0.0622	0.9771	0.0029	3
180	A,100.50	0.0622	0.9803	0.0025	3	180	A,103.00	0.0640	0.9815	0.0048	3
180	A,103.00	0.0640	0.9770	0.0035	3	180	A,103.00	0.0640	0.9804	0.0025	3
180	A,105.51	0.0658	0.9788	0.0051	3	180	A,105.51	0.0658	0.9816	0.0030	3
180	A,105.51	0.0658	0.9830	0.0026	3	180	A,90.50	0.0545	0.9856	0.0028	3
180	B,20.01	0.0038	0.9951	0.0045	1,3	180	B,20.01	0.0038	0.9984	0.0045	1,3
180	B,20.50	0.0040	0.9942	0.0046	1,3	180	B,20.50	0.0040	0.9926	0.0045	1,3
180	B,20.50	0.0040	1.0001	0.0047	1,3	180	B,20.50	0.0040	0.9926	0.0046	1,3
180	B,21.00	0.0042	0.9954	0.0047	1,3	180	B,21.50	0.0044	0.9993	0.0047	1,3
180	B,21.50	0.0044	0.9952	0.0047	1,3	180	B,22.00	0.0046	0.9925	0.0052	1,3
180	B,22.00	0.0046	0.9898	0.0052	1,3	180	B,22.00	0.0046	0.9976	0.0044	1,3
180	B,22.00	0.0046	0.9947	0.0043	1,3	180	B,22.50	0.0048	0.9940	0.0043	1,3
180	B,22.50	0.0048	0.9892	0.0043	1,3	180	B,23.00	0.0051	1.0011	0.0044	1,3
180	B,23.00	0.0050	1.0013	0.0044	1,3	180	B,23.00	0.0050	0.9957	0.0038	1,3
180	B,23.00	0.0050	0.9957	0.0038	1,3	180	B,23.51	0.0053	1.0002	0.0039	1,3
180	B,23.51	0.0053	0.9985	0.0039	1,3	180	B,23.51	0.0053	0.9991	0.0039	1,3
180	B,23.51	0.0053	0.9961	0.0039	1,3	180	B,24.01	0.0055	0.9964	0.0038	1,3
180	B,24.01	0.0055	0.9940	0.0044	1,3	180	B,24.50	0.0057	0.9909	0.0072	1,3
180	B,24.50	0.0057	0.9935	0.0042	1,3	180	B,24.50	0.0057	1.0003	0.0037	1,3
180	B,24.50	0.0057	0.9956	0.0066	1,3	180	B,24.50	0.0057	0.9961	0.0040	1,3
180	B,24.50	0.0057	0.9925	0.0068	1,3	180	B,25.01	0.0059	0.9960	0.0046	1,3
180	B,25.01	0.0059	0.9965	0.0042	1,3	180	B,25.01	0.0059	1.0012	0.0049	1,3
180	B,25.01	0.0059	0.9994	0.0030	1,3	180	B,25.50	0.0062	1.0022	0.0068	1,3
180	B,25.50	0.0062	0.9923	0.0038	1,3	180	B,25.50	0.0062	0.9939	0.0041	1,3
180	B,25.50	0.0062	0.9920	0.0040	1,3	180	B,25.50	0.0062	0.9903	0.0048	1,3
180	B,26.01	0.0064	0.9906	0.0036	1,3	180	B,26.01	0.0064	0.9914	0.0036	1,3
180	B,26.01	0.0064	0.9939	0.0061	1,3	180	B,26.01	0.0064	0.9967	0.0036	1,3
180	B,26.01	0.0064	0.9922	0.0043	1,3	180	B,26.51	0.0066	0.9942	0.0063	1,3
180	B,26.51	0.0066	0.9964	0.0029	1,3	180	B,26.51	0.0066	0.9984	0.0058	1,3
180	B,26.51	0.0066	0.9982	0.0030	1,3	180	B,26.51	0.0066	0.9968	0.0031	1,3
180	B,26.51	0.0066	0.9926	0.0030	1,3	180	B,27.00	0.0069	0.9848	0.0057	1,3
180	B,27.00	0.0069	0.9923	0.0027	1,3	180	B,27.50	0.0071	0.9934	0.0026	1,3
180	B,28.00	0.0074	0.9927	0.0027	1,3	180	B,28.00	0.0074	0.9971	0.0027	1,3
180	B,28.50	0.0077	0.9941	0.0027	1,3	180	B,28.50	0.0077	0.9895	0.0027	1,3
180	B,29.00	0.0079	0.9919	0.0026	1,3	180	B,29.00	0.0079	0.9933	0.0026	1,3
180	B,29.50	0.0082	0.9934	0.0024	1,3	180	B,29.99	0.0084	0.9907	0.0026	1,3
180	B,29.99	0.0084	0.9914	0.0026	1,3	180	B,30.50	0.0087	0.9935	0.0026	1,3
180	B,30.50	0.0087	0.9903	0.0026	1,3	180	B,31.00	0.0090	0.9908	0.0045	1,3
180	B,31.00	0.0090	0.9967	0.0030	1,3	180	B,31.00	0.0090	0.9908	0.0026	1,3
180	B,31.49	0.0093	0.9852	0.0050	1,3	180	B,31.49	0.0093	0.9897	0.0027	1,3
180	B,32.00	0.0095	0.9999	0.0051	1,3	180	B,32.00	0.0095	0.9912	0.0031	1,3
180	B,32.00	0.0095	0.9876	0.0028	1,3	180	B,32.00	0.0095	0.9928	0.0056	1,3
180	B,32.00	0.0095	0.9897	0.0039	1,3	180	B,32.00	0.0095	0.9912	0.0030	1,3
180	B,32.51	0.0098	0.9960	0.0055	1,3	180	B,32.51	0.0098	0.9952	0.0025	1,3
180	B,32.99	0.0101	0.9898	0.0032	1,3	180	B,32.99	0.0101	0.9882	0.0055	1,3
180	B,32.99	0.0101	0.9927	0.0023	1,3	180	B,33.50	0.0104	0.9898	0.0053	1,3
180	B,33.50	0.0104	0.9935	0.0032	1,3	180	B,33.50	0.0104	0.9923	0.0033	1,3
180	B,34.00	0.0107	1.0016	0.0055	1,3	180	B,34.00	0.0107	0.9928	0.0032	1,3
180	B,34.00	0.0107	0.9916	0.0028	1,3	180	B,34.50	0.0110	0.9902	0.0052	1,3
180	B,34.50	0.0110	0.9922	0.0030	1,3	180	B,34.50	0.0110	0.9916	0.0031	1,3
180	B,34.50	0.0110	0.9916	0.0031	1,3	180	B,34.50	0.0110	0.9909	0.0031	1,3
180	B,35.00	0.0113	0.9902	0.0046	1,3	180	B,35.00	0.0113	0.9944	0.0029	1,3
180	B,35.00	0.0113	0.9941	0.0025	1,3	180	B,35.50	0.0116	0.9972	0.0048	1,3
180	B,35.50	0.0116	0.9905	0.0037	1,3	180	B,35.50	0.0116	0.9911	0.0025	1,3
180	B,36.00	0.0119	0.9898	0.0049	1,3	180	B,36.00	0.0119	0.9909	0.0029	1,3
180	B,36.00	0.0119	0.9931	0.0025	1,3	180	B,36.50	0.0122	0.9879	0.0025	1,3
180	B,36.50	0.0122	0.9883	0.0025	1,3	180	B,37.00	0.0125	0.9930	0.0025	1,3
180	B,37.00	0.0125	0.9922	0.0027	1,3	180	B,37.50	0.0129	0.9937	0.0031	1,3
180	B,32.99	0.0101	0.9969	0.0033	1,4	180	B,32.99	0.0101	0.9895	0.0058	1,4

E_{Beam} [MeV]	Spec., θ [°]	Q^2_{avg} [$\frac{\text{GeV}^2}{\text{c}^2}$]	$\frac{\sigma_{\text{exp}}}{\sigma_{\text{dip}}}$	$\Delta\frac{\sigma_{\text{exp}}}{\sigma_{\text{dip}}}$	N	E_{Beam} [MeV]	Spec., θ [°]	Q^2_{avg} [$\frac{\text{GeV}^2}{\text{c}^2}$]	$\frac{\sigma_{\text{exp}}}{\sigma_{\text{dip}}}$	$\Delta\frac{\sigma_{\text{exp}}}{\sigma_{\text{dip}}}$	N
180	B,32.99	0.0101	0.9980	0.0024	1,4	180	B,37.50	0.0129	0.9894	0.0031	1,4
180	B,37.50	0.0129	0.9993	0.0033	1,4	180	B,38.01	0.0132	0.9904	0.0036	1,4
180	B,38.01	0.0132	0.9933	0.0036	1,4	180	B,38.50	0.0135	0.9895	0.0033	1,4
180	B,38.50	0.0135	0.9902	0.0033	1,4	180	B,39.00	0.0138	0.9915	0.0030	1,4
180	B,39.00	0.0138	0.9879	0.0030	1,4	180	B,39.49	0.0142	0.9900	0.0029	1,4
180	B,39.49	0.0142	0.9949	0.0029	1,4	180	B,40.50	0.0148	0.9881	0.0057	1,4
180	B,40.50	0.0148	0.9941	0.0034	1,4	180	B,40.50	0.0148	0.9933	0.0029	1,4
180	B,41.50	0.0155	0.9909	0.0024	1,4	180	B,41.50	0.0155	0.9893	0.0024	1,4
180	B,42.50	0.0162	0.9906	0.0025	1,4	180	B,42.50	0.0162	0.9861	0.0025	1,4
180	B,43.00	0.0165	0.9821	0.0048	1,4	180	B,43.00	0.0165	0.9819	0.0028	1,4
180	B,43.00	0.0165	0.9857	0.0024	1,4	180	B,43.50	0.0169	0.9901	0.0048	1,4
180	B,43.50	0.0169	0.9876	0.0028	1,4	180	B,43.50	0.0169	0.9860	0.0024	1,4
180	B,44.00	0.0172	0.9821	0.0048	1,4	180	B,44.00	0.0172	0.9894	0.0028	1,4
180	B,44.00	0.0172	0.9894	0.0024	1,4	180	B,44.51	0.0176	0.9840	0.0049	1,4
180	B,44.51	0.0176	0.9829	0.0028	1,4	180	B,44.51	0.0176	0.9900	0.0025	1,4
180	B,45.00	0.0180	0.9871	0.0049	1,4	180	B,45.00	0.0180	0.9886	0.0029	1,4
180	B,45.00	0.0180	0.9845	0.0025	1,4	180	B,45.50	0.0183	0.9903	0.0047	1,4
180	B,45.50	0.0183	0.9806	0.0028	1,4	180	B,45.50	0.0183	0.9867	0.0024	1,4
180	B,46.01	0.0187	0.9875	0.0047	1,4	180	B,46.01	0.0187	0.9812	0.0028	1,4
180	B,46.50	0.0190	0.9826	0.0048	1,4	180	B,46.50	0.0190	0.9944	0.0028	1,5
180	B,46.50	0.0190	0.9913	0.0025	1,5	180	B,47.00	0.0194	0.9865	0.0048	1,5
180	B,47.00	0.0194	0.9954	0.0029	1,5	180	B,47.00	0.0194	0.9877	0.0022	1,5
180	B,47.49	0.0198	0.9854	0.0047	1,5	180	B,47.49	0.0198	0.9894	0.0028	1,5
180	B,47.49	0.0198	0.9847	0.0023	1,5	180	B,48.00	0.0201	0.9837	0.0025	1,5
180	B,48.00	0.0201	0.9835	0.0034	1,5	180	B,48.50	0.0205	0.9830	0.0023	1,5
180	B,48.50	0.0205	0.9855	0.0023	1,5	180	B,49.00	0.0209	0.9794	0.0023	1,5
180	B,49.00	0.0209	0.9850	0.0048	1,5	180	B,49.00	0.0209	0.9878	0.0026	1,5
180	B,49.50	0.0213	0.9796	0.0023	1,5	180	B,49.50	0.0213	0.9862	0.0033	1,5
180	B,60.00	0.0295	0.9748	0.0028	1,5	180	B,60.00	0.0295	0.9758	0.0028	1,5
180	C,90.50	0.0545	0.9819	0.0038	2,4	180	C,90.50	0.0545	0.9763	0.0066	2,4
180	C,90.50	0.0545	0.9802	0.0027	2,4	180	C,90.50	0.0545	0.9707	0.0035	2,4
180	C,75.49	0.0421	0.9834	0.0030	2,4	180	C,75.49	0.0421	0.9850	0.0030	2,4
180	C,77.98	0.0442	0.9804	0.0030	2,4	180	C,77.98	0.0442	0.9753	0.0030	2,4
180	C,80.49	0.0463	0.9834	0.0036	2,4	180	C,80.49	0.0463	0.9814	0.0029	2,4
180	C,82.98	0.0484	0.9793	0.0029	2,4	180	C,82.98	0.0484	0.9793	0.0029	2,4
180	C,88.01	0.0525	0.9805	0.0061	2,4	180	C,88.01	0.0525	0.9781	0.0035	2,4
180	C,88.01	0.0525	0.9770	0.0031	2,4	180	C,93.00	0.0565	0.9763	0.0026	2,4
180	C,93.00	0.0565	0.9802	0.0026	2,4	180	C,98.01	0.0603	0.9778	0.0027	2,4
180	C,98.01	0.0603	0.9802	0.0027	2,4	180	C,100.50	0.0622	0.9811	0.0053	2,4
180	C,100.50	0.0622	0.9833	0.0027	2,4	180	C,103.00	0.0640	0.9822	0.0054	2,4
180	C,103.00	0.0640	0.9809	0.0031	2,4	180	C,103.00	0.0640	0.9731	0.0027	2,4
180	C,105.54	0.0658	0.9769	0.0055	2,4	180	C,105.54	0.0658	0.9856	0.0032	2,4
180	C,105.54	0.0658	0.9814	0.0032	2,4	180	C,108.04	0.0676	0.9845	0.0056	2,4
180	C,108.04	0.0676	0.9786	0.0032	2,4	180	C,108.04	0.0676	0.9800	0.0028	2,4
180	C,110.51	0.0693	0.9821	0.0033	2,4	180	C,110.51	0.0693	0.9821	0.0029	2,4
180	C,113.06	0.0710	0.9771	0.0058	2,4	180	C,113.06	0.0710	0.9796	0.0034	2,4
180	C,113.06	0.0710	0.9822	0.0029	2,4	180	C,115.56	0.0726	0.9844	0.0058	2,4
180	C,115.56	0.0726	0.9816	0.0035	2,4	180	C,117.94	0.0740	0.9794	0.0060	2,4
180	C,117.94	0.0740	0.9883	0.0036	2,5	180	C,117.94	0.0740	0.9898	0.0031	2,5
180	C,120.49	0.0756	0.9852	0.0062	2,5	180	C,123.08	0.0771	0.9890	0.0061	2,5
180	C,123.08	0.0771	0.9885	0.0037	2,5	180	C,123.08	0.0771	0.9895	0.0029	2,5
180	C,125.59	0.0785	0.9931	0.0033	2,5	180	C,125.59	0.0785	0.9957	0.0045	2,5
180	C,128.02	0.0798	0.9896	0.0030	2,5	180	C,128.02	0.0798	0.9927	0.0030	2,5
180	C,130.55	0.0811	0.9921	0.0031	2,5	180	C,130.55	0.0811	0.9956	0.0065	2,5
180	C,130.55	0.0811	0.9917	0.0035	2,5	180	C,132.95	0.0822	0.9873	0.0032	2,5
180	C,132.95	0.0822	0.9871	0.0045	2,5	180	C,135.53	0.0834	0.9920	0.0032	2,5
180	C,135.53	0.0834	0.9860	0.0032	2,5	315	A,43.00	0.0479	0.9771	0.0027	9
315	A,43.00	0.0479	0.9744	0.0030	9	315	A,43.00	0.0479	0.9710	0.0027	9
315	A,43.00	0.0479	0.9728	0.0027	9	315	A,43.00	0.0479	0.9739	0.0029	9
315	A,43.00	0.0479	0.9725	0.0027	9	315	A,43.00	0.0479	0.9680	0.0027	9
315	A,43.00	0.0479	0.9761	0.0024	9	315	A,43.00	0.0479	0.9747	0.0024	9
315	A,43.00	0.0479	0.9762	0.0024	9	315	A,43.00	0.0479	0.9740	0.0024	9
315	A,43.00	0.0479	0.9713	0.0024	9	315	A,43.00	0.0479	0.9765	0.0024	9
315	A,43.00	0.0479	0.9739	0.0024	9	315	A,48.00	0.0582	0.9759	0.0024	9
315	A,48.00	0.0582	0.9736	0.0024	9	315	A,48.00	0.0582	0.9721	0.0025	9
315	A,48.00	0.0582	0.9753	0.0025	9	315	A,48.00	0.0582	0.9691	0.0024	9
315	A,48.00	0.0582	0.9756	0.0025	9	315	A,53.01	0.0688	0.9709	0.0024	9
315	A,53.01	0.0688	0.9713	0.0024	9	315	A,53.01	0.0688	0.9689	0.0024	9
315	A,53.01	0.0688	0.9697	0.0024	9	315	A,58.00	0.0797	0.9654	0.0030	9
315	A,58.00	0.0797	0.9701	0.0025	9	315	A,58.00	0.0797	0.9694	0.0024	9
315	A,63.00	0.0908	0.9664	0.0027	9	315	A,63.00	0.0908	0.9708	0.0027	9
315	A,68.01	0.1018	0.9729	0.0030	9	315	A,73.01	0.1128	0.9672	0.0033	9
315	A,73.01	0.1128	0.9713	0.0033	9	315	A,78.00	0.1235	0.9749	0.0028	9
315	A,78.00	0.1235	0.9735	0.0028	9	315	A,83.01	0.1340	0.9692	0.0033	9
315	A,83.01	0.1340	0.9724	0.0034	9	315	A,82.99	0.1340	0.9705	0.0033	9
315	A,82.99	0.1340	0.9683	0.0033	9	315	A,88.00	0.1441	0.9733	0.0033	9
315	A,88.00	0.1441	0.9736	0.0033	9	315	A,40.50	0.0430	0.9702	0.0035	7,9
315	A,40.50	0.0430	0.9762	0.0035	7,9	315	A,40.50	0.0430	0.9745	0.0037	7,9
315	A,40.50	0.0430	0.9757	0.0027	7,9	315	A,40.50	0.0430	0.9768	0.0027	7,9
315	A,40.50	0.0430	0.9759	0.0027	7,9	315	A,40.50	0.0430	0.9758	0.0027	7,9
315	A,40.50	0.0430	0.9744	0.0025	7,9	315	A,40.50	0.0430	0.9767	0.0025	7,9

E_{Beam} [MeV]	Spec., θ [°]	Q^2_{avg} [$\frac{\text{GeV}^2}{\text{c}^2}$]	$\frac{\sigma_{\text{exp}}}{\sigma_{\text{dip}}}$	$\Delta\frac{\sigma_{\text{exp}}}{\sigma_{\text{dip}}}$	N	E_{Beam} [MeV]	Spec., θ [°]	Q^2_{avg} [$\frac{\text{GeV}^2}{\text{c}^2}$]	$\frac{\sigma_{\text{exp}}}{\sigma_{\text{dip}}}$	$\Delta\frac{\sigma_{\text{exp}}}{\sigma_{\text{dip}}}$	N
315	A,45.51	0.0530	0.9777	0.0024	7,9	315	A,45.51	0.0530	0.9759	0.0024	7,9
315	A,45.51	0.0530	0.9767	0.0024	7,9	315	A,45.51	0.0530	0.9759	0.0024	7,9
315	A,45.51	0.0530	0.9713	0.0024	7,9	315	A,45.51	0.0530	0.9733	0.0024	7,9
315	A,50.50	0.0634	0.9711	0.0023	7,9	315	A,50.50	0.0634	0.9713	0.0023	7,9
315	A,50.50	0.0634	0.9734	0.0023	7,9	315	A,50.50	0.0634	0.9741	0.0022	7,9
315	A,55.50	0.0742	0.9677	0.0021	7,9	315	A,55.50	0.0742	0.9694	0.0021	7,9
315	A,55.50	0.0742	0.9689	0.0025	7,9	315	A,55.50	0.0742	0.9710	0.0025	7,9
315	A,60.50	0.0852	0.9663	0.0026	7,9	315	A,60.50	0.0852	0.9714	0.0027	7,9
315	A,60.50	0.0852	0.9685	0.0026	7,9	315	A,60.50	0.0852	0.9665	0.0027	7,9
315	A,65.51	0.0963	0.9692	0.0031	7,9	315	A,70.50	0.1073	0.9692	0.0034	7,9
315	A,70.50	0.1073	0.9686	0.0034	7,9	315	A,75.50	0.1182	0.9692	0.0035	7,9
315	A,75.50	0.1182	0.9698	0.0035	7,9	315	A,80.51	0.1288	0.9720	0.0033	7,9
315	A,85.51	0.1391	0.9697	0.0033	7,9	315	A,80.50	0.1288	0.9672	0.0032	7,9
315	A,80.50	0.1288	0.9724	0.0033	7,9	315	A,85.49	0.1391	0.9725	0.0033	7,9
315	A,85.49	0.1391	0.9707	0.0033	7,9	315	B,19.50	0.0111	0.9853	0.0047	6,9
315	B,19.99	0.0116	0.9868	0.0031	6,9	315	B,19.99	0.0116	0.9875	0.0031	6,9
315	B,20.50	0.0122	0.9899	0.0032	6,9	315	B,20.50	0.0122	0.9894	0.0032	6,9
315	B,21.00	0.0128	0.9839	0.0033	6,9	315	B,21.00	0.0128	0.9921	0.0033	6,9
315	B,21.50	0.0134	0.9884	0.0033	6,9	315	B,21.50	0.0134	0.9894	0.0031	6,9
315	B,21.50	0.0134	0.9918	0.0032	6,9	315	B,22.00	0.0140	0.9845	0.0032	6,9
315	B,22.00	0.0140	0.9885	0.0032	6,9	315	B,22.50	0.0146	0.9855	0.0033	6,9
315	B,22.50	0.0146	0.9872	0.0033	6,9	315	B,22.50	0.0146	0.9897	0.0031	6,9
315	B,22.50	0.0146	0.9897	0.0031	6,9	315	B,23.00	0.0153	0.9912	0.0032	6,9
315	B,23.00	0.0153	0.9906	0.0032	6,9	315	B,23.51	0.0159	0.9892	0.0033	6,9
315	B,23.51	0.0159	0.9903	0.0033	6,9	315	B,23.51	0.0159	0.9858	0.0030	6,9
315	B,23.51	0.0159	0.9890	0.0030	6,9	315	B,24.00	0.0166	0.9865	0.0030	6,9
315	B,24.00	0.0166	0.9893	0.0030	6,9	315	B,24.00	0.0166	0.9892	0.0030	6,9
315	B,24.00	0.0166	0.9872	0.0030	6,9	315	B,24.50	0.0173	0.9816	0.0031	6,9
315	B,24.50	0.0173	0.9841	0.0031	6,9	315	B,24.50	0.0173	0.9841	0.0026	6,9
315	B,24.50	0.0173	0.9833	0.0026	6,9	315	B,25.01	0.0180	0.9829	0.0031	6,9
315	B,25.01	0.0180	0.9866	0.0031	6,9	315	B,25.01	0.0180	0.9847	0.0035	6,9
315	B,25.50	0.0186	0.9881	0.0030	6,9	315	B,25.50	0.0186	0.9868	0.0030	6,9
315	B,25.50	0.0186	0.9863	0.0030	6,9	315	B,25.50	0.0186	0.9832	0.0031	6,9
315	B,26.00	0.0193	0.9912	0.0031	6,9	315	B,26.00	0.0193	0.9853	0.0031	6,9
315	B,26.51	0.0201	0.9855	0.0030	6,9	315	B,26.51	0.0201	0.9872	0.0031	6,9
315	B,27.00	0.0208	0.9877	0.0034	6,9	315	B,27.50	0.0215	0.9866	0.0032	6,9
315	B,28.00	0.0223	0.9865	0.0033	6,9	315	B,28.00	0.0223	0.9904	0.0033	6,9
315	B,28.50	0.0230	0.9832	0.0032	6,9	315	B,28.50	0.0230	0.9873	0.0032	6,9
315	B,29.00	0.0238	0.9917	0.0033	6,9	315	B,29.00	0.0238	0.9889	0.0033	6,9
315	B,29.50	0.0246	0.9871	0.0031	6,9	315	B,29.50	0.0246	0.9894	0.0031	6,9
315	B,30.01	0.0254	0.9882	0.0033	6,9	315	B,30.50	0.0262	0.9805	0.0033	6,9
315	B,30.50	0.0262	0.9806	0.0033	6,9	315	B,31.00	0.0270	0.9753	0.0033	6,9
315	B,30.01	0.0254	0.9726	0.0029	6,9	315	B,30.01	0.0254	0.9768	0.0030	6,9
315	B,30.50	0.0262	0.9802	0.0031	6,9	315	B,30.50	0.0262	0.9841	0.0031	6,9
315	B,31.00	0.0270	0.9826	0.0031	6,9	315	B,31.00	0.0270	0.9817	0.0031	6,9
315	B,31.51	0.0278	0.9789	0.0032	6,9	315	B,31.51	0.0278	0.9827	0.0032	6,9
315	B,32.00	0.0286	0.9801	0.0026	6,9	315	B,32.00	0.0286	0.9856	0.0032	6,9
315	B,32.00	0.0286	0.9814	0.0032	6,9	315	B,32.51	0.0295	0.9806	0.0025	6,9
315	B,33.01	0.0303	0.9822	0.0024	6,9	315	B,33.50	0.0312	0.9788	0.0026	6,9
315	B,33.50	0.0312	0.9797	0.0026	6,9	315	B,34.00	0.0320	0.9799	0.0027	6,9
315	B,34.00	0.0320	0.9822	0.0027	6,9	315	B,35.00	0.0338	0.9757	0.0022	6,9
315	B,35.00	0.0338	0.9782	0.0022	6,9	315	B,35.51	0.0347	0.9801	0.0021	6,9
315	B,35.51	0.0347	0.9754	0.0021	6,9	315	B,36.00	0.0355	0.9797	0.0025	6,9
315	B,36.00	0.0355	0.9791	0.0022	6,9	315	B,36.50	0.0365	0.9735	0.0037	6,9
315	B,37.00	0.0374	0.9776	0.0035	6,9	315	B,37.00	0.0374	0.9754	0.0035	6,9
315	B,38.01	0.0393	0.9780	0.0026	6,9	315	B,34.50	0.0329	0.9746	0.0022	6,9
315	B,38.01	0.0393	0.9793	0.0026	6,9	315	B,38.50	0.0402	0.9833	0.0024	6,9
315	B,38.50	0.0402	0.9793	0.0024	6,9	315	B,39.00	0.0411	0.9754	0.0022	6,9
315	B,39.00	0.0411	0.9758	0.0022	6,9	315	B,39.51	0.0421	0.9800	0.0022	6,9
315	B,39.51	0.0421	0.9783	0.0022	6,9	315	B,40.00	0.0430	0.9807	0.0022	6,9
315	B,40.00	0.0430	0.9775	0.0022	6,9	315	B,40.50	0.0440	0.9727	0.0021	6,9
315	B,41.01	0.0450	0.9745	0.0021	6,9	315	B,41.01	0.0450	0.9756	0.0021	6,9
315	B,41.50	0.0459	0.9745	0.0021	6,9	315	B,41.50	0.0459	0.9762	0.0021	6,9
315	B,42.00	0.0469	0.9799	0.0021	6,9	315	B,42.00	0.0469	0.9764	0.0021	6,9
315	B,42.50	0.0479	0.9730	0.0021	6,9	315	B,42.50	0.0479	0.9745	0.0021	6,9
315	B,43.00	0.0489	0.9748	0.0018	6,9	315	B,43.00	0.0489	0.9786	0.0018	6,9
315	B,43.00	0.0489	0.9765	0.0018	6,9	315	C,73.01	0.1128	0.9744	0.0032	8,9
315	C,73.01	0.1128	0.9746	0.0030	8,9	315	C,73.01	0.1128	0.9756	0.0030	8,9
315	C,90.50	0.1490	0.9711	0.0042	8,9	315	C,73.01	0.1128	0.9745	0.0029	8,9
315	C,73.01	0.1128	0.9734	0.0028	8,9	315	C,90.50	0.1490	0.9709	0.0040	8,9
315	C,90.50	0.1490	0.9634	0.0037	8,9	315	C,90.50	0.1490	0.9694	0.0039	8,9
315	C,90.50	0.1490	0.9685	0.0039	8,9	315	C,90.50	0.1490	0.9695	0.0040	8,9
315	C,90.50	0.1490	0.9740	0.0040	8,9	315	C,90.50	0.1490	0.9652	0.0032	8,9
315	C,90.50	0.1490	0.9702	0.0032	8,9	315	C,90.50	0.1491	0.9681	0.0031	8,9
315	C,90.50	0.1490	0.9694	0.0031	8,9	315	C,90.50	0.1490	0.9696	0.0037	8,9
315	C,90.50	0.1490	0.9689	0.0031	8,9	315	C,74.54	0.1161	0.9688	0.0021	8,9
315	C,75.49	0.1181	0.9705	0.0022	8,9	315	C,75.49	0.1181	0.9715	0.0022	8,9
315	C,80.49	0.1287	0.9703	0.0024	8,9	315	C,90.50	0.1490	0.9652	0.0032	8,9
315	C,80.49	0.1287	0.9677	0.0024	8,9	315	C,83.02	0.1340	0.9637	0.0025	8,9
315	C,83.02	0.1340	0.9643	0.0025	8,9	315	C,85.51	0.1391	0.9667	0.0025	8,9
315	C,85.51	0.1391	0.9660	0.0025	8,9	315	C,88.01	0.1441	0.9673	0.0026	8,9

E_{Beam} [MeV]	Spec., θ [°]	Q^2_{avg} [$\frac{\text{GeV}^2}{\text{c}^2}$]	$\frac{\sigma_{\text{exp}}}{\sigma_{\text{dip}}}$	$\Delta\frac{\sigma_{\text{exp}}}{\sigma_{\text{dip}}}$	N	E_{Beam} [MeV]	Spec., θ [°]	Q^2_{avg} [$\frac{\text{GeV}^2}{\text{c}^2}$]	$\frac{\sigma_{\text{exp}}}{\sigma_{\text{dip}}}$	$\Delta\frac{\sigma_{\text{exp}}}{\sigma_{\text{dip}}}$	N
315	C,88.01	0.1441	0.9644	0.0026	8,9	315	C,90.50	0.1490	0.9715	0.0027	8,9
315	C,90.50	0.1490	0.9667	0.0027	8,9	315	C,93.00	0.1538	0.9635	0.0026	8,9
315	C,95.49	0.1585	0.9677	0.0027	8,9	315	C,98.01	0.1631	0.9654	0.0028	8,9
315	C,98.01	0.1631	0.9670	0.0027	8,9	315	C,100.50	0.1675	0.9735	0.0028	8,9
315	C,103.00	0.1719	0.9676	0.0029	8,9	315	C,103.00	0.1719	0.9687	0.0030	8,9
315	C,105.54	0.1761	0.9711	0.0026	8,9	315	C,105.54	0.1761	0.9738	0.0026	8,9
315	C,105.54	0.1761	0.9720	0.0026	8,9	315	C,108.04	0.1802	0.9710	0.0032	8,9
315	C,108.04	0.1802	0.9715	0.0032	8,9	315	C,110.53	0.1841	0.9723	0.0029	8,9
315	C,110.53	0.1841	0.9690	0.0029	8,9	315	C,113.06	0.1880	0.9696	0.0029	8,9
315	C,113.06	0.1880	0.9713	0.0030	8,9	315	C,115.56	0.1916	0.9718	0.0031	8,9
315	C,115.56	0.1916	0.9751	0.0031	8,9	315	C,117.94	0.1949	0.9717	0.0032	8,9
315	C,117.94	0.1949	0.9717	0.0032	8,9	315	C,120.49	0.1984	0.9749	0.0033	8,9
315	C,120.49	0.1984	0.9773	0.0033	8,9	315	C,123.08	0.2017	0.9750	0.0034	8,9
315	C,123.08	0.2017	0.9751	0.0034	8,9	315	C,125.59	0.2048	0.9829	0.0035	8,9
315	C,125.59	0.2048	0.9788	0.0035	8,9	315	C,130.55	0.2105	0.9789	0.0035	8,9
315	C,130.55	0.2105	0.9797	0.0035	8,9	315	C,132.95	0.2131	0.9770	0.0034	8,9
315	C,132.95	0.2131	0.9769	0.0034	8,9	450	A,33.01	0.0586	0.9612	0.0070	13
450	A,33.01	0.0586	0.9658	0.0065	13	450	A,33.01	0.0586	0.9743	0.0066	13
450	A,38.00	0.0758	0.9692	0.0076	13	450	A,38.00	0.0758	0.9727	0.0060	13
450	A,38.00	0.0758	0.9702	0.0060	13	450	A,38.00	0.0758	0.9717	0.0060	13
450	A,43.00	0.0943	0.9692	0.0045	13	450	A,43.00	0.0943	0.9720	0.0045	13
450	A,43.00	0.0943	0.9727	0.0046	13	450	A,43.00	0.0943	0.9693	0.0046	13
450	A,43.00	0.0943	0.9721	0.0034	13	450	A,43.00	0.0943	0.9700	0.0048	13
450	A,43.00	0.0943	0.9734	0.0061	13	450	A,43.00	0.0943	0.9691	0.0062	13
450	A,43.00	0.0943	0.9673	0.0057	13	450	A,43.00	0.0943	0.9702	0.0057	13
450	A,43.00	0.0943	0.9767	0.0052	13	450	A,43.00	0.0943	0.9713	0.0052	13
450	A,43.00	0.0943	0.9708	0.0052	13	450	A,43.00	0.0943	0.9710	0.0059	13
450	A,48.00	0.1137	0.9695	0.0045	13	450	A,48.00	0.1137	0.9691	0.0045	13
450	A,48.00	0.1137	0.9646	0.0044	13	450	A,48.00	0.1137	0.9614	0.0045	13
450	A,48.00	0.1137	0.9688	0.0035	13	450	A,53.01	0.1336	0.9577	0.0042	13
450	A,53.01	0.1336	0.9646	0.0042	13	450	A,53.01	0.1336	0.9603	0.0033	13
450	A,58.00	0.1537	0.9602	0.0045	13	450	A,58.00	0.1537	0.9624	0.0037	13
450	A,63.00	0.1737	0.9581	0.0047	13	450	A,63.00	0.1737	0.9597	0.0039	13
450	A,68.01	0.1934	0.9593	0.0031	13	450	A,73.01	0.2127	0.9593	0.0036	13
450	A,73.01	0.2127	0.9606	0.0036	13	450	A,78.00	0.2313	0.9627	0.0037	13
450	A,78.00	0.2313	0.9636	0.0037	13	450	A,83.01	0.2493	0.9654	0.0033	13
450	A,83.01	0.2492	0.9692	0.0047	13	450	A,88.00	0.2663	0.9718	0.0037	13
450	A,88.00	0.2663	0.9661	0.0037	13	450	A,90.50	0.2745	0.9648	0.0028	14
450	A,90.50	0.2745	0.9618	0.0028	14	450	A,35.51	0.0670	0.9686	0.0067	11,13
450	A,35.51	0.0670	0.9676	0.0066	11,13	450	A,35.51	0.0670	0.9641	0.0064	11,13
450	A,35.51	0.0670	0.9724	0.0064	11,13	450	A,40.50	0.0849	0.9701	0.0053	11,13
450	A,40.50	0.0849	0.9774	0.0054	11,13	450	A,40.50	0.0849	0.9768	0.0054	11,13
450	A,40.50	0.0849	0.9768	0.0054	11,13	450	A,40.50	0.0849	0.9718	0.0039	11,13
450	A,40.50	0.0849	0.9769	0.0039	11,13	450	A,45.51	0.1039	0.9639	0.0051	11,13
450	A,45.51	0.1039	0.9692	0.0051	11,13	450	A,45.51	0.1039	0.9687	0.0040	11,13
450	A,45.51	0.1039	0.9655	0.0048	11,13	450	A,45.51	0.1039	0.9699	0.0047	11,13
450	A,50.51	0.1236	0.9673	0.0033	11,13	450	A,50.51	0.1236	0.9591	0.0041	11,13
450	A,50.51	0.1236	0.9654	0.0041	11,13	450	A,55.50	0.1435	0.9643	0.0034	11,13
450	A,55.50	0.1435	0.9615	0.0031	11,13	450	A,55.50	0.1435	0.9601	0.0039	11,13
450	A,55.50	0.1435	0.9623	0.0039	11,13	450	A,60.50	0.1636	0.9586	0.0036	11,13
450	A,60.50	0.1636	0.9594	0.0036	11,13	450	A,65.49	0.1835	0.9594	0.0038	11,13
450	A,65.49	0.1835	0.9576	0.0038	11,13	450	A,70.50	0.2030	0.9608	0.0034	11,13
450	A,70.50	0.2030	0.9569	0.0034	11,13	450	A,75.50	0.2220	0.9613	0.0043	11,13
450	A,75.50	0.2220	0.9616	0.0035	11,13	450	A,80.50	0.2403	0.9607	0.0039	11,13
450	A,80.50	0.2403	0.9654	0.0039	11,13	450	A,85.51	0.2578	0.9659	0.0034	11,13
450	A,85.51	0.2578	0.9676	0.0040	11,13	450	A,90.50	0.2744	0.9701	0.0038	11,13
450	A,90.50	0.2744	0.9706	0.0036	11,13	450	B,16.00	0.0152	0.9783	0.0065	10,13
450	B,16.00	0.0152	0.9857	0.0066	10,13	450	B,16.00	0.0152	0.9761	0.0065	10,13
450	B,16.00	0.0152	0.9762	0.0065	10,13	450	B,16.50	0.0162	0.9724	0.0063	10,13
450	B,16.50	0.0162	0.9782	0.0064	10,13	450	B,16.50	0.0162	0.9792	0.0075	10,13
450	B,16.50	0.0162	0.9802	0.0060	10,13	450	B,17.01	0.0172	0.9757	0.0060	10,13
450	B,17.01	0.0172	0.9810	0.0060	10,13	450	B,17.01	0.0172	0.9811	0.0054	10,13
450	B,17.01	0.0172	0.9840	0.0054	10,13	450	B,17.50	0.0182	0.9840	0.0055	10,13
450	B,17.50	0.0182	0.9870	0.0055	10,13	450	B,18.00	0.0192	0.9771	0.0042	10,13
450	B,18.49	0.0202	0.9777	0.0042	10,13	450	B,18.49	0.0202	0.9776	0.0047	10,13
450	B,18.49	0.0202	0.9801	0.0048	10,13	450	B,19.00	0.0213	0.9779	0.0049	10,13
450	B,19.00	0.0213	0.9805	0.0049	10,13	450	B,19.50	0.0224	0.9795	0.0041	10,13
450	B,19.50	0.0224	0.9794	0.0046	10,13	450	B,20.01	0.0236	0.9830	0.0059	10,13
450	B,20.01	0.0236	0.9781	0.0060	10,13	450	B,20.50	0.0247	0.9760	0.0055	10,13
450	B,20.50	0.0247	0.9822	0.0055	10,13	450	B,21.00	0.0259	0.9837	0.0050	10,13
450	B,21.00	0.0259	0.9800	0.0050	10,13	450	B,21.50	0.0271	0.9749	0.0050	10,13
450	B,21.50	0.0271	0.9773	0.0057	10,13	450	B,21.50	0.0271	0.9756	0.0049	10,13
450	B,21.50	0.0271	0.9760	0.0049	10,13	450	B,22.00	0.0283	0.9771	0.0039	10,13
450	B,22.50	0.0296	0.9779	0.0047	10,13	450	B,22.50	0.0296	0.9827	0.0046	10,13
450	B,22.50	0.0296	0.9811	0.0043	10,13	450	B,22.50	0.0296	0.9815	0.0044	10,13
450	B,23.00	0.0308	0.9778	0.0043	10,13	450	B,23.00	0.0308	0.9730	0.0043	10,13
450	B,23.51	0.0322	0.9820	0.0034	10,13	450	B,23.51	0.0322	0.9795	0.0032	10,13
450	B,24.00	0.0334	0.9773	0.0040	10,13	450	B,24.00	0.0334	0.9757	0.0040	10,13
450	B,24.00	0.0334	0.9771	0.0040	10,13	450	B,24.00	0.0334	0.9804	0.0040	10,13
450	B,24.50	0.0348	0.9804	0.0032	10,13	450	B,24.50	0.0348	0.9808	0.0032	10,13
450	B,24.50	0.0348	0.9768	0.0029	10,13	450	B,25.01	0.0362	0.9778	0.0037	10,13

E_{Beam} [MeV]	Spec., θ [°]	Q^2_{avg} [$\frac{\text{GeV}^2}{\text{c}^2}$]	$\frac{\sigma_{\text{exp}}}{\sigma_{\text{dip}}}$	$\Delta\frac{\sigma_{\text{exp}}}{\sigma_{\text{dip}}}$	N	E_{Beam} [MeV]	Spec., θ [°]	Q^2_{avg} [$\frac{\text{GeV}^2}{\text{c}^2}$]	$\frac{\sigma_{\text{exp}}}{\sigma_{\text{dip}}}$	$\Delta\frac{\sigma_{\text{exp}}}{\sigma_{\text{dip}}}$	N
450	B,25.01	0.0362	0.9790	0.0037	10,13	450	B,25.50	0.0375	0.9792	0.0042	10,13
450	B,25.50	0.0375	0.9806	0.0035	10,13	450	B,26.00	0.0389	0.9787	0.0034	10,13
450	B,26.00	0.0389	0.9755	0.0034	10,13	450	B,26.49	0.0403	0.9798	0.0043	10,13
450	B,26.49	0.0403	0.9803	0.0035	10,13	450	B,27.00	0.0418	0.9807	0.0034	10,13
450	B,27.00	0.0418	0.9760	0.0034	10,13	450	B,27.50	0.0432	0.9776	0.0028	10,13
450	B,28.00	0.0447	0.9787	0.0030	10,13	450	B,28.00	0.0447	0.9747	0.0030	10,13
450	B,28.50	0.0462	0.9768	0.0031	10,13	450	B,28.50	0.0462	0.9772	0.0031	10,13
450	B,29.00	0.0477	0.9766	0.0036	10,13	450	B,29.00	0.0477	0.9773	0.0030	10,13
450	B,29.50	0.0493	0.9783	0.0030	10,13	450	B,29.50	0.0493	0.9799	0.0030	10,13
450	B,29.99	0.0508	0.9749	0.0031	10,13	450	B,29.99	0.0508	0.9740	0.0031	10,13
450	B,30.50	0.0524	0.9760	0.0028	10,13	450	B,30.50	0.0524	0.9784	0.0038	10,13
450	B,31.00	0.0540	0.9733	0.0028	10,13	450	B,31.00	0.0540	0.9761	0.0034	10,13
450	B,31.51	0.0556	0.9722	0.0029	10,13	450	B,32.00	0.0572	0.9736	0.0030	10,13
450	B,31.51	0.0556	0.9746	0.0030	10,13	450	B,32.00	0.0572	0.9758	0.0029	10,13
450	B,32.50	0.0589	0.9728	0.0033	10,14	450	B,32.50	0.0589	0.9724	0.0032	10,14
450	B,33.01	0.0605	0.9718	0.0032	10,14	450	B,33.01	0.0605	0.9688	0.0032	10,14
450	B,33.50	0.0622	0.9729	0.0033	10,14	450	B,33.50	0.0622	0.9733	0.0033	10,14
450	B,34.00	0.0639	0.9685	0.0030	10,14	450	B,34.00	0.0639	0.9688	0.0030	10,14
450	B,34.50	0.0655	0.9702	0.0029	10,14	450	B,34.50	0.0655	0.9706	0.0029	10,14
450	B,35.00	0.0673	0.9718	0.0027	10,14	450	B,35.50	0.0690	0.9730	0.0029	10,14
450	B,35.50	0.0690	0.9734	0.0029	10,14	450	B,36.00	0.0707	0.9705	0.0029	10,14
450	B,36.00	0.0707	0.9740	0.0029	10,14	450	B,40.00	0.0851	0.9670	0.0025	10,14
450	B,40.00	0.0851	0.9663	0.0024	10,14	450	B,32.00	0.0572	0.9736	0.0037	10,15
450	B,32.00	0.0572	0.9753	0.0035	10,15	450	B,32.00	0.0572	0.9774	0.0026	10,15
450	B,36.50	0.0725	0.9613	0.0034	10,15	450	B,36.50	0.0725	0.9635	0.0034	10,15
450	B,37.00	0.0743	0.9630	0.0033	10,15	450	B,37.00	0.0743	0.9618	0.0033	10,15
450	B,37.50	0.0761	0.9680	0.0029	10,15	450	B,37.50	0.0761	0.9681	0.0029	10,15
450	B,37.99	0.0778	0.9645	0.0027	10,15	450	B,37.99	0.0778	0.9677	0.0028	10,15
450	B,38.50	0.0796	0.9659	0.0020	10,15	450	B,39.00	0.0815	0.9658	0.0020	10,15
450	B,39.49	0.0832	0.9688	0.0025	10,15	450	B,39.49	0.0832	0.9621	0.0068	10,15
450	B,39.49	0.0832	0.9650	0.0025	10,15	450	B,40.00	0.0851	0.9659	0.0025	10,15
450	B,40.00	0.0851	0.9682	0.0025	10,15	450	B,40.50	0.0870	0.9693	0.0025	10,15
450	B,40.50	0.0870	0.9688	0.0025	10,15	450	B,41.01	0.0888	0.9674	0.0025	10,15
450	B,41.01	0.0888	0.9669	0.0025	10,15	450	B,41.49	0.0906	0.9677	0.0025	10,15
450	B,41.49	0.0906	0.9651	0.0025	10,15	450	B,42.00	0.0925	0.9685	0.0025	10,15
450	B,42.00	0.0925	0.9674	0.0025	10,15	450	B,42.50	0.0944	0.9678	0.0023	10,15
450	B,42.50	0.0944	0.9689	0.0023	10,15	450	B,43.00	0.0963	0.9680	0.0026	10,15
450	B,43.00	0.0963	0.9660	0.0026	10,15	450	B,43.50	0.0982	0.9656	0.0026	10,15
450	B,43.50	0.0982	0.9648	0.0026	10,15	450	B,44.00	0.1001	0.9650	0.0025	10,15
450	B,44.00	0.1001	0.9682	0.0026	10,15	450	B,44.51	0.1021	0.9651	0.0026	10,15
450	B,44.51	0.1021	0.9672	0.0026	10,15	450	B,45.00	0.1039	0.9672	0.0026	10,15
450	B,45.00	0.1039	0.9699	0.0026	10,15	450	B,45.50	0.1059	0.9670	0.0024	10,15
450	B,45.50	0.1059	0.9699	0.0024	10,15	450	B,46.01	0.1078	0.9679	0.0024	10,15
450	B,46.01	0.1078	0.9684	0.0024	10,15	450	B,46.50	0.1097	0.9681	0.0024	10,15
450	B,46.50	0.1097	0.9660	0.0024	10,15	450	B,47.00	0.1117	0.9667	0.0024	10,15
450	B,47.00	0.1117	0.9653	0.0024	10,15	450	B,47.51	0.1137	0.9635	0.0025	10,15
450	B,47.51	0.1137	0.9640	0.0025	10,15	450	B,48.00	0.1156	0.9659	0.0029	10,15
450	B,48.00	0.1156	0.9627	0.0029	10,15	450	B,48.50	0.1175	0.9624	0.0029	10,15
450	B,48.50	0.1175	0.9610	0.0029	10,15	450	C,73.01	0.2127	0.9653	0.0041	12,15
450	C,73.01	0.2127	0.9648	0.0039	12,15	450	C,75.49	0.2219	0.9597	0.0034	12,15
450	C,75.49	0.2219	0.9628	0.0034	12,15	450	C,75.49	0.2219	0.9616	0.0032	12,15
450	C,75.49	0.2219	0.9573	0.0031	12,15	450	C,77.98	0.2313	0.9607	0.0031	12,15
450	C,77.98	0.2313	0.9586	0.0031	12,15	450	C,80.49	0.2403	0.9593	0.0031	12,15
450	C,80.49	0.2403	0.9648	0.0032	12,15	450	C,83.02	0.2493	0.9600	0.0024	12,15
450	C,85.51	0.2578	0.9657	0.0024	12,15	450	C,88.01	0.2663	0.9666	0.0032	12,15
450	C,88.01	0.2663	0.9635	0.0086	12,15	450	C,88.01	0.2663	0.9614	0.0031	12,15
450	C,90.50	0.2744	0.9699	0.0032	12,15	450	C,90.50	0.2744	0.9729	0.0032	12,15
450	C,93.00	0.2825	0.9705	0.0032	12,15	450	C,95.49	0.2901	0.9738	0.0033	12,15
450	C,95.49	0.2901	0.9750	0.0033	12,15	450	C,98.01	0.2977	0.9734	0.0034	12,15
450	C,98.01	0.2977	0.9751	0.0034	12,15	450	C,100.50	0.3049	0.9788	0.0034	12,15
450	C,100.50	0.3049	0.9828	0.0035	12,15	450	C,103.00	0.3119	0.9780	0.0032	12,15
450	C,103.00	0.3119	0.9843	0.0032	12,15	450	C,105.54	0.3187	0.9885	0.0036	12,15
450	C,105.54	0.3187	0.9871	0.0036	12,15	450	C,108.04	0.3253	0.9852	0.0042	12,15
450	C,108.04	0.3253	0.9865	0.0036	12,15	450	C,110.53	0.3315	0.9881	0.0036	12,15
450	C,110.53	0.3315	0.9868	0.0037	12,15	450	C,113.06	0.3376	0.9887	0.0038	12,15
450	C,113.06	0.3376	0.9879	0.0038	12,15	450	C,115.56	0.3433	0.9946	0.0038	12,15
450	C,115.56	0.3433	0.9978	0.0039	12,15	450	C,117.94	0.3486	0.9955	0.0036	12,15
450	C,117.94	0.3486	0.9971	0.0036	12,15	450	C,120.49	0.3539	0.9972	0.0037	12,15
450	C,120.49	0.3539	1.0038	0.0037	12,15	450	C,123.08	0.3592	0.9977	0.0037	12,15
450	C,123.08	0.3591	1.0016	0.0037	12,15	450	C,125.41	0.3636	1.0047	0.0037	12,15
450	C,125.41	0.3636	1.0053	0.0037	12,15	450	C,128.02	0.3684	0.9995	0.0037	12,15
450	C,128.02	0.3684	1.0009	0.0038	12,15	450	C,130.55	0.3727	1.0099	0.0044	12,15
450	C,130.55	0.3727	1.0011	0.0044	12,15	450	C,132.95	0.3766	1.0018	0.0045	12,15
450	C,132.95	0.3767	1.0014	0.0044	12,15	585	A,25.51	0.0590	0.9817	0.0079	18
585	A,25.51	0.0590	0.9742	0.0073	18	585	A,25.51	0.0590	0.9750	0.0072	18
585	A,25.51	0.0590	0.9716	0.0064	18	585	A,25.51	0.0590	0.9629	0.0064	18
585	A,25.51	0.0590	0.9688	0.0059	18	585	A,25.51	0.0590	0.9711	0.0064	18
585	A,25.51	0.0590	0.9744	0.0072	18	585	A,25.51	0.0590	0.9736	0.0073	18
585	A,25.51	0.0590	0.9592	0.0069	18	585	A,25.51	0.0590	0.9665	0.0071	18
585	A,25.51	0.0590	0.9688	0.0072	18	585	A,28.01	0.0707	0.9660	0.0052	18
585	A,28.01	0.0707	0.9678	0.0052	18	585	A,28.01	0.0707	0.9697	0.0052	18

E_{Beam} [MeV]	Spec., θ [°]	Q^2_{avg} [$\frac{\text{GeV}^2}{\text{c}^2}$]	$\frac{\sigma_{\text{exp}}}{\sigma_{\text{dip}}}$	$\Delta\frac{\sigma_{\text{exp}}}{\sigma_{\text{dip}}}$	N	E_{Beam} [MeV]	Spec., θ [°]	Q^2_{avg} [$\frac{\text{GeV}^2}{\text{c}^2}$]	$\frac{\sigma_{\text{exp}}}{\sigma_{\text{dip}}}$	$\Delta\frac{\sigma_{\text{exp}}}{\sigma_{\text{dip}}}$	N
585	A,28.01	0.0707	0.9716	0.0052	18	585	A,28.01	0.0707	0.9643	0.0052	18
585	A,28.01	0.0707	0.9665	0.0052	18	585	A,28.01	0.0707	0.9672	0.0052	18
585	A,28.01	0.0707	0.9614	0.0052	18	585	A,28.01	0.0707	0.9567	0.0051	18
585	A,28.01	0.0707	0.9649	0.0052	18	585	A,30.50	0.0831	0.9691	0.0040	18
585	A,30.50	0.0831	0.9650	0.0040	18	585	A,30.50	0.0831	0.9696	0.0033	18
585	A,33.01	0.0964	0.9689	0.0030	18	585	A,33.01	0.0964	0.9687	0.0025	18
585	A,33.01	0.0964	0.9631	0.0045	19	585	A,33.01	0.0964	0.9647	0.0045	19
585	A,33.01	0.0964	0.9743	0.0046	19	585	A,33.01	0.0964	0.9622	0.0046	19
585	A,33.01	0.0964	0.9678	0.0045	19	585	A,33.01	0.0964	0.9707	0.0045	19
585	A,33.01	0.0964	0.9719	0.0045	19	585	A,33.01	0.0964	0.9694	0.0045	19
585	A,35.51	0.1100	0.9708	0.0037	19	585	A,35.51	0.1100	0.9650	0.0037	19
585	A,35.51	0.1100	0.9605	0.0036	19	585	A,38.00	0.1241	0.9672	0.0031	19
585	A,38.00	0.1241	0.9650	0.0030	19	585	A,40.51	0.1387	0.9674	0.0027	19
585	A,40.51	0.1387	0.9641	0.0026	19	585	A,42.99	0.1535	0.9633	0.0023	19
585	A,45.51	0.1688	0.9635	0.0021	19	585	A,48.01	0.1840	0.9591	0.0021	19
585	A,50.49	0.1992	0.9634	0.0022	19	585	A,53.01	0.2148	0.9587	0.0021	19
585	A,55.50	0.2301	0.9594	0.0022	19	585	A,58.00	0.2456	0.9604	0.0023	19
585	A,60.51	0.2608	0.9638	0.0023	19	585	A,63.00	0.2759	0.9639	0.0024	19
585	A,65.49	0.2905	0.9628	0.0024	19	585	A,68.01	0.3054	0.9662	0.0025	19
585	A,70.50	0.3195	0.9686	0.0026	19	585	A,73.01	0.3338	0.9731	0.0028	19
585	A,75.50	0.3473	0.9702	0.0028	19	585	A,78.00	0.3609	0.9765	0.0029	19
585	A,80.51	0.3738	0.9779	0.0030	19	585	A,80.51	0.3738	0.9766	0.0021	19
585	A,82.99	0.3866	0.9833	0.0022	19	585	A,85.49	0.3987	0.9814	0.0022	19
585	A,88.01	0.4108	0.9881	0.0023	19	585	A,90.50	0.4222	0.9942	0.0023	19
585	A,73.01	0.3338	0.9730	0.0014	19	585	B,16.00	0.0255	0.9881	0.0073	16,18
585	B,16.51	0.0272	0.9742	0.0080	16,18	585	B,16.51	0.0272	0.9714	0.0079	16,18
585	B,17.01	0.0288	0.9846	0.0081	16,18	585	B,17.01	0.0288	0.9876	0.0081	16,18
585	B,17.50	0.0304	0.9773	0.0080	16,18	585	B,17.50	0.0304	0.9784	0.0081	16,18
585	B,18.00	0.0322	0.9847	0.0086	16,18	585	B,18.00	0.0322	0.9774	0.0085	16,18
585	B,18.00	0.0322	0.9762	0.0085	16,18	585	B,18.51	0.0340	0.9780	0.0083	16,18
585	B,18.51	0.0340	0.9812	0.0083	16,18	585	B,18.51	0.0340	0.9752	0.0082	16,18
585	B,18.51	0.0340	0.9767	0.0073	16,18	585	B,18.51	0.0340	0.9881	0.0075	16,18
585	B,18.51	0.0340	0.9804	0.0069	16,18	585	B,18.51	0.0340	0.9830	0.0069	16,18
585	B,18.51	0.0340	0.9797	0.0061	16,18	585	B,18.99	0.0357	0.9757	0.0061	16,18
585	B,18.99	0.0357	0.9769	0.0057	16,18	585	B,19.50	0.0376	0.9788	0.0062	16,18
585	B,19.99	0.0394	0.9849	0.0070	16,18	585	B,19.99	0.0394	0.9801	0.0070	16,18
585	B,19.99	0.0394	0.9684	0.0067	16,18	585	B,19.99	0.0394	0.9731	0.0069	16,18
585	B,19.99	0.0394	0.9766	0.0069	16,18	585	B,19.99	0.0394	0.9729	0.0051	16,18
585	B,19.99	0.0394	0.9816	0.0052	16,18	585	B,19.99	0.0394	0.9760	0.0051	16,18
585	B,19.99	0.0394	0.9769	0.0052	16,18	585	B,20.49	0.0413	0.9763	0.0052	16,18
585	B,20.49	0.0413	0.9741	0.0052	16,18	585	B,21.00	0.0433	0.9752	0.0053	16,18
585	B,21.00	0.0433	0.9692	0.0053	16,18	585	B,21.00	0.0433	0.9664	0.0052	16,18
585	B,21.00	0.0433	0.9741	0.0053	16,18	585	B,21.00	0.0433	0.9820	0.0043	16,18
585	B,21.00	0.0433	0.9746	0.0043	16,18	585	B,21.00	0.0433	0.9773	0.0037	16,18
585	B,21.00	0.0433	0.9791	0.0034	16,18	585	B,21.00	0.0433	0.9782	0.0030	16,18
585	B,21.00	0.0433	0.9671	0.0041	16,19	585	B,21.50	0.0453	0.9698	0.0041	16,19
585	B,22.00	0.0473	0.9770	0.0042	16,19	585	B,22.50	0.0494	0.9619	0.0041	16,19
585	B,23.01	0.0515	0.9705	0.0042	16,19	585	B,23.51	0.0537	0.9744	0.0042	16,19
585	B,23.99	0.0557	0.9740	0.0042	16,19	585	B,23.99	0.0557	0.9706	0.0042	16,19
585	B,23.99	0.0557	0.9728	0.0034	16,19	585	B,24.50	0.0580	0.9704	0.0034	16,19
585	B,24.99	0.0602	0.9674	0.0034	16,19	585	B,24.99	0.0602	0.9734	0.0028	16,19
585	B,25.50	0.0625	0.9714	0.0028	16,19	585	B,25.50	0.0625	0.9796	0.0025	16,19
585	B,25.50	0.0625	0.9718	0.0024	16,19	585	B,26.00	0.0648	0.9734	0.0021	16,19
585	B,26.00	0.0648	0.9737	0.0019	16,19	585	B,26.51	0.0672	0.9689	0.0019	16,19
585	B,27.00	0.0695	0.9705	0.0019	16,19	585	B,27.49	0.0718	0.9687	0.0018	16,19
585	B,28.00	0.0743	0.9672	0.0019	16,19	585	B,28.50	0.0768	0.9640	0.0020	16,19
585	B,29.01	0.0793	0.9675	0.0020	16,19	585	B,29.51	0.0818	0.9689	0.0020	16,19
585	B,29.99	0.0842	0.9670	0.0020	16,19	585	B,30.50	0.0868	0.9633	0.0020	16,19
585	B,31.00	0.0894	0.9653	0.0021	16,19	585	B,31.49	0.0920	0.9646	0.0022	16,19
585	B,32.00	0.0946	0.9618	0.0022	16,19	585	B,32.51	0.0974	0.9673	0.0023	16,19
585	B,32.99	0.1000	0.9662	0.0023	16,19	585	B,33.49	0.1027	0.9641	0.0020	16,19
585	B,33.99	0.1054	0.9655	0.0021	16,19	585	B,34.51	0.1082	0.9646	0.0021	16,19
585	B,35.00	0.1110	0.9636	0.0022	16,19	585	B,35.00	0.1110	0.9670	0.0023	16,19
585	B,35.00	0.1110	0.9626	0.0022	16,19	585	B,35.00	0.1110	0.9651	0.0022	16,19
585	B,35.00	0.1110	0.9615	0.0022	16,19	585	B,35.00	0.1110	0.9658	0.0023	16,19
585	B,35.00	0.1110	0.9583	0.0022	16,19	585	B,35.00	0.1110	0.9654	0.0022	16,19
585	B,35.00	0.1109	0.9631	0.0022	16,19	585	B,35.00	0.1110	0.9606	0.0042	16,19
585	B,35.00	0.1110	0.9644	0.0021	16,19	585	B,35.00	0.1110	0.9663	0.0022	16,19
585	B,35.00	0.1110	0.9649	0.0019	16,19	585	B,31.49	0.0920	0.9605	0.0023	16,20
585	B,35.00	0.1110	0.9610	0.0020	16,20	585	B,35.50	0.1137	0.9632	0.0013	16,20
585	B,36.50	0.1194	0.9609	0.0012	16,20	585	B,37.50	0.1251	0.9647	0.0012	16,20
585	B,38.50	0.1308	0.9630	0.0012	16,20	585	B,39.51	0.1367	0.9619	0.0012	16,20
585	B,40.50	0.1425	0.9642	0.0012	16,20	585	B,41.50	0.1484	0.9625	0.0054	16,20
585	B,41.50	0.1484	0.9597	0.0012	16,20	585	B,42.00	0.1513	0.9611	0.0016	16,20
585	B,42.50	0.1543	0.9618	0.0016	16,20	585	B,43.00	0.1573	0.9621	0.0015	16,20
585	B,43.50	0.1603	0.9618	0.0015	16,20	585	B,44.01	0.1633	0.9629	0.0015	16,20
585	B,44.51	0.1663	0.9612	0.0016	16,20	585	B,45.00	0.1693	0.9574	0.0016	16,20
585	B,45.50	0.1723	0.9627	0.0016	16,20	585	B,46.01	0.1754	0.9623	0.0017	16,20
585	B,46.51	0.1785	0.9619	0.0016	16,20	585	B,47.01	0.1815	0.9572	0.0016	16,20
585	C,73.01	0.3340	0.9761	0.0040	17,20	585	C,73.01	0.3340	0.9762	0.0021	17,20
585	C,77.98	0.3610	0.9813	0.0022	17,20	585	C,83.02	0.3870	0.9813	0.0023	17,20

E_{Beam} [MeV]	Spec., θ [°]	Q^2_{avg} [$\frac{\text{GeV}^2}{\text{c}^2}$]	$\frac{\sigma_{\text{exp}}}{\sigma_{\text{dip}}}$	$\Delta\frac{\sigma_{\text{exp}}}{\sigma_{\text{dip}}}$	N	E_{Beam} [MeV]	Spec., θ [°]	Q^2_{avg} [$\frac{\text{GeV}^2}{\text{c}^2}$]	$\frac{\sigma_{\text{exp}}}{\sigma_{\text{dip}}}$	$\Delta\frac{\sigma_{\text{exp}}}{\sigma_{\text{dip}}}$	N
585	C,93.00	0.4338	0.9977	0.0026	17,20	585	C,98.01	0.4549	1.0057	0.0028	17,20
585	C,103.00	0.4745	1.0111	0.0029	17,20	585	C,108.04	0.4927	1.0195	0.0131	17,20
585	C,108.04	0.4927	1.0168	0.0029	17,20	585	C,110.51	0.5009	1.0221	0.0036	17,20
585	C,112.92	0.5089	1.0227	0.0038	17,20	585	C,115.56	0.5170	1.0315	0.0036	17,20
585	C,117.94	0.5241	1.0285	0.0037	17,20	585	C,120.49	0.5312	1.0348	0.0037	17,20
585	C,123.08	0.5382	1.0311	0.0038	17,20	585	C,125.47	0.5442	1.0378	0.0039	17,20
585	C,128.02	0.5504	1.0440	0.0040	17,20	585	C,130.55	0.5561	1.0500	0.0041	17,20
585	C,132.95	0.5613	1.0475	0.0041	17,20	585	C,135.53	0.5665	1.0450	0.0041	17,20
720	A,38.00	0.1835	0.9582	0.0036	25	720	A,38.00	0.1835	0.9521	0.0033	25
720	A,38.00	0.1835	0.9507	0.0034	25	720	A,40.50	0.2045	0.9480	0.0030	25
720	A,40.50	0.2045	0.9478	0.0027	25	720	A,40.50	0.2044	0.9526	0.0030	25
720	A,43.00	0.2258	0.9580	0.0066	25	720	A,43.00	0.2258	0.9530	0.0027	25
720	A,43.00	0.2258	0.9517	0.0059	25	720	A,43.00	0.2258	0.9559	0.0036	25
720	A,43.00	0.2258	0.9526	0.0027	25	720	A,45.51	0.2470	0.9569	0.0028	25
720	A,48.00	0.2686	0.9612	0.0026	25	720	A,50.50	0.2900	0.9644	0.0027	25
720	A,53.01	0.3120	0.9662	0.0027	25	720	A,55.50	0.3332	0.9700	0.0028	25
720	A,58.00	0.3543	0.9695	0.0029	25	720	A,60.50	0.3749	0.9681	0.0030	25
720	A,63.00	0.3954	0.9803	0.0027	25	720	A,65.51	0.4154	0.9821	0.0056	25
720	A,65.51	0.4154	0.9816	0.0028	25	720	A,68.01	0.4351	0.9918	0.0029	25
720	A,70.49	0.4540	0.9913	0.0030	25	720	A,73.01	0.4729	0.9977	0.0031	25
720	A,75.50	0.4908	1.0055	0.0071	25	720	A,75.50	0.4908	1.0001	0.0038	25
720	A,78.00	0.5085	1.0048	0.0028	25	720	A,80.50	0.5254	1.0071	0.0030	25
720	A,83.00	0.5419	1.0142	0.0032	25	720	A,88.01	0.5732	1.0237	0.0039	25
720	A,85.51	0.5578	1.0155	0.0038	25	720	A,90.50	0.5878	1.0224	0.0034	25
720	A,93.01	0.6022	1.0330	0.0036	25	720	A,95.50	0.6157	1.0287	0.0037	25
720	A,97.99	0.6288	1.0404	0.0048	25	720	A,97.99	0.6288	1.0412	0.0048	25
720	A,100.50	0.6414	1.0367	0.0056	25	720	A,100.50	0.6414	1.0374	0.0049	25
720	A,103.00	0.6536	1.0483	0.0051	25	720	A,103.00	0.6536	1.0506	0.0052	25
720	A,105.51	0.6651	1.0490	0.0065	25	720	A,105.51	0.6651	1.0450	0.0047	25
720	A,105.51	0.6651	1.0487	0.0046	25	720	A,108.00	0.6761	1.0510	0.0049	25
720	A,108.00	0.6761	1.0480	0.0049	25	720	A,73.01	0.4729	0.9979	0.0029	25
720	B,22.00	0.0711	0.9666	0.0042	21,25	720	B,22.50	0.0742	0.9644	0.0040	21,25
720	B,23.00	0.0773	0.9603	0.0040	21,25	720	B,23.00	0.0773	0.9600	0.0035	21,25
720	B,23.51	0.0805	0.9652	0.0032	21,25	720	B,24.00	0.0837	0.9615	0.0035	21,25
720	B,24.00	0.0837	0.9678	0.0077	21,25	720	B,24.00	0.0837	0.9622	0.0032	21,25
720	B,24.50	0.0870	0.9670	0.0042	21,25	720	B,25.01	0.0903	0.9652	0.0032	21,25
720	B,25.01	0.0903	0.9663	0.0032	21,25	720	B,25.50	0.0936	0.9615	0.0030	21,25
720	B,26.00	0.0970	0.9679	0.0030	21,25	720	B,26.51	0.1005	0.9656	0.0030	21,25
720	B,27.00	0.1039	0.9662	0.0030	21,25	720	B,27.50	0.1074	0.9586	0.0031	21,25
720	B,28.00	0.1110	0.9580	0.0031	21,25	720	B,28.50	0.1146	0.9636	0.0028	21,25
720	B,29.00	0.1182	0.9594	0.0054	21,25	720	B,29.00	0.1182	0.9634	0.0028	21,25
720	B,29.51	0.1219	0.9661	0.0028	21,25	720	B,29.99	0.1255	0.9616	0.0029	21,25
720	B,30.50	0.1294	0.9625	0.0030	21,25	720	B,31.00	0.1331	0.9662	0.0060	21,25
720	B,31.00	0.1331	0.9599	0.0034	21,25	720	B,31.51	0.1369	0.9632	0.0026	21,25
720	B,32.01	0.1408	0.9615	0.0027	21,25	720	B,32.51	0.1446	0.9635	0.0028	21,25
720	B,33.50	0.1524	0.9605	0.0034	21,25	720	B,33.01	0.1485	0.9614	0.0033	21,25
720	B,34.01	0.1564	0.9630	0.0031	21,25	720	B,34.01	0.1564	0.9604	0.0032	21,25
720	B,34.01	0.1564	0.9595	0.0032	21,25	720	B,34.01	0.1564	0.9617	0.0040	21,25
720	B,34.01	0.1564	0.9651	0.0040	21,25	720	B,34.01	0.1564	0.9630	0.0044	21,25
720	B,34.01	0.1564	0.9644	0.0040	21,25	720	B,34.01	0.1564	0.9627	0.0040	21,25
720	B,34.01	0.1564	0.9620	0.0040	21,25	720	B,34.01	0.1564	0.9630	0.0046	21,25
720	B,34.01	0.1564	0.9657	0.0036	21,25	720	B,34.01	0.1564	0.9620	0.0036	21,25
720	B,34.01	0.1564	0.9637	0.0036	21,25	720	B,34.01	0.1564	0.9615	0.0036	21,25
720	B,34.01	0.1564	0.9587	0.0036	21,25	720	B,34.01	0.1564	0.9589	0.0036	21,25
720	B,34.01	0.1564	0.9658	0.0036	21,25	720	B,30.50	0.1294	0.9592	0.0032	21,26
720	B,34.01	0.1564	0.9622	0.0038	21,26	720	B,34.01	0.1564	0.9628	0.0035	21,26
720	B,34.51	0.1604	0.9635	0.0031	21,26	720	B,35.00	0.1643	0.9627	0.0030	21,26
720	B,35.50	0.1683	0.9578	0.0030	21,26	720	B,36.00	0.1723	0.9537	0.0025	21,26
720	B,36.50	0.1764	0.9618	0.0025	21,26	720	B,37.00	0.1805	0.9637	0.0025	21,26
720	B,37.50	0.1846	0.9663	0.0031	21,26	720	B,38.01	0.1888	0.9640	0.0031	21,26
720	B,38.50	0.1928	0.9650	0.0032	21,26	720	B,39.00	0.1970	0.9594	0.0032	21,26
720	B,39.49	0.2011	0.9552	0.0032	21,26	720	B,40.00	0.2053	0.9580	0.0027	21,26
720	B,40.00	0.2053	0.9422	0.0088	21,26	720	B,40.00	0.2053	0.9559	0.0043	21,26
720	B,40.00	0.2053	0.9547	0.0066	21,26	720	B,40.00	0.2053	0.9585	0.0047	21,26
720	B,40.50	0.2095	0.9550	0.0033	21,26	720	B,40.50	0.2095	0.9576	0.0057	21,26
720	B,40.50	0.2095	0.9610	0.0048	21,26	720	B,40.50	0.2095	0.9554	0.0066	21,26
720	B,41.50	0.2179	0.9602	0.0034	21,26	720	B,41.50	0.2179	0.9406	0.0098	21,26
720	B,41.50	0.2179	0.9601	0.0050	21,26	720	B,41.50	0.2179	0.9541	0.0047	21,26
720	B,42.50	0.2264	0.9511	0.0031	21,26	720	B,42.50	0.2264	0.9543	0.0032	21,26
720	B,42.50	0.2264	0.9491	0.0130	21,26	720	B,42.50	0.2264	0.9447	0.0097	21,26
720	B,42.50	0.2264	0.9510	0.0040	21,26	720	B,43.50	0.2349	0.9562	0.0032	21,26
720	B,43.50	0.2349	0.9611	0.0052	21,26	720	B,43.50	0.2349	0.9525	0.0040	21,26
720	B,44.51	0.2435	0.9519	0.0031	21,26	720	B,39.49	0.2011	0.9559	0.0026	23,26
720	B,39.49	0.2011	0.9572	0.0024	23,26	720	B,40.00	0.2052	0.9553	0.0026	23,26
720	B,40.00	0.2052	0.9551	0.0046	23,26	720	B,40.50	0.2094	0.9597	0.0026	23,26
720	B,41.01	0.2137	0.9612	0.0025	23,26	720	B,41.01	0.2137	0.9586	0.0025	23,26
720	B,41.50	0.2178	0.9562	0.0026	23,26	720	B,41.50	0.2178	0.9574	0.0026	23,26
720	B,42.00	0.2222	0.9582	0.0026	23,26	720	B,42.00	0.2222	0.9579	0.0034	23,26
720	B,42.00	0.2222	0.9521	0.0037	23,26	720	B,42.50	0.2264	0.9626	0.0031	23,26
720	B,42.50	0.2264	0.9593	0.0027	23,26	720	B,43.00	0.2307	0.9603	0.0032	23,26
720	B,43.00	0.2307	0.9626	0.0042	23,26	720	B,43.00	0.2307	0.9610	0.0027	23,26

E_{Beam} [MeV]	Spec., θ [°]	Q^2_{avg} [$\frac{\text{GeV}^2}{\text{c}^2}$]	$\frac{\sigma_{\text{exp}}}{\sigma_{\text{dip}}}$	$\Delta\frac{\sigma_{\text{exp}}}{\sigma_{\text{dip}}}$	N	E_{Beam} [MeV]	Spec., θ [°]	Q^2_{avg} [$\frac{\text{GeV}^2}{\text{c}^2}$]	$\frac{\sigma_{\text{exp}}}{\sigma_{\text{dip}}}$	$\Delta\frac{\sigma_{\text{exp}}}{\sigma_{\text{dip}}}$	N
720	B,43.50	0.2348	0.9574	0.0027	23,26	720	B,43.50	0.2348	0.9535	0.0027	23,26
720	B,43.98	0.2390	0.9556	0.0027	23,26	720	B,43.98	0.2390	0.9553	0.0035	23,26
720	B,43.98	0.2390	0.9590	0.0034	23,26	720	B,44.49	0.2433	0.9539	0.0025	23,26
720	B,44.49	0.2433	0.9537	0.0025	23,26	720	B,45.00	0.2477	0.9588	0.0025	23,26
720	B,45.50	0.2520	0.9559	0.0025	23,26	720	B,45.50	0.2520	0.9594	0.0026	23,26
720	C,73.01	0.4729	0.9969	0.0024	22,26	720	C,73.01	0.4729	0.9967	0.0021	22,26
720	C,75.49	0.4908	0.9994	0.0022	22,26	720	C,77.98	0.5083	1.0018	0.0023	22,26
720	C,80.49	0.5253	1.0023	0.0023	22,26	720	C,83.02	0.5420	1.0178	0.0024	22,26
720	C,85.51	0.5579	1.0140	0.0020	22,26	720	C,88.01	0.5732	1.0171	0.0021	22,26
720	C,90.50	0.5879	1.0149	0.0139	22,26	720	C,90.50	0.5879	1.0248	0.0022	22,26
720	C,93.00	0.6022	1.0335	0.0217	22,26	720	C,93.00	0.6022	1.0284	0.0028	22,26
720	C,95.48	0.6157	1.0271	0.0029	22,26	720	C,98.01	0.6290	1.0417	0.0030	22,26
720	C,100.50	0.6415	1.0307	0.0031	22,26	720	C,103.00	0.6536	1.0395	0.0033	22,26
720	C,105.54	0.6652	1.0409	0.0028	22,26	720	C,105.54	0.6652	1.0472	0.0093	22,26
720	C,105.54	0.6653	1.0448	0.0045	22,26	720	C,105.54	0.6652	1.0442	0.0069	22,26
720	C,105.54	0.6652	1.0488	0.0049	22,26	720	C,108.04	0.6763	1.0492	0.0036	22,26
720	C,108.04	0.6763	1.0479	0.0062	22,26	720	C,108.04	0.6763	1.0522	0.0052	22,26
720	C,108.04	0.6763	1.0545	0.0071	22,26	720	C,113.06	0.6969	1.0557	0.0039	22,26
720	C,113.06	0.6969	1.0545	0.0115	22,26	720	C,113.06	0.6969	1.0645	0.0058	22,26
720	C,113.06	0.6969	1.0649	0.0055	22,26	720	C,117.94	0.7151	1.0587	0.0037	22,26
720	C,117.94	0.7151	1.0663	0.0039	22,26	720	C,117.94	0.7151	1.0789	0.0121	22,26
720	C,117.94	0.7151	1.0505	0.0048	22,26	720	C,123.08	0.7325	1.0727	0.0040	22,26
720	C,123.08	0.7325	1.0707	0.0065	22,26	720	C,123.08	0.7325	1.0735	0.0051	22,26
720	C,128.02	0.7474	1.0733	0.0040	22,26	720	C,103.00	0.6536	1.0350	0.0025	24,26
720	C,103.00	0.6536	1.0378	0.0023	24,26	720	C,105.54	0.6652	1.0400	0.0025	24,26
720	C,105.54	0.6652	1.0413	0.0045	24,26	720	C,108.04	0.6764	1.0468	0.0026	24,26
720	C,108.04	0.6764	1.0491	0.0026	24,26	720	C,110.53	0.6867	1.0510	0.0025	24,26
720	C,110.53	0.6867	1.0462	0.0025	24,26	720	C,113.06	0.6970	1.0491	0.0026	24,26
720	C,113.06	0.6970	1.0507	0.0026	24,26	720	C,115.56	0.7064	1.0600	0.0027	24,26
720	C,115.56	0.7064	1.0558	0.0036	24,26	720	C,115.56	0.7064	1.0564	0.0038	24,26
720	C,117.94	0.7152	1.0599	0.0033	24,26	720	C,117.94	0.7152	1.0582	0.0028	24,26
720	C,120.49	0.7239	1.0703	0.0034	24,26	720	C,120.49	0.7239	1.0608	0.0044	24,26
720	C,120.49	0.7239	1.0710	0.0029	24,26	720	C,123.08	0.7325	1.0700	0.0030	24,26
720	C,123.08	0.7324	1.0666	0.0030	24,26	720	C,125.59	0.7402	1.0715	0.0030	24,26
720	C,125.59	0.7402	1.0784	0.0040	24,26	720	C,125.59	0.7402	1.0728	0.0039	24,26
720	C,128.02	0.7474	1.0728	0.0028	24,26	720	C,128.02	0.7474	1.0726	0.0028	24,26
720	C,130.65	0.7546	1.0846	0.0029	24,26	720	C,132.84	0.7603	1.0818	0.0029	24,26
720	C,132.84	0.7603	1.0737	0.0029	24,26	855	A,43.00	0.3069	0.9515	0.0044	29,30
855	A,43.00	0.3069	0.9646	0.0044	29,30	855	A,43.00	0.3069	0.9647	0.0044	29,30
855	A,43.00	0.3069	0.9670	0.0046	29,30	855	A,43.00	0.3069	0.9561	0.0045	29,30
855	A,45.51	0.3354	0.9589	0.0045	29,30	855	A,45.51	0.3354	0.9547	0.0045	29,30
855	A,45.51	0.3354	0.9597	0.0045	29,30	855	A,45.51	0.3354	0.9620	0.0045	29,30
855	A,45.51	0.3354	0.9576	0.0045	29,30	855	A,48.00	0.3639	0.9602	0.0046	29,30
855	A,48.00	0.3639	0.9677	0.0046	29,30	855	A,48.00	0.3638	0.9701	0.0046	29,30
855	A,48.00	0.3639	0.9692	0.0046	29,30	855	A,48.00	0.3638	0.9658	0.0046	29,30
855	A,50.50	0.3917	0.9695	0.0046	29,30	855	A,50.50	0.3917	0.9673	0.0045	29,30
855	A,50.50	0.3916	0.9665	0.0045	29,30	855	A,50.50	0.3916	0.9723	0.0046	29,30
855	A,50.50	0.3916	0.9734	0.0046	29,30	855	A,53.01	0.4201	0.9776	0.0046	29,30
855	A,53.01	0.4201	0.9766	0.0074	29,30	855	A,53.01	0.4201	0.9693	0.0046	29,30
855	A,53.01	0.4201	0.9785	0.0047	29,30	855	A,53.01	0.4201	0.9839	0.0047	29,30
855	A,55.50	0.4471	0.9820	0.0048	29,30	855	A,55.50	0.4471	0.9858	0.0048	29,30
855	A,55.50	0.4471	0.9793	0.0048	29,30	855	A,55.50	0.4471	0.9798	0.0048	29,30
855	A,55.50	0.4471	0.9845	0.0048	29,30	855	A,58.00	0.4748	0.9854	0.0023	29,30
855	A,60.50	0.5011	0.9925	0.0022	29,30	855	A,63.00	0.5274	0.9931	0.0022	29
855	A,65.49	0.5524	1.0022	0.0023	29	855	A,68.00	0.5775	1.0137	0.0024	29
855	A,70.50	0.6011	1.0069	0.0024	29	855	A,73.01	0.6249	1.0167	0.0025	29
855	A,75.50	0.6468	1.0210	0.0034	29	855	A,78.00	0.6690	1.0248	0.0027	29
855	A,80.50	0.6895	1.0167	0.0066	29	855	A,83.01	0.7101	1.0365	0.0024	29
855	A,85.49	0.7290	1.0435	0.0025	29	855	A,88.01	0.7482	1.0492	0.0031	29
855	A,90.50	0.7656	1.0455	0.0028	29	855	A,85.51	0.7295	1.0407	0.0027	29
855	B,20.50	0.0867	0.9444	0.0067	27,29	855	B,21.00	0.0908	0.9594	0.0067	27,29
855	B,21.50	0.0949	0.9586	0.0066	27,29	855	B,22.00	0.0990	0.9622	0.0069	27,29
855	B,22.50	0.1033	0.9507	0.0068	27,29	855	B,22.50	0.1033	0.9477	0.0068	27,29
855	B,23.00	0.1076	0.9468	0.0068	27,29	855	B,23.51	0.1120	0.9543	0.0069	27,29
855	B,23.99	0.1163	0.9493	0.0069	27,29	855	B,24.50	0.1209	0.9445	0.0068	27,29
855	B,24.50	0.1209	0.9458	0.0068	27,29	855	B,25.01	0.1255	0.9517	0.0069	27,29
855	B,25.50	0.1300	0.9540	0.0069	27,29	855	B,26.01	0.1348	0.9587	0.0070	27,29
855	B,26.51	0.1395	0.9555	0.0070	27,29	855	B,26.51	0.1395	0.9516	0.0069	27,29
855	B,26.99	0.1441	0.9470	0.0068	27,29	855	B,27.50	0.1490	0.9485	0.0068	27,29
855	B,28.00	0.1538	0.9562	0.0070	27,29	855	B,28.50	0.1588	0.9553	0.0070	27,29
855	B,28.50	0.1588	0.9532	0.0069	27,29	855	B,29.00	0.1637	0.9517	0.0111	27,29
855	B,29.50	0.1687	0.9551	0.0070	27,29	855	B,30.01	0.1739	0.9618	0.0071	27,29
855	B,30.50	0.1789	0.9595	0.0070	27,29	855	B,30.50	0.1789	0.9597	0.0071	27,29
855	B,31.00	0.1840	0.9657	0.0072	27,29	855	B,31.51	0.1893	0.9576	0.0072	27,29
855	B,32.00	0.1943	0.9576	0.0072	27,29	855	B,32.50	0.1997	0.9536	0.0073	27,29
855	B,32.50	0.1997	0.9547	0.0031	27,29	855	B,33.01	0.2051	0.9583	0.0032	27,29
855	B,33.50	0.2103	0.9530	0.0031	27,29	855	B,34.00	0.2156	0.9549	0.0031	27,29
855	B,34.50	0.2210	0.9621	0.0032	27,29	855	B,35.00	0.2264	0.9561	0.0032	27,29
855	B,35.50	0.2318	0.9583	0.0032	27,29	855	B,36.00	0.2372	0.9521	0.0043	27,29
855	B,36.50	0.2427	0.9539	0.0033	27,29	855	B,37.00	0.2481	0.9448	0.0092	27,29
855	B,37.50	0.2536	0.9601	0.0028	27,29	855	B,38.01	0.2592	0.9617	0.0028	27,29

E_{Beam} [MeV]	Spec., θ [°]	Q^2_{avg} [$\frac{\text{GeV}^2}{\text{c}^2}$]	$\frac{\sigma_{\text{exp}}}{\sigma_{\text{dip}}}$	$\Delta\frac{\sigma_{\text{exp}}}{\sigma_{\text{dip}}}$	N	E_{Beam} [MeV]	Spec., θ [°]	Q^2_{avg} [$\frac{\text{GeV}^2}{\text{c}^2}$]	$\frac{\sigma_{\text{exp}}}{\sigma_{\text{dip}}}$	$\Delta\frac{\sigma_{\text{exp}}}{\sigma_{\text{dip}}}$	N
855	B,38.51	0.2647	0.9626	0.0035	27,29	855	B,39.00	0.2702	0.9598	0.0032	27,29
855	B,39.51	0.2758	0.9616	0.0035	27,29	855	B,40.00	0.2814	0.9584	0.0035	27,29
855	B,42.00	0.3038	0.9624	0.0037	27,29	855	B,42.50	0.3094	0.9692	0.0038	27,29
855	B,42.50	0.3094	0.9628	0.0038	27,29	855	B,43.00	0.3150	0.9644	0.0039	27,29
855	B,43.00	0.3150	0.9663	0.0039	27,29	855	B,43.50	0.3207	0.9725	0.0040	27,29
855	B,43.50	0.3207	0.9681	0.0040	27,29	855	B,44.00	0.3263	0.9611	0.0035	27,29
855	B,44.00	0.3263	0.9563	0.0037	27,31	855	B,44.51	0.3320	0.9659	0.0042	27,31
855	B,45.00	0.3375	0.9611	0.0037	27,31	855	B,45.50	0.3432	0.9651	0.0037	27,31
855	B,46.01	0.3489	0.9646	0.0038	27,31	855	B,46.50	0.3544	0.9698	0.0037	27,31
855	B,47.00	0.3600	0.9626	0.0037	27,31	855	B,47.51	0.3657	0.9714	0.0037	27,31
855	B,48.00	0.3712	0.9654	0.0046	27,31	855	B,48.00	0.3712	0.9665	0.0046	27,31
855	B,48.50	0.3768	0.9653	0.0045	27,31	855	B,48.50	0.3768	0.9672	0.0044	27,31
855	B,49.01	0.3825	0.9651	0.0046	27,31	855	B,49.01	0.3825	0.9719	0.0047	27,31
855	B,49.50	0.3880	0.9630	0.0072	27,31	855	B,49.50	0.3880	0.9683	0.0042	27,31
855	B,50.00	0.3936	0.9690	0.0049	27,31	855	B,50.00	0.3936	0.9734	0.0049	27,31
855	B,50.50	0.3991	0.9798	0.0049	27,31	855	B,50.50	0.3991	0.9715	0.0099	27,31
855	B,51.00	0.4047	0.9744	0.0050	27,31	855	B,51.00	0.4047	0.9750	0.0050	27,31
855	B,51.50	0.4102	0.9820	0.0066	27,31	855	B,52.00	0.4157	0.9764	0.0052	27,31
855	B,52.00	0.4158	0.9753	0.0061	27,31	855	B,52.49	0.4212	0.9797	0.0053	27,31
855	B,52.49	0.4212	0.9706	0.0052	27,31	855	B,53.01	0.4269	0.9754	0.0053	27,31
855	B,53.01	0.4269	0.9611	0.0124	27,31	855	B,53.50	0.4323	0.9694	0.0243	27,31
855	B,53.50	0.4323	0.9778	0.0054	27,31	855	B,53.50	0.4322	0.9809	0.0055	27,31
855	B,53.50	0.4322	0.9783	0.0054	27,31	855	B,54.01	0.4378	0.9734	0.0078	27,31
855	B,54.01	0.4378	0.9727	0.0084	27,31	855	C,85.51	0.7300	1.0293	0.0028	28,31
855	C,88.01	0.7486	1.0391	0.0033	28,31	855	C,90.50	0.7661	1.0401	0.0030	28,31
855	C,93.00	0.7836	1.0481	0.0031	28,31	855	C,95.49	0.7996	1.0530	0.0032	28,31
855	C,98.01	0.8157	1.0601	0.0034	28,31	855	C,100.50	0.8303	1.0673	0.0035	28,31
855	C,103.00	0.8449	1.0639	0.0036	28,31	855	C,105.54	0.8586	1.0678	0.0046	28,31
855	C,105.54	0.8586	1.0822	0.0046	28,31	855	C,108.04	0.8718	1.0791	0.0049	28,31
855	C,108.04	0.8718	1.0880	0.0045	28,31	855	C,110.51	0.8838	1.0891	0.0048	28,31
855	C,110.51	0.8838	1.0939	0.0049	28,31	855	C,113.06	0.8960	1.0895	0.0071	28,31
855	C,115.56	0.9070	1.0993	0.0047	28,31	855	C,115.56	0.9070	1.0895	0.0047	28,31
855	C,117.95	0.9174	1.0999	0.0048	28,31	855	C,120.49	0.9274	1.0979	0.0049	28,31
855	C,120.49	0.9275	1.1002	0.0050	28,31	855	C,123.08	0.9374	1.1159	0.0066	28,31
855	C,125.47	0.9460	1.1186	0.0053	28,31	855	C,125.47	0.9459	1.1020	0.0061	28,31
855	C,128.02	0.9547	1.1173	0.0053	28,31	855	C,128.02	0.9547	1.1102	0.0053	28,31
855	C,130.55	0.9627	1.1198	0.0054	28,31	855	C,132.95	0.9700	1.1161	0.0055	28,31
855	C,132.95	0.9700	1.1232	0.0055	28,31	855	C,132.95	0.9700	1.1212	0.0055	28,31
855	C,135.52	0.9772	1.1313	0.0080	28,31	855	C,135.52	0.9772	1.1347	0.0087	28,31

Table C.2.: New cross sections measured in this work. No Feshbach Coulomb correction and no TPE correction was applied to the data listed here.

E_{Beam} [MeV]	Spec., θ [°]	Q^2_{avg} [$\frac{\mathrm{GeV}^2}{\mathrm{c}^2}$]	$\frac{\sigma_{\mathrm{exp}}}{\sigma_{\mathrm{dip}}}$	$\Delta\frac{\sigma_{\mathrm{exp}}}{\sigma_{\mathrm{dip}}}$	N	E_{Beam} [MeV]	Spec., θ [°]	Q^2_{avg} [$\frac{\mathrm{GeV}^2}{\mathrm{c}^2}$]	$\frac{\sigma_{\mathrm{exp}}}{\sigma_{\mathrm{dip}}}$	$\Delta\frac{\sigma_{\mathrm{exp}}}{\sigma_{\mathrm{dip}}}$	N
720	A,78.00	0.5068	1.0059	0.0022	32	720	A,81.00	0.5272	1.0139	0.0022	32
720	A,84.01	0.5469	1.0154	0.0024	32	720	A,87.01	0.5656	1.0219	0.0023	32
720	A,90.01	0.5836	1.0289	0.0022	32	720	A,93.01	0.6007	1.0242	0.0022	32
720	A,96.01	0.6171	1.0328	0.0023	32	720	A,99.00	0.6327	1.0358	0.0023	32
720	A,102.00	0.6476	1.0409	0.0023	32	720	A,105.00	0.6617	1.0417	0.0023	32
720	A,108.00	0.6751	1.0466	0.0023	32	720	A,111.00	0.6878	1.0507	0.0023	32
720	A,114.00	0.6998	1.0506	0.0023	32	720	A,117.00	0.7111	1.0546	0.0023	32
720	A,120.00	0.7217	1.0592	0.0024	32	855	A,72.00	0.6146	1.0185	0.0023	33
855	A,75.00	0.6418	1.0265	0.0024	33	855	A,75.00	0.6419	1.0212	0.0024	33
855	A,78.00	0.6679	1.0286	0.0025	33	855	A,78.00	0.6680	1.0276	0.0025	33
855	A,81.00	0.6928	1.0328	0.0026	33	855	A,81.00	0.6929	1.0314	0.0026	33
855	A,84.01	0.7168	1.0400	0.0025	33	855	A,84.01	0.7168	1.0359	0.0025	33
855	A,87.01	0.7395	1.0394	0.0025	33	855	A,90.01	0.7613	1.0541	0.0027	33
855	A,93.01	0.7819	1.0506	0.0026	33	855	A,96.01	0.8016	1.0590	0.0027	33
855	A,99.00	0.8201	1.0606	0.0027	33	855	A,102.00	0.8379	1.0697	0.0029	33
855	A,105.00	0.8546	1.0749	0.0030	33	855	A,108.00	0.8705	1.0784	0.0032	33
855	A,111.00	0.8854	1.0808	0.0033	33	855	A,114.00	0.8994	1.0865	0.0035	33
855	A,117.00	0.9127	1.0901	0.0036	33	855	A,120.00	0.9250	1.0838	0.0037	33
1002	A,60.00	0.6428	1.0121	0.0036	34,39	1002	A,60.00	0.6429	1.0111	0.0032	34,39
1002	A,63.00	0.6815	1.0185	0.0026	34,39	1002	A,63.00	0.6815	1.0130	0.0038	34,39
1002	A,75.00	0.8244	1.0563	0.0026	34	1002	A,78.00	0.8556	1.0633	0.0027	34
1002	A,81.00	0.8848	1.0654	0.0028	34	1002	A,81.00	0.8853	1.0603	0.0028	34
1002	A,84.01	0.9134	1.0654	0.0029	34	1002	A,87.01	0.9404	1.0750	0.0031	34
1002	A,90.01	0.9658	1.0812	0.0033	34	1002	A,93.01	0.9901	1.0814	0.0035	34
1002	A,96.01	1.0130	1.0908	0.0037	34	1002	A,99.00	1.0346	1.0949	0.0039	34
1002	A,102.00	1.0552	1.1017	0.0058	34	1002	A,105.00	1.0746	1.0972	0.0042	34
1002	A,108.00	1.0928	1.1087	0.0046	34	1002	A,111.00	1.1100	1.1103	0.0048	34
1002	A,114.00	1.1261	1.1179	0.0051	34	1002	A,117.00	1.1412	1.1206	0.0052	34
1002	A,120.00	1.1553	1.1186	0.0050	34	1002	A,120.00	1.1553	1.1237	0.0052	34
1158	A,66.00	0.9084	1.0562	0.0021	35,39	1158	A,66.00	0.9085	1.0488	0.0021	35,39
1158	A,66.00	0.9089	1.0570	0.0025	35,39	1158	A,69.00	0.9477	1.0591	0.0020	35,39
1158	A,84.01	1.1341	1.1029	0.0029	35	1158	A,84.01	1.1343	1.0995	0.0029	35
1158	A,87.01	1.1653	1.1042	0.0031	35	1158	A,87.01	1.1654	1.1057	0.0031	35
1158	A,90.01	1.1943	1.1087	0.0033	35	1158	A,90.01	1.1946	1.1072	0.0033	35
1158	A,93.01	1.2221	1.1149	0.0035	35	1158	A,93.01	1.2221	1.1132	0.0035	35
1158	A,96.01	1.2481	1.1163	0.0038	35	1158	A,96.01	1.2483	1.1151	0.0038	35
1158	A,96.01	1.2483	1.1169	0.0055	35	1158	A,99.00	1.2726	1.1217	0.0040	35
1158	A,99.00	1.2728	1.1188	0.0040	35	1158	A,99.00	1.2729	1.1165	0.0040	35
1158	A,102.00	1.2960	1.1310	0.0043	35	1158	A,102.00	1.2960	1.1198	0.0043	35
1158	A,102.00	1.2961	1.1208	0.0042	35	1158	A,105.00	1.3178	1.1316	0.0045	35
1158	A,105.00	1.3179	1.1176	0.0045	35	1158	A,105.00	1.3179	1.1230	0.0045	35
1158	A,108.00	1.3382	1.1329	0.0047	35	1158	A,108.00	1.3383	1.1342	0.0047	35
1158	A,108.00	1.3384	1.1375	0.0047	35	1158	A,108.00	1.3385	1.1308	0.0064	35
1158	A,111.00	1.3575	1.1256	0.0050	35	1158	A,111.00	1.3575	1.1380	0.0047	35
1158	A,111.00	1.3577	1.1369	0.0050	35	1158	A,114.00	1.3755	1.1441	0.0051	35
1158	A,114.00	1.3755	1.1343	0.0053	35	1158	A,114.00	1.3756	1.1398	0.0052	35
1158	A,114.00	1.3756	1.1307	0.0052	35	1158	A,117.00	1.3923	1.1386	0.0055	35
1158	A,117.00	1.3924	1.1475	0.0051	35	1158	A,117.00	1.3924	1.1388	0.0051	35
1158	A,117.00	1.3925	1.1485	0.0055	35	1158	A,117.00	1.3925	1.1523	0.0055	35
1158	A,117.00	1.3925	1.1494	0.0055	35	1158	A,120.00	1.4081	1.1444	0.0053	35
1158	A,120.00	1.4081	1.1488	0.0053	35	1158	A,120.00	1.4081	1.1501	0.0057	35
1158	A,120.00	1.4081	1.1488	0.0057	35	1158	A,120.00	1.4081	1.1520	0.0053	35
1158	A,120.00	1.4081	1.1486	0.0057	35	1308	A,72.00	1.1932	1.0911	0.0026	36,39
1308	A,75.00	1.2344	1.0939	0.0028	36,39	1308	A,87.01	1.3899	1.1260	0.0040	36
1308	A,87.01	1.3900	1.1205	0.0040	36	1308	A,87.01	1.3900	1.1195	0.0040	36
1308	A,90.01	1.4225	1.1252	0.0043	36	1308	A,90.01	1.4226	1.1138	0.0043	36
1308	A,90.01	1.4226	1.1299	0.0043	36	1308	A,90.01	1.4228	1.1228	0.0043	36
1308	A,93.01	1.4533	1.1267	0.0046	36	1308	A,93.01	1.4533	1.1391	0.0046	36
1308	A,93.01	1.4533	1.1313	0.0046	36	1308	A,96.01	1.4820	1.1358	0.0050	36
1308	A,96.01	1.4821	1.1350	0.0050	36	1308	A,96.01	1.4822	1.1420	0.0050	36
1308	A,99.00	1.5093	1.1348	0.0053	36	1308	A,99.00	1.5094	1.1363	0.0053	36
1308	A,102.00	1.5348	1.1379	0.0056	36	1308	A,102.00	1.5348	1.1350	0.0056	36
1308	A,102.00	1.5349	1.1371	0.0056	36	1308	A,102.00	1.5349	1.1286	0.0056	36
1308	A,102.00	1.5350	1.1371	0.0056	36	1308	A,105.00	1.5588	1.1394	0.0059	36
1308	A,105.00	1.5588	1.1406	0.0059	36	1308	A,105.00	1.5588	1.1407	0.0059	36
1308	A,105.00	1.5589	1.1280	0.0095	36	1308	A,105.00	1.5589	1.1393	0.0059	36
1308	A,105.00	1.5590	1.1437	0.0060	36	1308	A,105.00	1.5590	1.1354	0.0059	36
1308	A,105.00	1.5590	1.1408	0.0059	36	1308	A,108.00	1.5813	1.1428	0.0063	36
1308	A,108.00	1.5813	1.1342	0.0062	36	1308	A,108.00	1.5813	1.1361	0.0062	36
1308	A,108.00	1.5814	1.1543	0.0063	36	1308	A,111.00	1.6023	1.1444	0.0066	36
1308	A,111.00	1.6023	1.1600	0.0066	36	1308	A,111.00	1.6023	1.1429	0.0066	36
1308	A,111.00	1.6024	1.1414	0.0066	36	1308	A,111.00	1.6024	1.1470	0.0062	36
1308	A,114.00	1.6219	1.1546	0.0069	36	1308	A,114.00	1.6220	1.1455	0.0069	36
1308	A,114.00	1.6220	1.1401	0.0069	36	1308	A,114.00	1.6221	1.1584	0.0069	36
1308	A,114.00	1.6222	1.1533	0.0069	36	1308	A,117.00	1.6403	1.1563	0.0073	36

E_{Beam} [MeV]	Spec., θ [°]	Q^2_{avg} [$\frac{\text{GeV}^2}{\text{c}^2}$]	$\frac{\sigma_{\text{exp}}}{\sigma_{\text{dip}}}$	$\Delta\frac{\sigma_{\text{exp}}}{\sigma_{\text{dip}}}$	N	E_{Beam} [MeV]	Spec., θ [°]	Q^2_{avg} [$\frac{\text{GeV}^2}{\text{c}^2}$]	$\frac{\sigma_{\text{exp}}}{\sigma_{\text{dip}}}$	$\Delta\frac{\sigma_{\text{exp}}}{\sigma_{\text{dip}}}$	N
1308	A,117.00	1.6403	1.1552	0.0073	36	1308	A,117.00	1.6403	1.1513	0.0073	36
1308	A,117.00	1.6403	1.1474	0.0073	36	1308	A,117.00	1.6403	1.1465	0.0072	36
1308	A,117.00	1.6404	1.1569	0.0073	36	1308	A,117.00	1.6404	1.1473	0.0073	36
1308	A,120.00	1.6572	1.1722	0.0128	36	1308	A,120.00	1.6573	1.1453	0.0076	36
1308	A,120.00	1.6574	1.1588	0.0076	36	1308	A,120.00	1.6574	1.1436	0.0075	36
1308	A,120.00	1.6574	1.1534	0.0076	36	1308	A,120.00	1.6575	1.1630	0.0076	36
1308	A,120.00	1.6575	1.1585	0.0076	36	1402	A,75.00	1.3713	1.1129	0.0039	37,39
1402	A,78.00	1.4127	1.1232	0.0042	37,39	1402	A,90.01	1.5681	1.1289	0.0059	37
1402	A,90.01	1.5682	1.1206	0.0058	37	1402	A,90.01	1.5683	1.1259	0.0059	37
1402	A,93.01	1.6009	1.1263	0.0063	37	1402	A,93.01	1.6009	1.1195	0.0063	37
1402	A,93.01	1.6009	1.1266	0.0063	37	1402	A,96.01	1.6314	1.1280	0.0067	37
1402	A,96.01	1.6314	1.1294	0.0067	37	1402	A,96.01	1.6314	1.1284	0.0068	37
1402	A,96.01	1.6314	1.1507	0.0068	37	1402	A,99.00	1.6601	1.1230	0.0072	37
1402	A,99.00	1.6601	1.1398	0.0101	37	1402	A,99.00	1.6602	1.1337	0.0072	37
1402	A,102.00	1.6878	1.1452	0.0077	37	1402	A,102.00	1.6878	1.1493	0.0077	37
1402	A,102.00	1.6880	1.1570	0.0077	37	1402	A,105.00	1.7130	1.1389	0.0081	37
1402	A,105.00	1.7130	1.1451	0.0082	37	1402	A,105.00	1.7131	1.1510	0.0082	37
1402	A,105.00	1.7132	1.1473	0.0082	37	1402	A,105.00	1.7132	1.1513	0.0082	37
1402	A,108.00	1.7367	1.1379	0.0134	37	1402	A,108.00	1.7368	1.1549	0.0086	37
1402	A,108.00	1.7368	1.1434	0.0086	37	1402	A,108.00	1.7368	1.1480	0.0086	37
1402	A,108.00	1.7368	1.1446	0.0086	37	1402	A,108.00	1.7369	1.1499	0.0086	37
1402	A,111.00	1.7587	1.1563	0.0091	37	1402	A,111.00	1.7587	1.1640	0.0092	37
1402	A,111.00	1.7588	1.1477	0.0091	37	1402	A,111.00	1.7588	1.1658	0.0092	37
1402	A,111.00	1.7588	1.1691	0.0092	37	1402	A,111.00	1.7589	1.1489	0.0091	37
1402	A,114.00	1.7792	1.1625	0.0096	37	1402	A,114.00	1.7792	1.1629	0.0096	37
1402	A,114.00	1.7793	1.1566	0.0125	37	1402	A,114.00	1.7793	1.1592	0.0096	37
1402	A,114.00	1.7794	1.1460	0.0095	37	1402	A,114.00	1.7794	1.1655	0.0096	37
1508	A,78.00	1.5735	1.1347	0.0075	38,39	1508	A,81.00	1.6151	1.1298	0.0075	38,39
1508	A,81.00	1.6151	1.1124	0.0074	38,39	1508	A,81.00	1.6153	1.1267	0.0074	38,39
1508	A,81.00	1.6153	1.1255	0.0075	38,39	1508	A,93.01	1.7706	1.1542	0.0082	38
1508	A,93.01	1.7708	1.1445	0.0082	38	1508	A,93.01	1.7708	1.1488	0.0082	38
1508	A,93.01	1.7709	1.1470	0.0082	38	1508	A,93.01	1.7710	1.1523	0.0082	38
1508	A,96.01	1.8031	1.1523	0.0088	38	1508	A,96.01	1.8031	1.1490	0.0089	38
1508	A,96.01	1.8032	1.1349	0.0088	38	1508	A,96.01	1.8032	1.1442	0.0089	38
1508	A,99.00	1.8332	1.1317	0.0094	38	1508	A,99.00	1.8332	1.1341	0.0094	38
1508	A,99.00	1.8333	1.1333	0.0095	38	1508	A,99.00	1.8333	1.1373	0.0095	38
1508	A,99.00	1.8333	1.1499	0.0095	38	1508	A,99.00	1.8333	1.1420	0.0094	38
1508	A,102.00	1.8616	1.1511	0.0101	38	1508	A,102.00	1.8616	1.1498	0.0101	38
1508	A,102.00	1.8617	1.1660	0.0102	38	1508	A,102.00	1.8618	1.1426	0.0100	38
1508	A,102.00	1.8618	1.1207	0.0100	38	1508	A,102.00	1.8619	1.1397	0.0100	38
1508	A,102.00	1.8620	1.1479	0.0101	38	1508	A,105.00	1.8881	1.1552	0.0106	38
1508	A,105.00	1.8881	1.1629	0.0107	38	1508	A,105.00	1.8884	1.1565	0.0107	38
1508	A,105.00	1.8884	1.1461	0.0098	38	1508	A,105.00	1.8884	1.1486	0.0107	38
1508	A,105.00	1.8884	1.1467	0.0106	38	1508	A,105.00	1.8885	1.1536	0.0107	38
1508	A,105.00	1.8885	1.1503	0.0107	38	1508	A,108.00	1.9130	1.1560	0.0112	38
1508	A,108.00	1.9130	1.1487	0.0112	38	1508	A,108.00	1.9131	1.1613	0.0112	38
1508	A,108.00	1.9132	1.1497	0.0112	38	1508	A,108.00	1.9132	1.1542	0.0112	38
1508	A,108.00	1.9132	1.1654	0.0112	38	1508	A,108.00	1.9133	1.1534	0.0112	38
1508	A,108.00	1.9133	1.1554	0.0112	38	1508	A,108.00	1.9133	1.1514	0.0112	38
1508	A,108.00	1.9135	1.1409	0.0111	38	1508	A,111.00	1.9361	1.1265	0.0117	38
1508	A,111.00	1.9361	1.1326	0.0123	38	1508	A,111.00	1.9361	1.1403	0.0118	38
1508	A,111.00	1.9362	1.1498	0.0118	38	1508	A,111.00	1.9364	1.1400	0.0123	38

Table C.3.: Numerical values for the form factors with 1-σ statistical errors. The Q^2 values are spaced evenly on a logarithmic scale. The results listed here are without the Feshbach Coulomb correction and without any TPE correction applied.

Q^2 (GeV/c)^2	G_E	G_M/μ_p	$\mu_p\, G_E/G_M$
0.0040	0.98712 ± 0.00016	0.98987 ± 0.00009	0.99722 ± 0.00019
0.0043	0.98617 ± 0.00017	0.98912 ± 0.00010	0.99702 ± 0.00020
0.0046	0.98515 ± 0.00019	0.98831 ± 0.00011	0.99681 ± 0.00022
0.0050	0.98406 ± 0.00020	0.98743 ± 0.00012	0.99659 ± 0.00023
0.0053	0.98289 ± 0.00021	0.98650 ± 0.00012	0.99635 ± 0.00025
0.0057	0.98164 ± 0.00023	0.98549 ± 0.00013	0.99609 ± 0.00027
0.0062	0.98029 ± 0.00024	0.98441 ± 0.00014	0.99582 ± 0.00029
0.0066	0.97885 ± 0.00026	0.98325 ± 0.00015	0.99552 ± 0.00031
0.0071	0.97731 ± 0.00028	0.98200 ± 0.00016	0.99522 ± 0.00033
0.0076	0.97565 ± 0.00030	0.98066 ± 0.00017	0.99489 ± 0.00035
0.0082	0.97388 ± 0.00032	0.97923 ± 0.00018	0.99454 ± 0.00037
0.0088	0.97198 ± 0.00034	0.97768 ± 0.00019	0.99417 ± 0.00040
0.0095	0.96995 ± 0.00036	0.97602 ± 0.00020	0.99377 ± 0.00042
0.0102	0.96777 ± 0.00038	0.97424 ± 0.00022	0.99336 ± 0.00045
0.0110	0.96545 ± 0.00041	0.97233 ± 0.00023	0.99292 ± 0.00048
0.0118	0.96296 ± 0.00043	0.97028 ± 0.00024	0.99246 ± 0.00051
0.0127	0.96030 ± 0.00046	0.96807 ± 0.00026	0.99197 ± 0.00055
0.0136	0.95745 ± 0.00049	0.96571 ± 0.00027	0.99145 ± 0.00058
0.0146	0.95442 ± 0.00052	0.96317 ± 0.00029	0.99091 ± 0.00062
0.0157	0.95117 ± 0.00055	0.96044 ± 0.00030	0.99035 ± 0.00065
0.0169	0.94771 ± 0.00058	0.95752 ± 0.00032	0.98976 ± 0.00069
0.0182	0.94401 ± 0.00062	0.95438 ± 0.00033	0.98914 ± 0.00073
0.0195	0.94007 ± 0.00065	0.95102 ± 0.00035	0.98849 ± 0.00078
0.0210	0.93588 ± 0.00069	0.94741 ± 0.00037	0.98783 ± 0.00082
0.0225	0.93140 ± 0.00072	0.94354 ± 0.00038	0.98713 ± 0.00087
0.0242	0.92664 ± 0.00076	0.93940 ± 0.00040	0.98642 ± 0.00091
0.0260	0.92158 ± 0.00080	0.93496 ± 0.00041	0.98569 ± 0.00096
0.0280	0.91619 ± 0.00084	0.93020 ± 0.00043	0.98494 ± 0.00101
0.0301	0.91047 ± 0.00088	0.92510 ± 0.00044	0.98418 ± 0.00106
0.0323	0.90440 ± 0.00091	0.91965 ± 0.00046	0.98341 ± 0.00111
0.0347	0.89796 ± 0.00095	0.91382 ± 0.00047	0.98264 ± 0.00116
0.0373	0.89113 ± 0.00099	0.90759 ± 0.00048	0.98187 ± 0.00121
0.0401	0.88391 ± 0.00102	0.90092 ± 0.00048	0.98111 ± 0.00125
0.0431	0.87626 ± 0.00106	0.89381 ± 0.00049	0.98037 ± 0.00130
0.0463	0.86818 ± 0.00109	0.88622 ± 0.00049	0.97965 ± 0.00134
0.0498	0.85966 ± 0.00112	0.87813 ± 0.00049	0.97897 ± 0.00138
0.0535	0.85067 ± 0.00114	0.86950 ± 0.00049	0.97833 ± 0.00142
0.0575	0.84119 ± 0.00116	0.86033 ± 0.00048	0.97776 ± 0.00146
0.0618	0.83123 ± 0.00118	0.85058 ± 0.00047	0.97725 ± 0.00148
0.0664	0.82076 ± 0.00119	0.84023 ± 0.00045	0.97683 ± 0.00151
0.0713	0.80977 ± 0.00119	0.82926 ± 0.00044	0.97650 ± 0.00152
0.0767	0.79826 ± 0.00119	0.81765 ± 0.00042	0.97629 ± 0.00153
0.0824	0.78620 ± 0.00117	0.80538 ± 0.00040	0.97619 ± 0.00154
0.0885	0.77360 ± 0.00116	0.79244 ± 0.00038	0.97622 ± 0.00153
0.0952	0.76044 ± 0.00113	0.77883 ± 0.00037	0.97639 ± 0.00152
0.1023	0.74672 ± 0.00109	0.76453 ± 0.00037	0.97670 ± 0.00151
0.1099	0.73244 ± 0.00105	0.74957 ± 0.00038	0.97715 ± 0.00149
0.1181	0.71759 ± 0.00100	0.73394 ± 0.00041	0.97772 ± 0.00147
0.1269	0.70216 ± 0.00094	0.71768 ± 0.00045	0.97839 ± 0.00145
0.1364	0.68617 ± 0.00088	0.70080 ± 0.00050	0.97912 ± 0.00144
0.1466	0.66960 ± 0.00082	0.68336 ± 0.00057	0.97987 ± 0.00145
0.1576	0.65246 ± 0.00075	0.66539 ± 0.00063	0.98056 ± 0.00146
0.1693	0.63475 ± 0.00069	0.64698 ± 0.00069	0.98110 ± 0.00150
0.1820	0.61648 ± 0.00063	0.62817 ± 0.00075	0.98138 ± 0.00155
0.1956	0.59765 ± 0.00058	0.60906 ± 0.00080	0.98127 ± 0.00160
0.2102	0.57828 ± 0.00054	0.58972 ± 0.00083	0.98061 ± 0.00166
0.2259	0.55840 ± 0.00052	0.57023 ± 0.00084	0.97925 ± 0.00171
0.2427	0.53802 ± 0.00051	0.55066 ± 0.00084	0.97706 ± 0.00174
0.2609	0.51721 ± 0.00051	0.53106 ± 0.00081	0.97393 ± 0.00177
0.2803	0.49604 ± 0.00053	0.51145 ± 0.00076	0.96986 ± 0.00178
0.3013	0.47459 ± 0.00055	0.49179 ± 0.00071	0.96503 ± 0.00179
0.3238	0.45301 ± 0.00058	0.47201 ± 0.00065	0.95975 ± 0.00181
0.3480	0.43138 ± 0.00061	0.45213 ± 0.00060	0.95410 ± 0.00185
0.3740	0.40976 ± 0.00064	0.43217 ± 0.00055	0.94813 ± 0.00191
0.4019	0.38823 ± 0.00068	0.41219 ± 0.00050	0.94189 ± 0.00201
0.4319	0.36689 ± 0.00073	0.39221 ± 0.00046	0.93544 ± 0.00216
0.4642	0.34579 ± 0.00079	0.37228 ± 0.00042	0.92884 ± 0.00236
0.4988	0.32502 ± 0.00086	0.35245 ± 0.00039	0.92217 ± 0.00263
0.5361	0.30467 ± 0.00093	0.33279 ± 0.00036	0.91549 ± 0.00298
0.5761	0.28479 ± 0.00101	0.31337 ± 0.00034	0.90881 ± 0.00339
0.6191	0.26548 ± 0.00109	0.29430 ± 0.00033	0.90208 ± 0.00382
0.6654	0.24680 ± 0.00113	0.27570 ± 0.00031	0.89515 ± 0.00424
0.7151	0.22881 ± 0.00114	0.25771 ± 0.00030	0.88785 ± 0.00455
0.7685	0.21156 ± 0.00112	0.24037 ± 0.00028	0.88017 ± 0.00476
0.8259	0.19509 ± 0.00107	0.22369 ± 0.00026	0.87214 ± 0.00488
0.8876	0.17941 ± 0.00100	0.20770 ± 0.00024	0.86380 ± 0.00493

Q^2 (GeV/c)^2	G_E	G_M/μ_p	$\mu_p\, G_E/G_M$
0.9539	0.16453 ± 0.00094	0.19238 ± 0.00023	0.85523 ± 0.00498
1.0251	0.15043 ± 0.00088	0.17770 ± 0.00022	0.84653 ± 0.00504
1.1017	0.13711 ± 0.00081	0.16366 ± 0.00022	0.83780 ± 0.00507
1.1839	0.12459 ± 0.00074	0.15025 ± 0.00021	0.82918 ± 0.00504
1.2724	0.11287 ± 0.00067	0.13752 ± 0.00020	0.82080 ± 0.00504
1.3674	0.10200 ± 0.00064	0.12548 ± 0.00019	0.81286 ± 0.00522
1.4695	0.09199 ± 0.00063	0.11418 ± 0.00017	0.80561 ± 0.00568
1.5793	0.08285 ± 0.00064	0.10364 ± 0.00016	0.79935 ± 0.00631
1.6972	0.07455 ± 0.00064	0.09384 ± 0.00015	0.79442 ± 0.00697
1.8240	0.06705 ± 0.00063	0.08475 ± 0.00014	0.79119 ± 0.00753
1.9602	0.06033 ± 0.00059	0.07635 ± 0.00012	0.79009 ± 0.00790
2.1066	0.05432 ± 0.00054	0.06862 ± 0.00011	0.79155 ± 0.00804
2.2640	0.04897 ± 0.00049	0.06152 ± 0.00010	0.79595 ± 0.00800
2.4330	0.04422 ± 0.00044	0.05503 ± 0.00009	0.80363 ± 0.00802
2.6148	0.04001 ± 0.00041	0.04911 ± 0.00008	0.81471 ± 0.00847
2.8101	0.03624 ± 0.00042	0.04372 ± 0.00007	0.82896 ± 0.00962
3.0199	0.03285 ± 0.00044	0.03884 ± 0.00006	0.84558 ± 0.01132
3.2455	0.02973 ± 0.00045	0.03444 ± 0.00006	0.86322 ± 0.01306
3.4879	0.02684 ± 0.00045	0.03047 ± 0.00005	0.88085 ± 0.01471
3.7484	0.02414 ± 0.00045	0.02690 ± 0.00005	0.89726 ± 0.01667
4.0283	0.02160 ± 0.00047	0.02371 ± 0.00005	0.91085 ± 0.01980
4.3292	0.01918 ± 0.00052	0.02086 ± 0.00004	0.91951 ± 0.02496
4.6525	0.01686 ± 0.00059	0.01832 ± 0.00004	0.92066 ± 0.03239
5.0000	0.01463 ± 0.00067	0.01606 ± 0.00005	0.91114 ± 0.04151

References

[1] Rutherford, E. (1911). The scattering of alpha and beta particles by matter and the structure of the atom. *Phil. Mag. Ser. 6*, *21*, 669–688. https://doi.org/10.1080/14786440508637080

[2] Gegier, H., Marsden, E., & Rutherford, E. (1909). On a diffuse reflection of the α-particles. *Proceedings of the Royal Society of London. Series A, Containing Papers of a Mathematical and Physical Character*, *82*(557), 495–500. https://doi.org/10.1098/rspa.1909.0054

[3] Rutherford, E. (1919). Collision of α particles with light atoms. IV. An anomalous effect in nitrogen. *Phil. Mag. Ser. 6*, *37*, 581–587. https://doi.org/10.1080/14786431003659230

[4] Chadwick, J. (1932). Possible Existence of a Neutron. *Nature*, *129*, 312. https://doi.org/10.1038/129312a0

[5] Thomson, J. J. (1897). Cathode rays. *Phil. Mag. Ser. 5*, *44*, 293–316. https://doi.org/10.1080/14786449708621070

[6] Kinoshita, T., & Nio, M. (2006). Improved α^4 term of the electron anomalous magnetic moment. *Phys. Rev. D*, *73*, 013003. https://doi.org/10.1103/PhysRevD.73.013003

[7] Odom, B. C., Hanneke, D., D'Urso, B., & Gabrielse, G. (2006). New Measurement of the Electron Magnetic Moment Using a One-Electron Quantum Cyclotron. *Phys. Rev. Lett.*, *97*, 030801. https://doi.org/10.1103/PhysRevLett.97.030801

[8] Gabrielse, G., Hanneke, D., Kinoshita, T., Nio, M., & Odom, B. C. (2006). New Determination of the Fine Structure Constant from the Electron g Value and QED. *Phys. Rev. Lett.*, *97*, 030802. https://doi.org/10.1103/PhysRevLett.97.030802

[9] Frisch, R., & Stern, O. (1933). Über die magnetische Ablenkung von Wasserstoffmolekülen und das magnetische Moment des Protons. I. *Zeitschrift für Physik*, *85*(1), 4–16. https://doi.org/10.1007/BF01330773

[10] Estermann, O., I.and Stern. (1933). Über die magnetische Ablenkung von Wasserstoffmolekülen und das magnetische Moment des Protons. II. *Zeitschrift für Physik*, *85*(1), 17–24. https://doi.org/10.1007/BF01330774

[11] Tiesinga, E., Mohr, P. J., Newell, D. B., & Taylor, B. N. (2021). CODATA recommended values of the fundamental physical constants: 2018*. *Rev. Mod. Phys.*, *93*(2), 025010. https://doi.org/10.1103/RevModPhys.93.025010

[12] Hofstadter, R., & McAllister, R. W. (1955). Electron Scattering From the Proton. *Phys. Rev.*, *98*, 217–218. https://doi.org/10.1103/PhysRev.98.217

[13] Chambers, E. E., & Hofstadter, R. (1956). Structure of the Proton. *Phys. Rev.*, *103*, 1454–1463. https://doi.org/10.1103/PhysRev.103.1454

[14] Hofstadter, R. (1956). Electron scattering and nuclear structure. *Rev. Mod. Phys.*, *28*, 214–254. https://doi.org/10.1103/RevModPhys.28.214

[15] Simon, G. G., Borkowski, F., Schmitt, C., & Walther, V. H. (1980). THE STRUCTURE OF THE NUCLEONS. *Z. Naturforsch. A*, *35*, 1–8.

[16] Karshenboim, S. G. (1999). What do we actually know on the proton radius? *Can. J. Phys.*, *77*, 241–266. https://doi.org/10.1139/cjp-77-4-241

[17] Jones, M. K., & others. (2000). G_{E_p}/G_{M_p} ratio by polarization transfer in $\vec{e}\ p \to e\ \vec{p}$. *Phys. Rev. Lett.*, *84*, 1398–1402. https://doi.org/10.1103/PhysRevLett.84.1398

[18] Bernauer, J. C. (2010). *Measurement of the elastic electron-proton cross section and separation of the electric and magnetic form factor in the Q^2 range from 0.004 to 1 (GeV/c)^2* (PhD thesis). Institut für Kernphysik, Johannes Gutenberg-Universität Mainz. Retrieved from https://download.uni-mainz.de/fb08-kpha1/doctor/bernauer.pdf

[19] Bernauer, J. C., & others. (2010). High-precision determination of the electric and magnetic form factors of the proton. *Phys. Rev. Lett.*, *105*, 242001. https://doi.org/10.1103/PhysRevLett.105.242001

[20] Bernauer, J. C., & others. (2014). Electric and magnetic form factors of the proton. *Phys. Rev. C*, *90*(1), 015206. https://doi.org/10.1103/PhysRevC.90.015206

[21] Mohr, P. J., Taylor, B. N., & Newell, D. B. (2008). CODATA Recommended Values of the Fundamental Physical Constants: 2006. *Rev. Mod. Phys.*, *80*, 633–730. https://doi.org/10.1103/RevModPhys.80.633

[22] Pohl, R., & others. (2010). The size of the proton. *Nature*, *466*, 213–216. https://doi.org/10.1038/nature09250

[23] Xiong, W., & others. (2019). A small proton charge radius from an electron–proton scattering experiment. *Nature*, *575*(7781), 147–150. https://doi.org/10.1038/s41586-019-1721-2

[24] Wang, Y., & others. (2022). Low-Q2 elastic electron-proton scattering using a gas jet target. *Phys. Rev. C*, *106*(4), 044610. https://doi.org/10.1103/PhysRevC.106.044610

[25] Mihovilovič, M., & others. (2021). The proton charge radius extracted from the initial-state radiation experiment at MAMI. *Eur. Phys. J. A*, *57*(3), 107. https://doi.org/10.1140/epja/s10050-021-00414-x

[26] Zhan, X., & others. (2011). High-Precision Measurement of the Proton Elastic Form Factor Ratio $\mu_p G_E/G_M$ at low Q^2. *Phys. Lett. B*, *705*, 59–64. https://doi.org/10.1016/j.physletb.2011.10.002

[27] Bezginov, N., Valdez, T., Horbatsch, M., Marsman, A., Vutha, A. C., & Hessels, E. A. (2019). A measurement of the atomic hydrogen Lamb shift and the proton charge radius. *Science*, *365*(6457), 1007–1012. https://doi.org/10.1126/science.aau7807

[28] Fleurbaey, H., & others. (2018). New Measurement of the $1S - 3S$ Transition Frequency of Hydrogen: Contribution to the Proton Charge Radius Puzzle. *Phys. Rev. Lett.*, *120*(18), 183001. https://doi.org/10.1103/PhysRevLett.120.183001

[29] Beyer, A., & others. (2017). The Rydberg constant and proton size from atomic hydrogen. *Science*, *358*(6359), 79–85. https://doi.org/10.1126/science.aah6677

[30] Antognini, A., & others. (2013). Proton Structure from the Measurement of $2S - 2P$ Transition Frequencies of Muonic Hydrogen. *Science*, *339*, 417–420. https://doi.org/10.1126/science.1230016

[31] Zhou, S., Giulani, P., Piekarewicz, J., Bhattacharya, A., & Pati, D. (2019). Reexamining the proton-radius problem using constrained Gaussian processes. *Phys. Rev. C*, *99*(5), 055202. https://doi.org/10.1103/PhysRevC.99.055202

[32] Alarcón, J. M., Higinbotham, D. W., Weiss, C., & Ye, Z. (2019). Proton charge radius extraction from electron scattering data using dispersively improved chiral effective field theory. *Phys. Rev. C*, *99*(4), 044303. https://doi.org/10.1103/PhysRevC.99.044303

[33] Sick, I. (2018). Proton charge radius from electron scattering. *Atoms*, *6*(1). https://doi.org/10.3390/atoms6010002

[34] Horbatsch, M., Hessels, E. A., & Pineda, A. (2017). Proton radius from electron-proton scattering and chiral perturbation theory. *Phys. Rev. C*, *95*(3), 035203. https://doi.org/10.1103/PhysRevC.95.035203

[35] Higinbotham, D. W., Kabir, A. A., Lin, V., Meekins, D., Norum, B., & Sawatzky, B. (2016). Proton radius from electron scattering data. *Phys. Rev. C*, *93*(5), 055207. https://doi.org/10.1103/PhysRevC.93.055207

[36] Griffioen, K., Carlson, C., & Maddox, S. (2016). Consistency of electron scattering data with a small proton radius. *Phys. Rev. C*, *93*(6), 065207. https://doi.org/10.1103/PhysRevC.93.065207

[37] Arrington, J., & Sick, I. (2015). Evaluation of the proton charge radius from e-p scattering. *J. Phys. Chem. Ref. Data*, *44*, 031204. https://doi.org/10.1063/1.4921430

[38] Graczyk, K. M., & Juszczak, C. (2014). Proton radius from Bayesian inference. *Phys. Rev. C*, *90*, 054334. https://doi.org/10.1103/PhysRevC.90.054334

[39] Lorenz, I. T., Hammer, H.-W., & Meissner, U.-G. (2012). The size of the proton - closing in on the radius puzzle. *Eur. Phys. J. A*, *48*, 151. https://doi.org/10.1140/epja/i2012-12151-1

[40] Ron, G., & others. (2011). Low Q^2 measurements of the proton form factor ratio mu_pG_E/G_M. *Phys. Rev. C*, *84*, 055204. https://doi.org/10.1103/PhysRevC.84.055204

[41] Hill, R. J., & Paz, G. (2010). Model independent extraction of the proton charge radius from electron scattering. *Phys. Rev. D*, *82*, 113005. https://doi.org/10.1103/PhysRevD.82.113005

[42] A1 Collaboration. (2005). *Measurements of the elastic electron-proton cross section and separation of the form factors G_e and G_m in the Q^2 region from 0.1 (GeV/c)^2 to 2 (GeV/c)^2* (Proposal No. MAMI-A1-2/05). Institut für Kernphysik, Johannes Gutenberg-Universität Mainz. Retrieved from https://download.uni-mainz.de/fb08-kpha1/proposals/MAMI-A1-2-05.pdf

[43] Milner, R., & others. (2014). The OLYMPUS Experiment. *Nucl. Instrum. Meth. A*, *741*, 1–17. https://doi.org/10.1016/j.nima.2013.12.035

[44] Guichon, P. A. M., & Vanderhaeghen, M. (2003). How to reconcile the Rosenbluth and the polarization transfer method in the measurement of the proton form-factors. *Phys. Rev. Lett.*, *91*, 142303. https://doi.org/10.1103/PhysRevLett.91.142303

[45] Afanasev, A., Blunden, P. G., Hasell, D., & Raue, B. A. (2017). Two-photon exchange in elastic electron–proton scattering. *Prog. Part. Nucl. Phys.*, *95*, 245–278. https://doi.org/10.1016/j.ppnp.2017.03.004

[46] Rachek, I. A., & others. (2015). Measurement of the two-photon exchange contribution to the elastic $e^{\pm}p$ scattering cross sections at the VEPP-3 storage ring. *Phys. Rev. Lett.*, *114*(6), 062005. https://doi.org/10.1103/PhysRevLett.114.062005

[47] Adikaram, D., & others. (2015). Towards a resolution of the proton form factor problem: new electron and positron scattering data. *Phys. Rev. Lett.*, *114*, 062003. https://doi.org/10.1103/PhysRevLett.114.062003

[48] Henderson, B. S., & others. (2017). Hard Two-Photon Contribution to Elastic Lepton-Proton Scattering Determined by the OLYMPUS Experiment. *Phys. Rev. Lett.*, *118*(9), 092501. https://doi.org/10.1103/PhysRevLett.118.092501

[49] Greiner, W., & Reinhardt, J. (2009). *Quantum electrodynamics*. Springer-Verlag.

[50] Griffiths, D. J. (2004). *Introduction to elementary particles*. John Wiley & Sons, Ltd. https://doi.org/https://doi.org/10.1002/9783527618460

[51] Rosenbluth, M. N. (1950). High Energy Elastic Scattering of Electrons on Protons. *Phys. Rev.*, *79*, 615–619. https://doi.org/10.1103/PhysRev.79.615

[52] Yennie, D. R., Lévy, M. M., & Ravenhall, D. G. (1957). Electromagnetic structure of nucleons. *Rev. Mod. Phys.*, *29*, 144–157. https://doi.org/10.1103/RevModPhys.29.144

[53] Ernst, F. J., Sachs, R. G., & Wali, K. C. (1960). Electromagnetic form factors of the nucleon. *Phys. Rev.*, *119*, 1105–1114. https://doi.org/10.1103/PhysRev.119.1105

[54] Sachs, R. G. (1962). High-energy behavior of nucleon electromagnetic form factors. *Phys. Rev.*, *126*, 2256–2260. https://doi.org/10.1103/PhysRev.126.2256

[55] Vanderhaeghen, M., Friedrich, J. M., Lhuillier, D., Marchand, D., Van Hoorebeke, L., & Van de Wiele, J. (2000). QED radiative corrections to virtual Compton scattering. *Phys. Rev. C*, *62*, 025501. https://doi.org/10.1103/PhysRevC.62.025501

[56] Maximon, L. C., & Tjon, J. A. (2000). Radiative corrections to electron proton scattering. *Phys. Rev. C*, *62*, 054320. https://doi.org/10.1103/PhysRevC.62.054320

[57] Bloch, F., & Nordsieck, A. (1937). Note on the radiation field of the electron. *Phys. Rev.*, *52*, 54–59. https://doi.org/10.1103/PhysRev.52.54

[58] Jauch, J. M., & Rohrlich, F. (1954). The infrared divergence. *Helvetica Physica Acta*, *27*(7), 613–636.

[59] McKinley, W. A., & Feshbach, H. (1948). The Coulomb Scattering of Relativistic Electrons by Nuclei. *Phys. Rev.*, *74*, 1759–1763. https://doi.org/10.1103/PhysRev.74.1759

[60] Tsai, Y.-S. (1961). Radiative Corrections to Electron-Proton Scattering. *Phys. Rev.*, *122*, 1898–1907. https://doi.org/10.1103/PhysRev.122.1898

[61] Friedrich, J. M. (2000). *Messung der virtuellen Comptonstreuung an MAMI zur Bestimmung generalisierter Polarisierbarkeiten des Protons* (PhD thesis). Institut für Kernphysik, Johannes Gutenberg-Universität Mainz. Retrieved from https://download.uni-mainz.de/fb08-kpha1/doctor/friedrich.pdf

[62] Blunden, P. G., Melnitchouk, W., & Tjon, J. A. (2003). Two photon exchange and elastic electron proton scattering. *Phys. Rev. Lett.*, *91*, 142304. https://doi.org/10.1103/PhysRevLett.91.142304

[63] Ahmed, J., Blunden, P. G., & Melnitchouk, W. (2020). Two-photon exchange from intermediate state resonances in elastic electron-proton scattering. *Phys. Rev. C*, *102*(4), 045205. https://doi.org/10.1103/PhysRevC.102.045205

[64] Herminghaus, H., Feder, A., Kaiser, K. H., Manz, W., & v. d. Schmitt, H. (1976). The design of a cascaded 800 MeV normal conducting C.W. race track microtron. *Nuclear Instruments and Methods*, *138*(1), 1–12. https://doi.org/10.1016/0029-554X(76)90145-2

[65] Kaiser, K.-H., & others. (2008). The 1.5GeV harmonic double-sided microtron at Mainz University. *Nuclear Instruments and Methods in Physics Research Section A: Accelerators, Spectrometers, Detectors and Associated Equipment*, *593*(3), 159–170. https://doi.org/10.1016/j.nima.2008.05.018

[66] Heine, R., & others. (2010). Recent Status of the MAMI-C Accelerator and First Experiences with the Energy Upgrade towards 1.6 GeV. *Conf. Proc. C*, *100523*, 4328–4330.

[67] Dehn, M., Aulenbacher, K., Heine, R., Kreidel, H.-J., Ludwig-Mertin, U., & Jankowiak, A. (2011). The MAMI C accelerator: The beauty of normal conducting multi-turn recirculators. *Eur. Phys. J. ST*, *198*, 19–47. https://doi.org/10.1140/epjst/e2011-01481-4

[68] Dehn, M., Aulenbacher, K., Kreidel, H.-J., Nillius, F., Schlimme, B. S., & Tioukine, V. (2016). Recent Challenges for the 1.5 GeV MAMI-C Accelerator at JGU Mainz. In *7th International Particle Accelerator Conference* (p. THPOY026). https://doi.org/10.18429/JACoW-IPAC2016-THPOY026

[69] Blomqvist, K. I., & others. (1998). The three-spectrometer facility at the Mainz microtron MAMI. *Nucl. Instrum. Meth. A*, *403*, 263–301. https://doi.org/10.1016/S0168-9002(97)01133-9

[70] Distler, M. O. (1990). *Aufbau und Test einer vertikalen Driftkammer* (Diplomarbeit). Institut für Kernphysik, Johannes Gutenberg-Universität Mainz.

[71] Schilling, C.-G. (1994). *Aufbau und Eichung eines Flüssig-Deuterium-Targets für hohe Strahlströme* (Diplomarbeit). Institut für Kernphysik, Johannes Gutenberg-Universität Mainz.

[72] Blobel, V., & Lohrmann, E. (2012). *Statistische und numerische Methoden der Datenanalyse*. Hamburg: V. Blobel. Retrieved from https://www-library.desy.de/elbook.html

[73] Mihovilovič, M. (2015). Advanced event generator for Simul++. Internal Report Institut für Kernphysik, Johannes Gutenberg-Universität Mainz; Unpublished.

[74] Friedrich, J., & Voegler, N. (1982). The salient features of charge density distributions of medium and heavy even-even nuclei determined from a systematic analysis of elastic electron scattering form factors. *Nucl. Phys. A*, *373*, 192–224. https://doi.org/10.1016/0375-9474(82)90147-6

[75] De Forest, T. (1983). Off-Shell electron Nucleon Cross-Sections. The Impulse Approximation. *Nucl. Phys. A*, *392*, 232–248. https://doi.org/10.1016/0375-9474(83)90124-0

[76] Dehn, M. (2020). Private communication.

[77] de Boor, C. (2001). *A practical guide to splines*. Springer-Verlag.

[78] Janssens, T., Hofstadter, R., Hughes, E. B., & Yearian, M. R. (1966). Proton form factors from elastic electron-proton scattering. *Phys. Rev.*, *142*, 922–931. https://doi.org/10.1103/PhysRev.142.922

[79] Goitein, M., & others. (1970). Elastic electron-proton scattering cross-sections measured by a coincidence technique. *Phys. Rev. D*, *1*, 2449–2476. https://doi.org/10.1103/PhysRevD.1.2449

[80] Litt, J., & others. (1970). Measurement of the ratio of the proton form factors, GE/GM, at high momentum transfers and the question of scaling. *Phys. Lett. B*, *31*, 40–44. https://doi.org/10.1016/0370-2693(70)90015-8

[81] Price, L. E., Dunning, J. R., Goitein, M., Hanson, K., Kirk, T., & Wilson, R. (1971). Backward-angle electron-proton elastic scattering and proton electromagnetic form-factors. *Phys. Rev. D*, *4*, 45–53. https://doi.org/10.1103/PhysRevD.4.45

[82] Borkowski, F., Peuser, P., Simon, G. G., Walther, V. H., & Wendling, R. D. (1974). Electromagnetic form-factors of the proton at low four-momentum transfer. *Nucl. Phys. A*, *222*, 269–275. https://doi.org/10.1016/0375-9474(74)90392-3

[83] Borkowski, F., Peuser, P., Simon, G. G., Walther, V. H., & Wendling, R. D. (1975). Electromagnetic Form-Factors of the Proton at Low Four-Momentum Transfer. *Nucl. Phys. B*, *93*, 461–478. https://doi.org/10.1016/0550-3213(75)90514-3

[84] Stein, S., & others. (1975). Electron Scattering at 4-Degrees with Energies of 4.5-GeV - 20-GeV. *Phys. Rev. D*, *12*, 1884. https://doi.org/10.1103/PhysRevD.12.1884

[85] Simon, G. G., Schmitt, C., Borkowski, F., & Walther, V. H. (1980). Absolute electron proton cross-sections at low momentum transfer measured with a high pressure gas target system. *Nucl. Phys. A*, *333*, 381–391. https://doi.org/10.1016/0375-9474(80)90104-9

[86] Bosted, P. E., & others. (1990). Measurements of the Deuteron and Proton Magnetic Form-factors at Large Momentum Transfers. *Phys. Rev. C*, *42*, 38–64. https://doi.org/10.1103/PhysRevC.42.38

[87] Rock, S., & others. (1992). Measurement of elastic electron - neutron scattering and inelastic electron - deuteron scattering cross-sections at high momentum transfer. *Phys. Rev. D*, *46*, 24–44. https://doi.org/10.1103/PhysRevD.46.24

[88] Sill, A. F., & others. (1993). Measurements of elastic electron - proton scattering at large momentum transfer. *Phys. Rev. D*, *48*, 29–55. https://doi.org/10.1103/PhysRevD.48.29

[89] Andivahis, L., & others. (1994). Measurements of the electric and magnetic form factors of the proton from Q^2=1.75 to 8.83 $(\mathrm{GeV/c})^2$. *Phys. Rev. D*, *50*, 5491–5517. https://doi.org/10.1103/PhysRevD.50.5491

[90] Walker, R. C., & others. (1994). Measurements of the proton elastic form factors for $1 \leq Q^2 \leq 3$ $(\mathrm{GeV}/c)^2$ at SLAC. *Phys. Rev. D*, *49*, 5671–5689. https://doi.org/10.1103/PhysRevD.49.5671

[91] Christy, M. E., & others. (2004). Measurements of electron-proton elastic cross sections for $0.4 < Q^2 < 5.5\,\mathrm{GeV/c}^2$. *Phys. Rev. C*, *70*, 015206. https://doi.org/10.1103/PhysRevC.70.015206

[92] Qattan, I. A., & others. (2005). Precision Rosenbluth measurement of the proton elastic form-factors. *Phys. Rev. Lett.*, *94*, 142301. https://doi.org/10.1103/PhysRevLett.94.142301

[93] Akhiezer, A. I., & Rekalo, Mikhail. P. (1973). Polarization effects in the scattering of leptons by hadrons. *Fiz. Elem. Chast. Atom. Yadra*, *4*, 662–688.

[94] Arnold, R. G., Carlson, C. E., & Gross, F. (1981). Polarization transfer in elastic electron scattering from nucleons and deuterons. *Phys. Rev. C*, *23*, 363. https://doi.org/10.1103/PhysRevC.23.363

[95] Milbrath, B. D., & others. (1998). A Comparison of polarization observables in electron scattering from the proton and deuteron. *Phys. Rev. Lett.*, *80*, 452–455. https://doi.org/10.1103/PhysRevLett.80.452

[96] Dieterich, S., & others. (2001). Polarization transfer in the ^{4}He(e$\rightarrow$, e' p$\rightarrow$)^{3}H reaction. *Phys. Lett. B*, *500*, 47–52. https://doi.org/10.1016/S0370-2693(01)00052-1

[97] Gayou, O., & others. (2001). Measurements of the elastic electromagnetic form factor ratio $\mu_p G_{\mathrm{Ep}}/G_{\mathrm{Mp}}$ via polarization transfer. *Phys. Rev. C*, *64*, 038202. https://doi.org/10.1103/PhysRevC.64.038202

[98] Pospischil, Th., & others. (2001). Measurement of G_{Ep}/G_{Mp} via polarization transfer at $Q^2 = 0.4 - GeV/c^2$. *Eur. Phys. J. A*, *12*, 125–127. https://doi.org/10.1007/s100500170046

[99] Gayou, O., & others. (2002). Measurement of G_{E_p}/G_{M_p} in $\vec{e}\ p \rightarrow e\ \vec{p}$ to $Q^2 = 5.6\text{GeV}^2$. *Phys. Rev. Lett.*, *88*, 092301. https://doi.org/10.1103/PhysRevLett.88.092301

[100] Punjabi, V., & others. (2005). Proton elastic form factor ratios to $Q^2 = 3.5\ \text{GeV}^2$ by polarization transfer. *Phys. Rev. C*, *71*, 055202. https://doi.org/10.1103/PhysRevC.71.055202

[101] Jones, M. K., & others. (2006). Proton G_E/G_M from beam-target asymmetry. *Phys. Rev. C*, *74*, 035201. https://doi.org/10.1103/PhysRevC.74.035201

[102] MacLachlan, G., & others. (2006). The ratio of proton electromagnetic form factors via recoil polarimetry at $Q^2 = 1.13\ (\text{GeV/c})^2$. *Nucl. Phys. A*, *764*, 261–273. https://doi.org/10.1016/j.nuclphysa.2005.09.012

[103] Crawford, C. B., & others. (2007). Measurement of the proton's electric to magnetic form factor ratio from $^1\vec{\text{H}}\ (\vec{e}, e'p)$. *Phys. Rev. Lett.*, *98*, 052301. https://doi.org/10.1103/PhysRevLett.98.052301

[104] Meziane, M., & others. (2011). Search for effects beyond the Born approximation in polarization transfer observables in $\vec{e}\vec{p}$ elastic scattering. *Phys. Rev. Lett.*, *106*, 132501. https://doi.org/10.1103/PhysRevLett.106.132501

[105] Bernauer, J. C., & Distler, M. O. (2016). Avoiding common pitfalls and misconceptions in extractions of the proton radius. In *ECT* Workshop on The Proton Radius Puzzle*. Retrieved from https://arxiv.org/abs/1606.02159

[106] Gramolin, A. V., & Russell, R. L. (2022). Transverse charge density and the radius of the proton. *Phys. Rev. D*, *105*(5), 054004. https://doi.org/10.1103/PhysRevD.105.054004

[107] Brodsky, S. J., & Farrar, G. R. (1975). Scaling Laws for Large Momentum Transfer Processes. *Phys. Rev. D*, *11*, 1309. https://doi.org/10.1103/PhysRevD.11.1309

[108] Hug, F., Aulenbacher, K., Heine, R., Ledroit, B., & Simon, D. (2017). MESA - an ERL Project for Particle Physics Experiments. In *28th International Linear Accelerator Conference* (p. MOP106012). https://doi.org/10.18429/JACoW-LINAC2016-MOP106012

[109] Hug, F., & others. (2020). Status of the MESA ERL Project. In *63rd ICFA Advanced Beam Dynamics Workshop on Energy Recovery Linacs* (p. MOCOXBS05). https://doi.org/10.18429/JACoW-ERL2019-MOCOXBS05

[110] Schlimme, B. S., & others. (2021). Operation and characterization of a windowless gas jet target in high-intensity electron beams. *Nucl. Instrum. Meth. A*, *1013*, 165668. https://doi.org/10.1016/j.nima.2021.165668

[111] Korn, M. (1994). *Entwicklung des Bahnrückverfolgungsverfahrens für die Drei-Spektrometer-Anlage und experimentelle Bestimmung der Abbildungseigenschaften der Spektrometer A und B mit elastischer Elektronenstreuung* (PhD thesis). Institut für Kernphysik, Johannes Gutenberg-Universität Mainz. Retrieved from https://download.uni-mainz.de/fb08-kpha1/doctor/korn.pdf